Molecular Engineering Towards High Efficiency Perovskite Solar Cells

THÈSE N° 8625 (2018)

PRÉSENTÉE LE 27 JUILLET 2018
À LA FACULTÉ DES SCIENCES DE BASE
LABORATOIRE DE PHOTONIQUE ET INTERFACES
PROGRAMME DOCTORAL EN CHIMIE ET GÉNIE CHIMIQUE

ÉCOLE POLYTECHNIQUE FÉDÉRALE DE LAUSANNE

POUR L'OBTENTION DU GRADE DE DOCTEUR ÈS SCIENCES

PAR

Jiyoun SEO

acceptée sur proposition du jury:

Prof. J.-E. Moser, président du jury
Prof. M. Graetzel, Dr S. M. Zakeeruddin, directeurs de thèse
Prof. F. Nüesch, rapporteur
Prof. A. DI CARLO, rapporteur
Prof. A. Hagfeldt, rapporteur

EPFL

ÉCOLE POLYTECHNIQUE
FÉDÉRALE DE LAUSANNE

Suisse
2018

Abstract

High energy demands of our society stimulate the development of sustainable technologies, such as those based on solar energy conversion or photovoltaics. Perovskite solar cells (PSCs) are an emerging photovoltaic technology that consist of the perovskite film positioned between the electron transport and hole transport layer, while the photovoltaic properties are determined by each component of the structure, as well as the corresponding interfaces. Since 2009, power conversion efficiency of solar cells has already achieved values above 22%. This rapid progress in perovskite solar cell research led to the increased performance and operational stability, which nevertheless remains a challenge towards the commercialization of PSC technologies.

In the course of this PhD thesis, new strategies in the design of perovskite solar cells were established based on molecular engineering by addressing (1) perovskite, (2) electron transport, as well as (3) hole transport layers, as detailed in the subsequent chapters. The research objectives focused on two key investigation domains, namely charge recombination in the perovskite grain boundaries or interfaces of perovskite / electron transport layers, and the stability of perovskite and hole transport materials. This approach resulted in the development of highly stable and efficient PSCs.

First, with the aim of achieving high performance PSCs, the investigation of crystal growth mechanism was performed to discover the methods to control the grain size distribution within perovskite films that affects their performance by employing organic agents. The study revealed the crystal growth mechanisms and resulted in the achievement of high efficiency of 19.5% in a planar perovskite solar cell architecture. Subsequently, cesium-based perovskites were studied as novel perovskite systems with excellent stability. The role of the cesium in the crystal formation of perovskites was primarily explored, facilitating the rapid room temperature crystallization that led to power conversion efficiency of 18.0% under room temperature. These results are very promising for low temperatue applcation demands, such as the roll-to-roll production and the development of flexible PSCs.

In addition to the perovskite absorption layer, the roles of electron and hole transport layers are very important for the PSC performance. In this regard, while the mesoscopic titanium oxide (mp-TiO$_2$) is predominantly used for electron transport-

Abstract

ing materials, studies of mp-TiO$_2$ are scarce despite its common use in today's most efficient PSCs. Therefore, following the previous investigation of the perovskite material, we further demonstrated for the first time that bimodal porous TiO$_2$ nanoparticles and their surface doping with cesium halides further strengthens the interaction with the perovskite layer, resulting in very high fill factor of 80% and efficiencies exceeding 21%.

Finally, a new dopant, Zn(TFSI)$_2$, for organic hole transport materials was explored to enhance thermal stability by replacement of one of the dopant materials. This approach revealed further improved stability with efficiency exceeding 22%.

This work on the development of highly efficient and stable perovskite solar cells highlights the utility of molecular engineering and provides the basis for facilitating industrial applications in the near future.

Keywords

Perovskite, Perovskite Solar Cells, Photovoltaics, Hybrid Organic Inorganic Perovskite, Crystal Growth, Molecular Engineering

Résumé

Les exigences énergétiques élevées de notre société stimulent le développement de technologies durables, telles que celles basées sur la conversion de l'énergie solaire ou le photovoltaïque. Les cellules solaires pérovskites (PSC) sont une technologie photovoltaïque émergente qui consiste en un film de pérovskite placé entre la couche de transport d'électrons et de transport de trous, tandis que les propriétés photovoltaïques sont déterminées par chacun des composantes de la structure ainsi que leurs interfaces correspondantes. Depuis 2009, l'efficacité de conversion de l'énergie des cellules solaires a déjà atteint des valeurs supérieures à 22%. Ce progrès rapide de la recherche sur les cellules solaires pérovskites a conduit à l'amélioration de la performance et de la stabilité opérationnelle. Ces deux aspects restent néanmoins un défi pour la commercialisation des technologies PSC.

Au cours de cette thèse, de nouvelles stratégies de conception de cellules photovoltaïques à pérovskite ont été établies sur la base de l'ingénierie moléculaire en abordant (1) la pérovskite, (2) le transport d'électrons ainsi que (3) les matériaux de transport des trous, comme détaillé dans les chapitres suivants. Les objectifs de la recherche se concentrent sur deux principaux domaines d'investigation, à savoir la recombinaison des charges dans les joints de grains de pérovskites ou des interfaces de couches de transport de pérovskite / électron, et la stabilité des matériaux de transport de pérovskites et de trous. Cette approche a abouti au développement de PSC hautement stables et efficaces.

Tout d'abord, dans le but d'obtenir des PSC à haute performance, l'étude du mécanisme de croissance des cristaux a permis de découvrir les méthodes de contrôle de la distribution granulométrique des films de pérovskite qui affectent leurs performances en utilisant des agents organiques. L'étude a révélé les mécanismes de croissance cristalline et a abouti à l'obtention d'un rendement élevé de 19.5% dans une architecture de cellules solaires à pérovskite planaire. Par la suite, des pérovskites à base de césium ont été étudiées en tant que nouveaux systèmes de pérovskites avec une excellente stabilité. Le rôle du césium dans la formation de cristaux de pérovskites a été exploré initialement, facilitant la cristallisation rapide à température ambiante qui a conduit à une efficacité de conversion de puissance de 18.0% à température ambiante. Ces résultats sont très prometteurs pour les de-

mandes d'application à basse température, telles que la production de rouleaux à rouleaux et le développement de PSC flexibles.

En plus de la couche d'absorption de la pérovskite, les rôles des couches de transport d'électrons et de trous sont mp-TiO_2 très importants pour la performance des PSC. À cet égard, alors que l'oxyde de titane mésoscopique (mp-TiO_2) est principalement utilisé pour les matériaux de transport d'électrons, les études de mp-TiO_2 sont rares malgré son utilisation courante dans les PSC les plus efficaces d'aujourd'hui. Par conséquent, suite à l'étude précédente du matériau pérovskite, nous avons démontré pour la première fois que les nanoparticules de TiO_2 poreuses bimodales et leur dopage de surface avec des halogénures de césium renforcent l'interaction avec la couche de pérovskite, résultant en un facteur de remplissage très élevé de 80% et une efficacité dépassant 21%.

Enfin, un nouveau dopant, $Zn(TFSI)_2$, pour les matériaux de transport de trous organiques a été exploré pour améliorer la stabilité thermique en remplaçant l'un des matériaux dopants, ce qui montre une stabilité et une efficacité encore supérieures à 22%

Ce travail sur le développement de cellules solaires pérovskites hautement efficaces et stables souligne l'utilité de l'ingénierie moléculaire et fournit la base pour faciliter les applications industrielles dans un avenir proche.

Mots-clés

Pérovskite, Cellules solaires à Pérovskite, Photovoltaïque, Pérovskites hybrides organiques-inorganiques, Croissance du cristal, Génie moléculaire

Abbreviations

2D	Two-dimensional
3D	Three-dimensional
AM	Air mass
BET	Brunauer, Emmett and Teller
CB	Chlorobenzene
cm	Centimeter
CT	Charge transfer
CV	Cyclic voltammetry
Cu(II)tmby	bis-(4,4',6,6'-tetramethyl-2,2'-bipyridine)copper(I)
DMF	N,N-dimethylformamide
DMSO	Dimethylsulfoxide
DSC	Differential scanning calorimetry
DSSC	Dye-sensitized solar cell
ETL	Electron transporting layer
ETM	Electron transporting material
eV	Electronvolt
FA	Formamidinium
FF	Fill factor
FK209	tris(2-(1H-pyrazol-1-yl)-4-$tert$-butylpyridine)cobalt(III) tri[bis(tri fluoromethane) sulfonimide]
FTO	Fluorine-doped tin oxide, SnO_2:F
G	Gram
HOMO	Highest occupied molecular orbital
HTL	Hole transporting layer
HTM	Hole transporting material
Hz	Hertz
IPCE	Incident photon-to-current conversion efficiency
IS	Impedance spectroscopy
ITO	Tin-doped indium oxide
J-V	Photocurrent-voltage
J_{max}	Maximum photocurrent
J_{SC}	Short-circuit photocurrent density
K	Kelvin
LED	Light emitting diode
LiTFSI	Lithium bis(trifluoromethanesulfonyl)imide
M	Molar
mp-TiO_2	Mesoporous titanium dioxide

MA	Methylammonium
mA	Milliampere
mol%	Molar percentage
mW	Milliwatt
nm	Nanometer
PCE	Power conversion efficiency
P_{in}	Power of the incident light
P_{max}	Maximum power
PL	Photoluminescence
PSC	Perovskite solar cell
PTAA	Poly[bis(4-phenyl)(2,4,6-trimethylphenyl)amine]
PV	Photovoltaic
PW	Petawatt
rpm	Revolutions per minute
RT	Room temperature
S	Second
S	Siemens
SC	Short-circuit
SEM	Scanning electron microscope
Spiro-OMeTAD	2,2',7,7'-Tetrakis-(N,N'-di-p-methoxyphenylamine)-9,9'-spirobifluorene
ssDSSC	Solid-state dye-sensitized solar cell
T_g	Glass transition temperature
tBP	4-t-butylpyridine
TCO	Transparent conducting oxide
TCSPC	Time-correlated single photon counting
TGA	Thermogravimetric analysis
TRPL	Time-resolved photoluminescence
TW	Terawatt
UV	Ultraviolet
V	Volt
V_{max}	Maximum voltage
V_{OC}	Open-circuit voltage
VB	Valence band
Vis	Visible
Zn(TFSI)$_2$	zinc(II) bis(trifluoromethanesulfonyl)imide

Contents

Chapter 1. Introduction

Perovskite solar cell (PSC) was first introduced by Miyasaka et al. in 2009 based on $CH_3NH_3PbX_3$ (X = Br and I) perovskite materials, which showed light harvesting properties.[1] Since then, PSCs are a rapidly expanding area of photovoltaic technology, showing amazingly fast progress in power conversion efficiencies currently exceeding 22% after a short period of time (Figure 1.1).[2] Because of its fascinating electrical properties for photovoltaic applications and low cost of raw materials, many scientific studies have been reported over the past decade with over 9000 publications. Laboratory Photonics and Interfaces (LPI) directed by Prof. Graetzel has been actively involved in research on PSCs, positioning as a world leader in this research field (Figure 1.2).[3] Considering these efforts on PSCs studies that resulted in significant breakthroughs over the past years, in this Chapter, I will provide an introduction on the special properties of perovskite solar cells and strategies towards high efficiency PSCs.
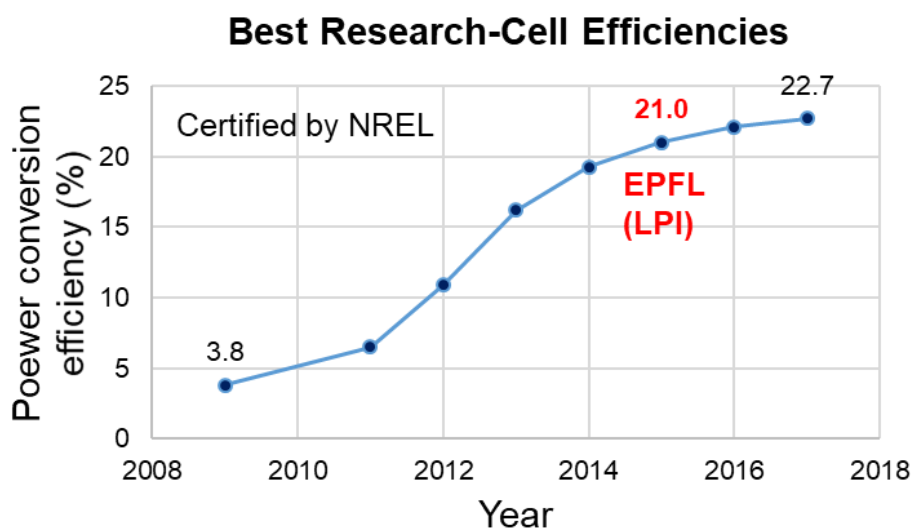
Figure 1.1 Rapid power conversion efficiency of perovskite sloar cells from 2008 to 2018.

(a)

Publications on perovskite solar cells

Source: Scopus
Keyword: Perovskite solar cells
in title, abstract and keywords

(b)
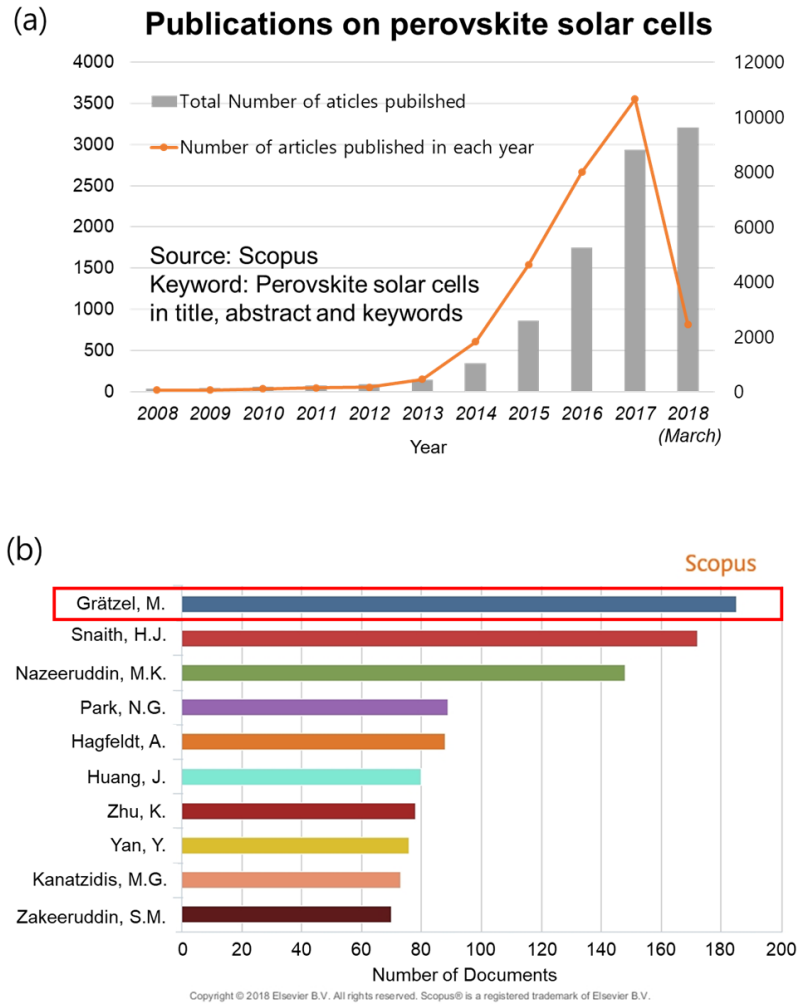
Figure 1.2 (a) Publications on PSCs by year and (b) comparison of the document counts for top ten authors. Data collected based on Scopus using keywords "perovskite solar cells"

1.1 Perovskite for Solar Cells

The component of perovskite solar cells that mainly determines the solar cell perfomance is the perovskite material, most notably organic halide perovskite. The basis of perovskite crystal is a cubic AMX_3 structure, where A generally denotes an organic cation, M is a divalent metal, and X is a halide (A = aliphatic or aromatic ammonium, M = Pb^{2+}, Sn^{2+}, X = Cl^-, Br^-, I^-; Figrure 1.3). Lead(II)-based perovskites have been developed as the most effective light harvesting active layers. In an ideal perovskite structure featuring cubic-symmetry, the M cation is in 6-fold coordination, surrounded by an octahedron of anions (MX_6^-), while A cation is 12-fold coordinated. The MX_6 octahedra constitute a three-dimensional network in which they

share corners with each other. Within this framework, the A cations fill in the space between the octahedra, balancing the charge of the entire network. The choice of an A cation is limited by the space that it occupies. In this regard, the crystallographic structure of a perovskite can be estimated by considering the relative ion size of the constituent atoms that can be expressed through the tolerance factor *t*, which is defined by equation (1.1):

$$t = \frac{r_A + r_I}{\sqrt{2}(r_{Pb} + r_I)} \tag{1.1}$$

where *r* is the corresponding ionic radius in an $APbI_3$ perovskite, and an octahedral factor μ is used to measure the mismatch between the average equilibrium A–X and M–X bond lengths and determine the level of distortion in the system.[4]
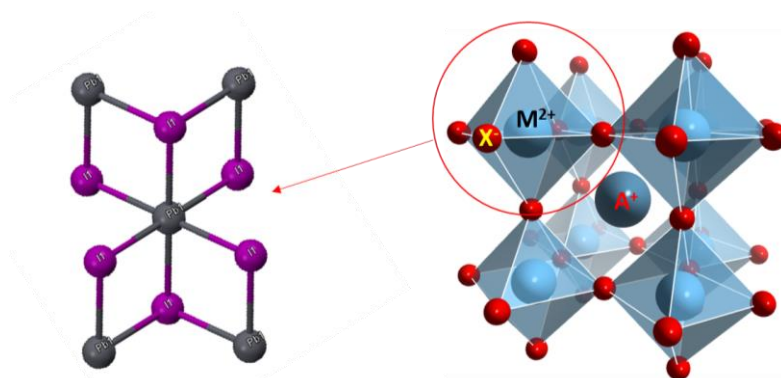
Figure 1.3 The octahedral PbI_2 crystal structure (left) and AMX_3 perovskite crystal structure (right). The representation of the structure is adapted from http://chemicalstructure.net.

In Figure 1.3 crystal structure of $(RNH_3)_2MA_{n-1}M_nX_{3n+1}$, where RNH_3^+ is an alkylammonium or phenethylammonium species, is demonstrated.[5] The <100> oriented inorganic perovskite sheet alternates with a bilayer of organic cations and *n* refers to the number of perovskite sheets. The structure is stabilized by intermolecular interactions; the NH_3^+ termini of the organic cations form hydrogen bonds and engage in electrostatic interactions with the halogens in the perovskite sheets, while the hydrocarbon tails R of the organic cation extend into the space between the perovskite sheets, forming van der Waals interactions. For *n* = 1, a single inorganic layer is formed. As *n* increases, thickness of the inorganic sheet follows the same trend until for *n*→∞ a 3D structure is formed (Figure 1.3).

Based on these structural features, several guidelines can be identified for selecting suitable organic cations for incorporation within the layered perovskite framework. First, the organic molecule must contain one or more terminal cation groups that can

ionically interact with the extended inorganic anion. Furthermore, the cation should ensure effective space occupancy determined by the tolerance factor (t), as well as stabilisation through hydrogen bonding, without the rest of the organic molecule sterically interfering.[6] Accordingly, methylammonium $CH_3NH_3^+$ (MA^+) and formanidinium $CH_3(NH_2)_2^+$ (FA^+) are commonly employed as A cation materials, and they exhibit excellent optoelectronic properties for photovoltaics applications. This particularly refers to their narrow bandgap and a broad absorption range covering almost the whole visible region with a bandgap of 1.5–1.6 eV (corresponding to an absorption onset of about 800 nm).[7] These guidelines are also very useful when selecting the additive molecules for controlling crystal growth of perovskite mateirals, which will be mainly discussed in Chapter 2.
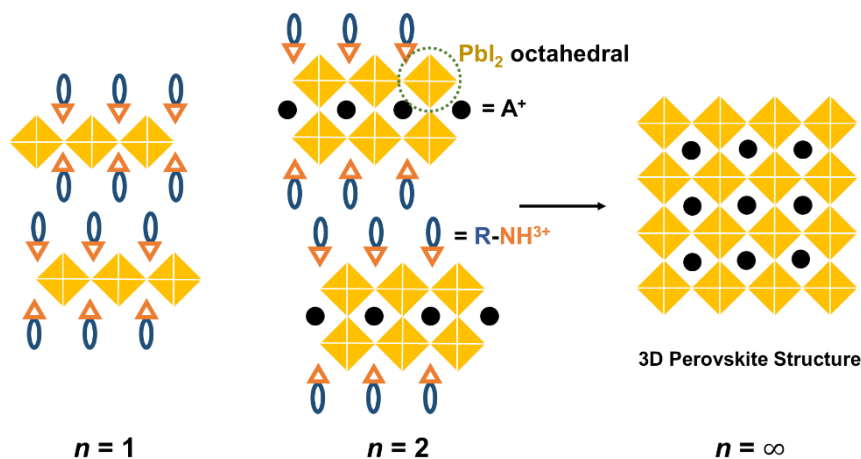
Figure 1.4 Scheme of single-layer <100>-oriented perovskites with RNH_3^+ and 3D perovskite structure of $(RNH_3)_2MA_{n-1}M_nX_{3n+1}$.

1.2 Device Architecture and Working Principles

The perovskite solar cell architecture could involve either n-i-p (typical) and p-i-n (inverted) type structure,[8,9] where the perovskite is an intrinsic semiconductor and light enters through either the n-type or the p-type layer, respectively.[10–12] The typical device architecture is composed of five layers (Figure 1.5), namely (1) transparent electrode (commonly fluorine-doped tin oxide, SnO_2:F, FTO), (2) n-type semiconductor as electron transporting layer (ETL), (3) photoactive perovskite, (4) p-type semiconductor as hole transporting layer (HTL) and (5) the metallic electrode. Depending on the n-type layer, PSCs can futher be categorized into planar (Figure 1.5a) or mesoscopic (Figure 1.5b).[11]. For the work presented in Chapters 2–3, SnO_2 was adapted for electron selective layer introduced by atomic layer deposition (ALD) method and mesocopic TiO_2 was used for high efficiency of PSCs in Chapters 4–5.
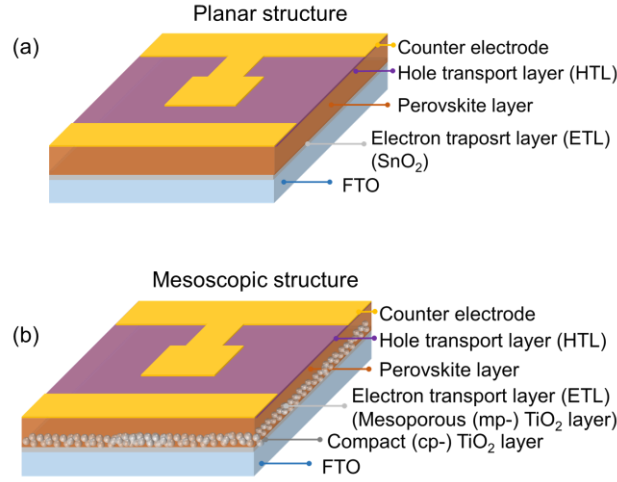
Figure 1.5 Scheme diagrams for n-i-p perovskite solar cell architectures: (a) planar structure and (b) mesoscopic structure. HTL = hole transporting layer; ETL = electron transporting layer; FTO = fluorine-doped tin oxide, SnO_2:F.

Both planar and mesoscopic PSC structures opearte through the same charge-transfer mechanism. Once the sun light illuminates the FTO side of the PSC, the incident photons excite the perovskite materials, generating electrons and holes (Figure 1.6a). The electrons separated from the holes are injected into the conduction band (CB) of the electron transporting layer, before migrating to the anode. Meanwhile, the holes generated upon excitation of the perovskite are transferred to the HOMO level of the hole transporting layer, before injection into the cathode. Electron and hole injections occur quite efficiently in perovskite solar cells owing to the high diffusion lengths of charge carriers. To reduce carrier recombination at the interfaces, which is detrimental to the open-circuit voltage (V_{OC}), the ETL and HTL should be compact and not heavily doped. Upon illumination, electron (E'_{Fn}) and hole (E'_{Fp}) quasi-Fermi levels in the perovskite layer are formed close to valance band minimum (VBM) and conduction band minimum (CBM), respectively, and the difference between E'_{Fn} and E'_{Fp} determines the V_{OC} of the PSCs. The energy level diagram of a representative materials for HTL, perovskite, and ETL employed in this work are presented in Figure 1.6. in the course of device operation, however, undesirable charge transfer processes accompany the photovoltaics, such as charge recombination, which can occur at each interface between the different layers of the cell, as well as at grain boundaries.[13–15] The strategy to reduce recombination and loss of photogenerated charges are discussed in Chapter 2 (grain boundary recombination) and Chapter 4 (interfacial recombination) of this thesis.
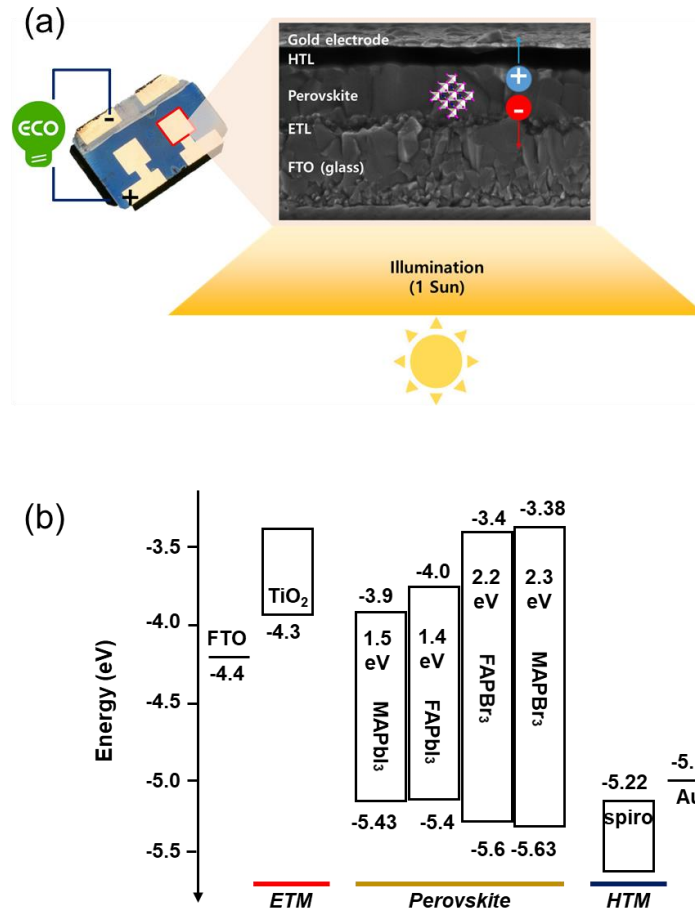
Figure 1.6 Schemaic of energy level diagram of representative lead halides perovskite, TiO₂, spiro-OMeTAD and electodes.[7]

1.3   Components of Typical PSCs

1.3.1   Working Electrode

The cells generally consist of a transparent conducting oxide (TCO) as conducting substrate, such as fluorine-doped tin oxide SnO_2:F (FTO) or tin-doped indium oxide (ITO), which is coated on glass or plastic substrate to provide electrical conductivity. FTO has been recognized as a very promising material because of it being relatively stable under atmospheric conditions, as well as chemically inert, mechanically hard, and high-temperature resistant. Moreover, it has a high tolerance to physical abrasion, high transparency, low reflection and absorption, as well as low sheet resistance, while it is less expensive than ITO. In this work, FTO glass (10 Ω/square Nippon Sheet Glass) was used for PSCs as a working electrode.

1.3.2 Electron Transporting Material

The purpose of the electron transporting materials (ETM) is to prevent the photoinjected electrons in the conductive substrate from direct recombination with the holes. It must feature high transmittance in the UV-Vis region in order for the photon to pass through easily and be absorbed by the perovskite absorber. The ETM layer, which acts as a hole blocking layer, is directly deposited onto the conductive glass substrate to form a compact, continuous n-type contact in order to provide electron selectivity. The mesoporous TiO_2 has mostly been used as ETM in perovskite solar cells. The role of the mesoscopic layer was particularly important for highly efficient perovskite solar cells. Today's record PSCs still adapt a mesoscopic scaffold, hence the role of the porous network in the electron transport cannot be overlooked.[1,16,17] In case of dye sensitized solar cells (DSSC), it is known that the mp-TiO_2 framework provides a high contact area for electron injection, which is used to increase the projected electrode area and boost the dye loading, as well as the external quantum efficiency of both DSSCs and solid -state (ss) DSSCs.[18–20] A study of the effect of porosity of mp-TiO_2 and surface doping to enhance efficiency is described in Chapter 4.

1.3.3 Perovskite Absorber

Organolead halide perovskite layer is the key component in all possible device configurations and it is crucial for light absorption and photogeneration of free carriers. It has received considerable attention for solar cell applications, mainly due to its fascinating optoelectronic properties, inexpensive precursors, and simple fabrication methods based on solution processing. In particular, $CH_3NH_3PbI_3$ (MAPbI_3) has a wide bandgap of 1.54 eV, showing an excellent driving force for both the electron injection into the TiO_2 and the hole injection into the HTM. For $MAPbX_3$ systems (X = Cl ,Br, and I), experiments have shown that larger anions (Cl < Br < I) increase the covalent character of the lead-halogen bonding, and as a result decrease the electron-negativity of halides.[21] Consequently, the band gap gradually decreases from Cl to I, resulting in a red shift of the optical absorption edge. Moreover, the incorporation of two diffident halides[22,23] allows for a continuous tuning of the bandgap and the optical absorption to cover almost the entire visible spectrum. In addition to the structural composition of the perovskite mateirla, the crystal quality of the perovskite directly affects the device performance, despite high diffusion lengths of the charge carriers. Accordingly, increasing the grain sizes and crystallinity provides low defect concentration and less trapping sites acting as recombination centers. For this purpose, various perovskite film deposition methology are employed, such as sequential solution deposition, spin coating, vapor-assisted deposi-

tion, thermal evaporation, and vacuum flash-assisted methods.[17,24–26]

1.3.4 Hole Transporting Material

In general, HTMs play an important role in the device performance and need to fulfil several requirements to provide high efficiency PSCs. Firstly, they have to show high hole mobility, ideally above 10^{-3} cm^2 (V×s)$^{-1}$.[27] In addition, they should have little absorption in the vis-IR region to avoid overlap with the perovskite layer. This is especially important for tandem and semi-transparent architectures. Finally, HTMs should feature a glass transition temperature (T_g) above 85 °C to ensure long-term stability of the PSC that needs to withstand temperatures up to 85 °C. Apart from these key requirements, to be compatible with device fabrication, HTMs need to be easily processed through solution-based techniques, while the HOMO level of the HTM should be higher in energy than the valence band of the perovskite absorber to ensure efficient operation of the device[28]. Based on these criteria, one of the most used HTM is the spiro-OMeTAD (2,2',7,7'-Tetrakis-(*N*,*N*'-di-*p*-methoxyphenylamine)-9,9'-spirobifluorene). Its core consists of two fused fluorenes resulting in a molecule with a twisted shape and a relatively high T_g of 125 °C.[29] This HTM has resulted in some of the highest efficiencies for PSCs, while also being an efficient charge carryint layer in solid state dye sensitized solar cells.[30,31] Despite popular usage, spiro-OMeTAD shows notable drawbacks, such as a rather long and low-yielding synthesis and a low hole mobility of about $1.6×10^{-4}$ cm^2(V×s)$^{-1}$. As a solution to this setback, Snaith et al. reported in 2016 that hole mobility can be increased by a factor of 10 using lithium doping.[32] Presence of such dopants is however frequently associated with the inherent device instabilities. There is now an urgent need to develop new HTMs or dopants to further improve the device stability and increase reproducibility.[33] The investigation of novel p-dopant materials of spiro-OMeTAD enhancing stability is presented in Chapter 5.

1.3.5 Counter Electrode

Counter-electrode as the back contact of the perovskite solar cell is required to complete the internal circuit and to function as an electrode, providing current and voltage for the external electrical work. Traditionally, the back contact of PSC is formed by thermal evaporation of a noble metal with high work function, required to reach high open-circuit voltage of the devices, which is often gold or silver. However, both of these electrode materials have limitations. Au is expensive and migrates through the HTM once exposed to higher temperatures, whereas Ag is unstable due to oxidation. Alternatively, in case of HTM-free PSCs, the carbon composites were demonstrated to be a promising replacement for Au back contact electrodes, allow-

ing simple deposition methods as screen-printing or drop-casting.[34,35] In the course of this work, we focused on Au counter electrodes for perovskite solar cells.

1.4 Device Measurements

1.4.1 *J-V Characterization*

One of the most important charaterization techniues for solar cells is the current-voltage (*J-V*) measurement, which enables to determine the solar cell energy conversion efficiency. The *J-V* measurements are performed under AM 1.5G illuminatrion (1 Sun illumination). As shown in Figure 1.7, the current density is recorded along the scan of linearly-varying voltage in the direction from V_{OC} to 0 V to provide a *J-V* curve, where the V_{OC} is determined as the measured potential at open-circuit condition when the current density equals to 0 mA/cm^2. On the contrary, the J_{SC} is determined by monitoring the current density at short-circuit when the photovoltage equals to 0 V.
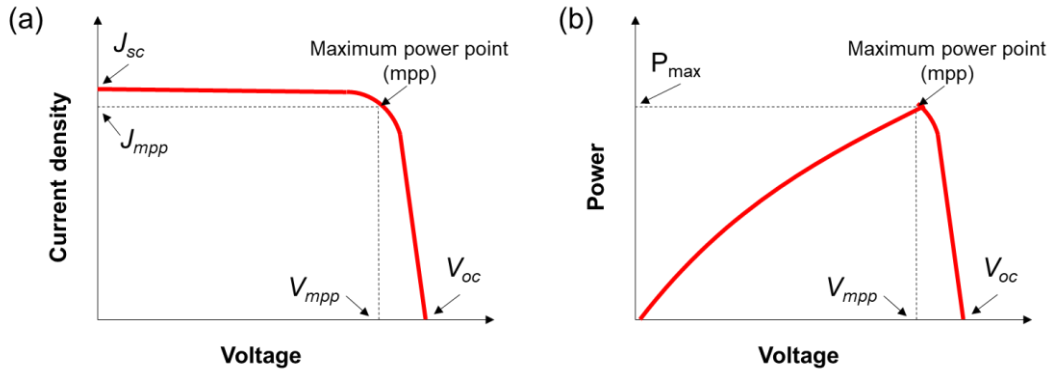
Figure 1.7 Example of a typical solar cell (a) *J-V* characteristics and (b) power output as a function of voltage under illumination.

Therefore, the V_{OC} (V) is the difference in electrical potential between two terminals of a cell, when no current is flowing and the J_{SC} (mA/cm^2) is the photocurrent per unit area when device is short-circuited. The maximum power (P_{max}) point then can be found as the product of the photocurrent and voltage reaching maximum values (J_{max} and V_{max}). The overall power conversion efficiency (η) of a device is therefore defined by the ratio of the maximum power to the power of the incident light (P_{in}) as the following equation (1.2):

$$PCE(\eta) = \frac{P_{max}}{P_{in}} = \frac{J_{sc}V_{oc}FF}{P_{in}} \tag{1.2}$$

For PSCs, the *J-V* curves are often highly dependent on the scan direction, which is called hysteresis behavior.[36,37] Therefore, the scan direction and the scan rate are important for obtaining reliable photovoltaic parameters. That is because higher efficiency may be obtained by holding a perovskite device at a forward bias voltage before measurement compared to that found when the device has been reverse biased or when the device is held at the maximum power point (mpp) or at short-circuit. The fill factor (FF) is a parameter to evaluate the deviation of the measured solar cell efficiency from the theoretical maximum power output of the cell and is defined by equation (1.3) as the ratio of the maximum power (P_{max}) to the external short- and open-circuit values:

$$FF = \frac{J_{max}V_{max}}{J_{sc}V_{oc}} \tag{1.3}$$

1.4.2 Incident Photon to Current Efficiency

Incident photon to current efficiency (IPCE) indicates how efficiently the incoming photons at a specific wavelength are converted into electrons by the PSC device and it is usually used to see the mismatch with the J_{SC} obtained from the *J-V* measurement. The IPCE spectrum (Figure 1.8) is obtained when the device is exposed to illumination and scanning through each monochromatic light wavelength while recording the photocurrent output simultaneously. The IPCE(λ) is calculated the equation (1.4):

$$IPCE(\lambda) = \frac{n_{electrons}(\lambda)}{n_{photons}(\lambda)} = \frac{J_{sc}(\lambda)}{eP_{in}(\lambda)} \tag{1.4}$$

where the $J_{SC}(\lambda)$ is the short-circuit photocurrent density under monochromatic irradiation, $P_{in}(\lambda)$ is the input optical power, and *e* stands for an elementary charge. Integration of the product of IPCE and $J_{SC}(\lambda)$ over the wavelength of the incoming light yields the total short-circuit photocurrent density that is expected to be generated by the solar cell.
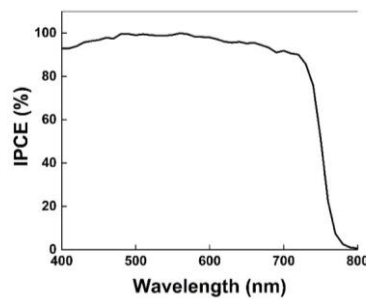
Figure 1.8 Example of IPCE spectrum of perovskite solar cell as a function of wavelength.

1.4.3 Impedance Spectroscopy and IMPS Measurements

Impedance spectroscopy (IS) is a useful tool for characterizing solar cells, which has been developed and well established in classical photovoltaics, such as dye sensitized solar cells (DSSCs)[38–40] and bulk heterojunction (BHJ) cells[41], and recently perovskite solar cells (PSCs). IS is able to characterize solar cells in terms of transport, recombination, and capacitance. Intensity-modulated photocurrent spectroscopy (IMPS) also has been extensively used to investigate carrier transport in DSSCs. In intensity-modulated spectroscopy, it is a light modulation, rather than a voltage perturbation, that is applied to the cell, using a fast LED or a CW laser diode.[42–45] It has been particularly useful in the description of the transport and recombination of photo-generated charges, which can not be directly accessed by impedance spectroscopy without some arbitrary assignment of the spectral features.[46–49]

1.5   Molecular Engineering in Perovskite Solar Cells

There are many studies on perovskite solar cells attempting to employ molecular engeering approach to ehnace the performance in ETL, HTL and perovskite materials. There are several strategies of employing molecular engineering within this research field.

Compositional enginnering is the most well-known method to tune the electronic and physical properties of perovskites by creating new perovskite materials. Recently, there have been many studies using alkali metals (Li, Na, K, Rb, Cs) in new perovskite compositions, for instance. The choice of these cations is absed on the tolerance factor. Empirically, perovskites that have a photoactive black phase fulfill the relation $0.8 < t < 1.0$. [50] The tolerance factor shows that, with respect to the alkali metal cations, only $CsPbI_3$ falls into the range of photoactive perovskites with an α-phase (black phase). Saliba et al. investigated the addition of inorganic cesium to $MA_xFA_{1-x}PbI_{3-y}Br_y$. The resulting triple-cation perovskite compositions are thermally more stable, contain less phase impurities, and are less sensitive to processing conditions.[51] These triple cation perovskites paved the way to a substantial improvement of the quality of the perovskite solar cells in terms of reproducibility, with PCEs over 20% reached on a regular basis.

Another approach to modify the material properties is the purposeful addition of small amounts of new substances, i.e. "molecular additives", into the existing systems. Such additive engineering has been applied to perovskite solar cells to enhance photovoltaic performances and stability. Accordingly, each layer and interface

is suited for additive engineering. Additives related to molecular engineering have been used for some time in crystal engineering. The concept of crystal engineering was first introduced by Pepinsky in 1955, it is defined as the understanding of the role of intermolecular or supramolecular interactions, such as hydrogen bonding, van der Waals force, and ionic bonding in crystalline packing.[52] The perovskite crystal structure consists of octahedral MX_6 and organic molecules with-R-NH_3^+ terminal groups, enabling the establishment of ionic or hydrogen bond interactions.[6] One promising goal for additives in perovskites is the improvement of the crystal quality, as well as the increase of the grain size, in order to prevent performance losses from defects and grain boundaries in the perovskite film. As a first design principle, a perovskite additive is a good candidate if it contains a common cation or anion with the target perovskite precursor, so that its introduction does not disturb the crystal structure significantly. Table 1 summarizes a number of the most recently reported additives, together with the respective perovskite precursor, the PCE of the resulting best device, and the main improvement achieved upon additive introduction with respect to efficiency and stability. They are categorized as metal salts, organic salts, and molecules. Our approach will be discussed in Chapters 2–3.

Table 1. Additives used for perovskite solar cells with PCEs of the corresponding devices.

Additive	Perovskite Precursor	PCE[*] %	V_{OC}[*] V	J_{SC}[*] mA/cm$_2$	Improvement	Ref
$PbCl_2$[#]	$MAPbI_3$	18.1	1.04	23.5	Efficiency	[53]
$Pb(OAc)_2$	$MAPbI_{3-x}Cl_x$	15.2	0.97	21.7	Efficiency	[54]
$Pb(SCN)_2$	$MA_xFA_{1-x}PbI_3$	20.1	1.12	22.9	Efficiency	[55]
$Pb(SCN)_2$	$MAPbI_3$	8.3	0.87	15.1	Stability	[56]
NaI	$MAPbI_{3-x}Cl_x$	12.6	0.92	22.4	Hysteresis	[57]
CsI	$MA_xFA_{1-x}PbI_{3-y}Br_y$	21.2	1.15	23.5	Reproducibility	[51]
RbI	$Cs_zMA_xFA_{1-x}PbI_{3-y}Br_y$	21.8	1.18	22.8	Stability	[50]
Cu (thiourea)I	$MAPbI_{3-x}Cl_x$	19.9	1.13	22.3	Efficiency	[58]
MACl	$MAPbI_3$	12.1	1.02	20.4	Efficiency	[59]
MACl	$MAPbI_3$	18.6	1.08	22.2	Efficiency	[60]
$MA(OAc)_2$	$MAPbI_3$	18.1	1.00	22.9	Efficiency	[61]
NH_4Ac	$MAPbI_3$	17.0	1.10	22.9	Efficiency	[62]
FEAI	$MAPbI_3$	18	1.06	21.2	Stability	[63]
4-ABPACl	$MAPbI_3$	16.6	1.00	22.1	Stability	[64]
1,4-DIB	$MAPbI_{3-x}Cl_x$	13.1	0.94	18.5	Efficiency	[65]

*PCE = Power Conversion Efficiency, V_{OC} = open-circuit voltage, J_{SC} = short-circuit current density were collected from *J–V* curves for champion photovoltaic devices measured under a simulated AM1.5G. Ac = acetate, FEAI = 1,1,1-trifluoro-ethyl ammonium iodide, and OAc = acetoxy. [#]Cl is added in the precursor mixture in order to facilitate film growth. However, due to size mismatch with respect to I, it does not enter into the structure of the generated perovskite structure.

References

[1]   A. Kojima, K. Teshima, Y. Shirai, T. Miyasaka, *J. Am. Chem. Soc.* **2009**, *131*, 6050.

[2]   https://www.nrel.gov/pv/assets/images/efficiency-chart.png

[3]   https://www.scopus.com

[4]   F. Brivio, K. T. Butler, A. Walsh, M. Van Schilfgaarde, *Phys. Rev. B - Condens. Matter Mater. Phys.* **2014**, *89*.

[5]   D. B. Mitzi, *J. Chem. Soc. Dalt. Trans.* **2001**, 1.

[6]   J. Calabrese, N. L. Jones, R. L. Harlow, N. Herron, D. L. Thorn, Y. Wang, *J. Am. Chem. Soc.* **1991**, *113*, 2328.

[7]   C.-C. Chueh, C.-Z. Li, A. K.-Y. Jen, *Energy Environ. Sci.* **2015**, *8*, 1160.

[8]   H. Kim, K.-G. Lim, T.-W. Lee, *Energy Environ. Sci.* **2016**, *9*, 12.

[9]   T. Liu, K. Chen, Q. Hu, R. Zhu, Q. Gong, *Adv. Energy Mater.* **2016**, *6*.

[10]   W. Yin, L. Pan, T. Yang, Y. Liang, *Molecules* **2016**, *21*.

[11]   Z. Song, S. C. Watthage, A. B. Phillips, M. J. Heben, *J. Photonics Energy* **2016**, *6*, 22001.

[12]   C. Momblona, L. Gil-Escrig, E. Bandiello, E. M. Hutter, M. Sessolo, K. Lederer, J. Blochwitz-Nimoth, H. J. Bolink, *Energy Environ. Sci.* **2016**, *9*, 3456.

[13]   T. S. Sherkar, C. Momblona, L. Gil-Escrig, J. Ávila, M. Sessolo, H. J. Bolink, L. J. A. Koster, *ACS Energy Lett.* **2017**, *2*, 1214.

[14]   P. Y. Huang, C. S. Ruiz-Vargas, A. M. Van Der Zande, W. S. Whitney, M. P. Levendorf, J. W. Kevek, S. Garg, J. S. Alden, C. J. Hustedt, Y. Zhu, J. Park, P. L. McEuen, D. A. Muller, *Nature* **2011**, *469*, 389.

[15]   M. Moriya, D. Hirotani, T. Ohta, Y. Ogomi, Q. Shen, T. S. Ripolles, K. Yoshino, T. Toyoda, T. Minemoto, S. Hayase, *ChemSusChem* **2016**, *9*, 2634.

[16]   H.-S. Kim, C.-R. Lee, J.-H. Im, K.-B. Lee, T. Moehl, A. Marchioro, S.-J. Moon, R. Humphry-Baker, J.-H. Yum, J. E. Moser, M. Grätzel, N.-G. Park, *Sci. Rep.* **2012**, *2*, 591.

[17]   J. Burschka, N. Pellet, S.-J. Moon, R. Humphry-Baker, P. Gao, M. K. Nazeeruddin, M. Grätzel, *Nature* **2013**, *499*, 316.

[18] G. Xing, N. Mathews, S. Sun, S. S. Lim, Y. M. Lam, M. Graïzel, S. Mhaisalkar, T. C. Sum, *Sci.* **2013**, *342*, 344.

[19] S. D. Stranks, G. E. Eperon, G. Grancini, C. Menelaou, M. J. P. Alcocer, T. Leijtens, L. M. Herz, A. Petrozza, H. J. Snaith, *Science.* **2013**, *342*, 341.

[20] Y. Zhao, A. M. Nardes, K. Zhu, *J. Phys. Chem. Lett.* **2014**, *5*, 490.

[21] L. Y. Huang, W. R. L. Lambrecht, *Phys. Rev. B - Condens. Matter Mater. Phys.* **2013**, *88*.

[22] J. H. Noh, S. H. Im, J. H. Heo, T. N. Mandal, S. Il Seok, *Nano Lett.* **2013**, *13*, 1764.

[23] S. a. Kulkarni, T. Baikie, P. P. Boix, N. Yantara, N. Mathews, S. Mhaisalkar, *J. Mater. Chem. A* **2014**, *2*, 9221.

[24] M. J. Carnie, C. Charbonneau, M. L. Davies, J. Troughton, T. M. Watson, K. Wojciechowski, H. Snaith, D. a Worsley, *Chem. Commun.* **2013**, *49*, 7893.

[25] X. Li, D. Bi, C. Yi, J.-D. Decoppet, J. Luo, S. M. Zakeeruddin, A. Hagfeldt, M. Gratzel, *Science.* **2016**, *353*, 58.

[26] N. J. Jeon, J. H. Noh, Y. C. Kim, W. S. Yang, S. Ryu, S. Il Seok, *Nat Mater* **2014**, *13*, 897.

[27] Z. H. Bakr, Q. Wali, A. Fakharuddin, L. Schmidt-Mende, T. M. Brown, R. Jose, *Nano Energy* **2017**, *34*, 271.

[28] L. Calio, S. Kazim, M. Gratzel, S. Ahmad, *Angew. Chemie.* **2016**, *55*, 14522.

[29] S. D. S. Cells, T. Leijtens, I. Ding, T. Giovenzana, J. T. Bloking, M. D. Mcgehee, A. Sellinger, **2012**, 1455.

[30] U. Bach, D. Lupo, P. Comte, J. E. Moser, F. Weissörtel, J. Salbeck, H. Spreitzer, M. Grätzel, *Nature* **1998**, *395*, 583.

[31] N. J. Jeon, H. G. Lee, Y. C. Kim, J. Seo, J. H. Noh, J. Lee, S. Il Seok, *J. Am. Chem. Soc.* **2014**, *136*, 7837.

[32] H. J. Snaith, M. Grätzel, *Appl. Phys. Lett.* **2006**, *89*.

[33] J. Zhang, B. Xu, L. Yang, A. Mingorance, C. Ruan, Y. Hua, L. Wang, N. Vlachopoulos, M. Lira-Cantú, G. Boschloo, A. Hagfeldt, L. Sun, E. M. J. Johansson, *Adv. Energy Mater.* **2017**, 1602736.

[34] S. G. Hashmi, D. Martineau, M. I. Dar, T. T. T. Myllymäki, T. Sarikka, V. Ulla, S. M. Zakeeruddin, M. Grätzel, *J. Mater. Chem. A* **2017**, *5*, 12060.

[35] F. Behrouznejad, C. M. Tsai, S. Narra, E. W. G. Diau, N. Taghavinia, *ACS Appl. Mater. Interfaces* **2017**, *9*, 25204.

[36] E. L. Unger, E. T. Hoke, C. D. Bailie, W. H. Nguyen, A. R. Bowring, T. Heumüller, M. G. Christoforo, M. D. McGehee, *Energy Environ. Sci.* **2014**, *7*, 3690.

[37] W. Tress, N. Marinova, T. Moehl, S. M. Zakeeruddin, M. K. Nazeeruddin, M. Grätzel, *Energy Environ. Sci.* **2015**, *8*, 995.

[38] A. Zaban, M. Andreas, B. A. Gregg, *J. Phys. Chem. B* **1997**, *101*, 7990.

[39] R. Kern, R. Sastrawan, J. Ferber, R. Stangl, J. Luther, *Electrochim. Acta* **2002**, *47*, 4213.

[40] S. Soedergren, A. Hagfeldt, J. Olsson, S.-E. Lindquist, *J. Phys. Chem.* **1994**, *98*, 5552.

[41] G. Garcia-Belmonte, A. Guerrero, J. Bisquert, *J. Phys. Chem. Lett.* **2013**, *4*, 877.

[42] L. Dloczik, O. Ileperuma, I. Lauermann, L. M. Peter, E. A. Ponomarev, G. Redmond, N. J. Shaw, I. Uhlendorf, *J. Phys. Chem. B* **1997**, *101*, 10281.

[43] P. E. de Jongh, D. Vanmaekelbergh, *J. Phys. Chem. B* **1997**, *101*, 2716.

[44] G. Schlichthörl, S. Y. Huang, J. Sprague, a J. Frank, *J. Phys. Chem. B* **1997**, *101*, 8141.

[45] E. A. Ponomarev, L. M. Peter, *J. Electroanal. Chem.* **1995**, *396*, 219.

[46] H. S. Kim, I. Mora-Sero, V. Gonzalez-Pedro, F. Fabregat-Santiago, E. J. Juarez-Perez, N. G. Park, J. Bisquert, *Nat. Commun.* **2013**, *4*.

[47] H. S. Jung, N.-G. Park, *Small* **2015**, *11*, 10.

[48] A. Pockett, G. E. Eperon, T. Peltola, H. J. Snaith, A. Walker, L. M. Peter, P. J. Cameron, *J. Phys. Chem. C* **2015**, *119*, 3456.

[49] A. Dualeh, T. Moehl, N. Tetreault, J. Teuscher, P. Gao, M. K. Nazeeruddin, M. Grätzel, *ACS Nano* **2014**, *8*, 362.

[50] M. Saliba, T. Matsui, K. Domanski, J.-Y. Seo, A. Ummadisingu, S. M. Zakeeruddin, J.-P. Correa-Baena, W. R. Tress, A. Abate, A. Hagfeldt, M. Gratzel, *Science.* **2016**, *354*, 206.

[51] M. Saliba, T. Matsui, J.-Y. Seo, K. Domanski, J.-P. Correa-Baena, M. K. Nazeeruddin, S. M. Zakeeruddin, W. Tress, A. Abate, A. Hagfeldt, M. Grätzel, *Energy Environ. Sci.* **2016**, *9*, 1989.

[52] G. R. Desiraju, J. J. Vittal, A. Ramanan, *Cryst. Eng. A Textb.* **2011**.

[53] N. D. Pham, V. T. Tiong, P. Chen, L. Wang, G. J. Wilson, J. Bell, H. Wang, *J. Mater. Chem. A* **2017**, *5*, 5195.

[54] W. Zhang, M. Saliba, D. T. Moore, S. K. Pathak, M. T. Horantner, T. Stergiopoulos, S. D. Stranks, G. E. Eperon, J. A. Alexander-Webber, A. Abate, A. Sadhanala, S. Yao, Y. Chen, R. H. Friend, L. A. Estroff, U. Wiesner, H. J. Snaith, *Nat Commun* **2015**, *6*, 6142.

[55] C. Wang, D. Zhao, Y. Yu, N. Shrestha, C. R. Grice, W. Liao, A. J. Cimaroli, J. Chen, R. J. Ellingson, X. Zhao, Y. Yan, *Nano Energy* **2017**, *35*, 223.

[56] Q. Jiang, D. Rebollar, J. Gong, E. L. Piacentino, C. Zheng, T. Xu, *Angew. Chem. Int. Ed.* **2015**, *54*, 7617.

[57] L. Wang, D. Moghe, S. Hafezian, P. Chen, M. Young, M. Elinski, L. Martinu, S. Kéna-Cohen, R. R. Lunt, *ACS Appl. Mater. Interfaces* **2016**, *8*, 23086.

[58] S. Ye, H. Rao, Z. Zhao, L. Zhang, H. Bao, W. Sun, Y. Li, F. Gu, J. Wang, Z. Liu, Z. Bian, C. Huang, *J. Am. Chem. Soc.* **2017**, jacs. 7b01439.

[59] Y. Zhao, K. Zhu, *J. Phys. Chem. C* **2014**, *118*, 9412.

[60] M. Yang, Z. Li, M. O. Reese, O. G. Reid, D. H. Kim, S. Siol, T. R. Klein, Y. Yan, J. J. Berry, M. F. A. M. van Hest, K. Zhu, *Nat. Energy* **2017**, *2*, 17038.

[61] Y. Xia, C. Ran, Y. Chen, Q. Li, N. Jiang, C. Li, Y. Pan, T. Li, J. Wang, W. Huang, *J. Mater. Chem. A* **2017**, *5*, 3193.

[62] Q. Wu, P. Zhou, W. Zhou, X. Wei, T. Chen, S. Yang, *ACS Appl. Mate.r Interfaces* **2016**, *8*, 15333.

[63] D. Bi, P. Gao, R. Scopelliti, E. Oveisi, J. Luo, M. Grätzel, A. Hagfeldt, M. K. Nazeeruddin, *Adv. Mater.* **2016**, *28*, 2910.

[64] X. Li, M. I. Dar, C. Yi, J. Luo, M. Tschumi, S. M. Zakeeruddin, M. K. Nazeeruddin, H. Han, M. Gratzel, *Nat. Chem.* **2015**, *7*, 703.

[65] C.-C. Chueh, C.-Y. Liao, F. Zuo, S. T. Williams, P.-W. Liang, A. K.-Y. Jen, *J. Mater. Chem. A* **2015**, *3*, 9058.

Chapter 2.
Controlling Perovskite Crystal Growth

In this Chapter, we present a method to obtain a compact perovskite layer with larger grains, aiming for high performance perovskite solar cells with 19.5% power conversion efficiency. The mechanism of controlling perovskite crystal growth with ionic liquid, methylammonium formate (MAF) was demostrated. MAF can selectively interact with Pb, which can retard PbI$_2$-methylammonium iodide (MAI) interaction in the formation of the perovskite.

The main body of the work detailed in this Chapter resulted in the following publication: Seo, J.-Y. et al. Ionic Liquid Control Crystal Growth to Enhance Planar Perovskite Solar Cells Efficiency. *Adv. Energy Mater.*, **2016** 1600767

2.1   Introduction

Currently, the highest efficiency PSCs employ a mesoscopic (mp) TiO$_2$ electron contact, which is processed at temperatures above 400 °C and thus not compatible with the preparation of tandem devices. Although there are strategies to prepare mp-TiO$_2$ at low temperatures, the easiest approach would be to use a planar perovskite device without mesoporous layer.[1] We recently demonstrated low temperature processed SnO$_2$ as electron contact in planar PSCs for tandem silicon-perovskite solar cell.[2] Although the efficiency of our tandem device was one of the highest reported, the top planar PSC was poorly performing compared to a mesoscopic TiO$_2$ based device. Therefore, to profit from using perovskite in tandem with other photovoltaic materials, planar devices need to be improved.

In planar PSCs, the crystallinity, morphology, thickness, and surface coverage of perovskite film are critical for the device performance.[3] Several methods have been proposed to prepare high-quality perovskite layer, such as spin-coating, two-step sequential deposition, and vacuum vapor deposition.[4-7] Even though the one-step spin-coating method enabled among the highest efficiencies, the perovskite films frequently showed poor surface coverage, which results in a reduced cell perfor-

mance.[8] To overcome these issues, control of perovskite crystal growth and morphology has been widely investigated using several additives in the perovskite precursor solution.[9-11] Shahiduzzaman et al. made use of the low vapor pressure ionic liquid (IL) 1-hexyl-3-methylimidazolium chloride to control the film morphology by forming a uniform distribution of perovskite nanoparticles.[11] Moore et al. demonstrated that methylammonium formate can be used as an additive to produce higher quality, crystalline perovskite films.[10] Although these studies suggested that adding ILs in the perovskite precursor solution may help to prepare better solar cells, there are currently no reports that implemented this strategy to improve state-of-the-art planar PSCs.

In this work we demonstrate that ionic liquids enable the highest ever reported stabilized power conversion efficiency for a planar perovskite solar cell. Moreover, we show that compact perovskite films with larger crystalline domain can be prepared from solution by adding particular ionic liquids, such as methylammonium formate, to the precursors. Finally, we demonstrate that larger crystalline domains result in a more effective charge collection and thus better photovoltaic performances. We propose an IL-driven mechanism of crystallization as a new strategy to prepare high efficiency planar perovskite solar cells.

2.2   Results and Discussion

2.2.1   Selection of the Molecular Additive

In order to enable control of the perovskite crystal growth and morphology without changing the perovskite structure, we selected molecular cadidates as additives to the precursor solution based on their affinity for interaction with the perovskite precursor methylammonium iodide (MAI). First, we screened morphology changes of perovskite films with three candidate molecules which have the same cation (methylammonium) and different counter anions, namely formate ($HCOO^-$), nitrate (NO_3^-), chloride(Cl^-) or iodide (I^-), as shown in Figure 2.1a. The influence of the anion on the crystallization and morphology of the perovskite with 5 mol% of the additives in the perovskite precursor solution is shown in Figure 2.1b. In case of MACl, the films feature pinholes, since chloride can easily evaporate during the annealing process at 100 ºC. On the contrary, methylammonium nitrate (MAN) shows larger grain size, with a poor surface coverage. Finally, the MAF leads to smooth and pin-hole-free surfaces. Interestingly, MAF has special chemical properties of ionic liquids (ILs), which are well known for their extremely low vapor pressure that makes them non-volatile. This implies that if ILs are added in small amounts (few mol%) to the precursor solution, they remain in the perovskite film

after all the solvent has evaporated during the annealing process.[10,11] Therefore, in the course of this study we focused on the methylammonium formate (MAF) as an IL.[12]
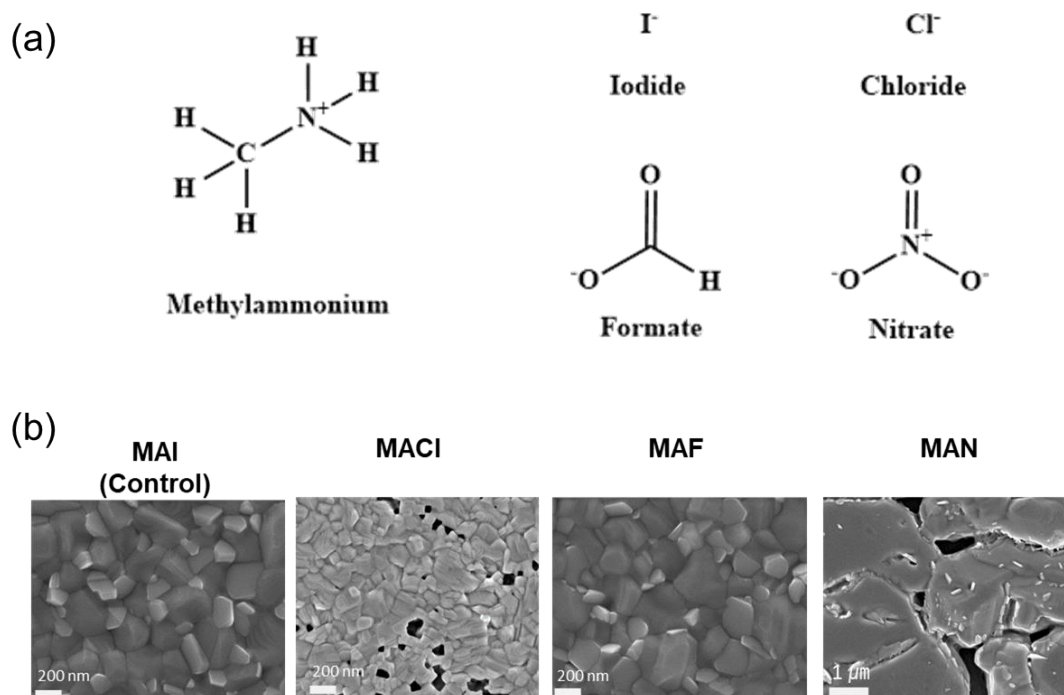

Figure 2.1. (a) Molecular structure of the organic precursors considered in this stady, namely methylammonium iodide (MAI), chloride (MACl), and formate. (MAF) (b) SEM images of perovskite films with different additive molecules in the perovskite precursor solutions.

2.2.2 Mechanism of Crystal Growth upon Treatment

Since HCOO⁻ is known to form the metal-organic complex with Pb^{2+}, we hypothesized that the HCOO⁻ influences the crystal growth of the perovskite through interaction with Pb^{2+}.[13] A schematic view of the proposed mechanism is depicted in Figure 2.2. First, HCOO⁻ coordinates Pb^{2+} in solution and during the early stage of the crystal growth (STEP 1). The HCOO⁻-Pb^+ complex is gradually displaced by Pb^+-I^- when films are heated to 100 °C (STEP 2), until HCOO⁻-Pb^+ coordination is completely replaced by Pb^+-I^- (STEP 3), enabling the crystal growth. Once the crystallization is completed, MAF occupies the surface of the perovskite crystals (as schematically presented in the Figure 2.2).

To understand the impact of the MAF on the crystal growth, we prepared perovskite precursor solutions with and without 5mol% of MAF. Perovskite films were coated onto SnO_2 layers that were deposited on FTO substrates by spin-coating the precur-

sor solution in a nitrogen filled glovebox by using the one-step anti-solvent method.[14] The images of the perovskite films collected every 5 s after posing the substrates on an hotplate at 100 °C are shown in Figure 2.3a. It is evident that the control film without MAF turns black earlier than the film with MAF, which suggested that the crystal growth is slowed down in the presence of MAF. To assess the impact of the slower crystal growth on the film morphology, we collected scanning electron microscopy (SEM) images of the film surface after 1 h of the annealing at 100 °C. SEM images of perovskite films show that the average grain sizes are 170 nm before the treatment, whereas the size increases to 325 nm upon addition of MAF. This observation suggests that the slower crystal growth induced larger average grain size. Furthermore, we notice that the MAF inhibits the formation of grains smaller than 150 nm, which represent a great portion of the size distribution in the film without the MAF (as shown by the statistical distribution in Figure 2.3b). Having elucidated the crystal growth mechanism, we further investigated its impact on the morphology and optical properties of the films.
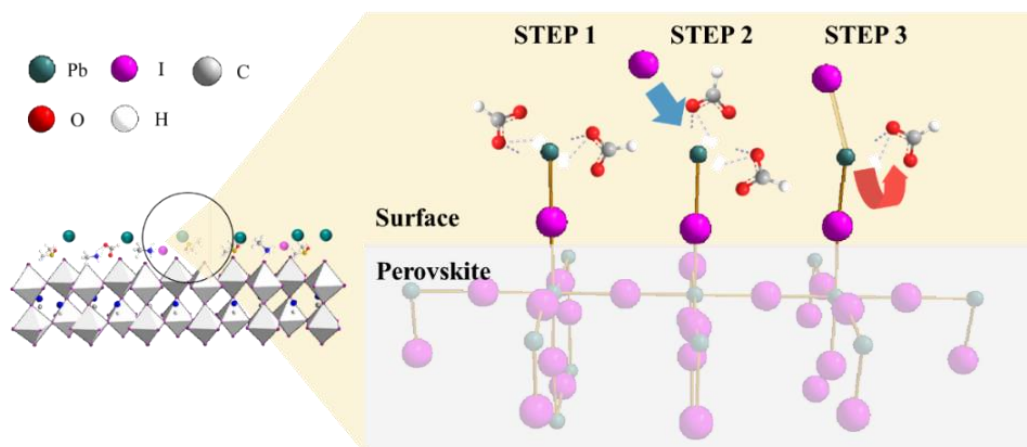

Figure 2.2. Schematic of the proposed perovskite crystal growth mechanism, as controlled by the formate anions.

2.2.3 Mophology and Optical Properties of Modified Perovskite Films

In order to investigate the impact of the MAF on the crystal structure of the perovskite, X-ray diffraction (XRD) patterns were collected from perovskite films with and without MAF on SnO_2/FTO substrates. The XRD spectra in Figure 3a show that the MAF mediated perovskite is rather similar to the non-MAF film (Figure 2.4). This indicates that HCOO[-] ions do not induce polymorphism or variation of the crystal lattice, despite the influence on the perovskite film morphology, as shown in Figure 2.3. Furthermore, the fact that the diffraction pattern remains the same, de-

spite the size of HCOO⁻ (Van der Waals radius of 249 pm) being larger than I⁻ (220 pm), suggests that HCOO⁻ is not incorporated into the perovskite crystal lattice.[12,15] It is interesting to note that the intensity of the (112), (211), (202) and (224) peaks relative to the intensity of the (110) peak (Figure 2.4, inset) is significantly higher in the film without MAF. Moreover, the Full Width at Half Maximum (FWHM) of the (110) XRD peak of the film treated with MAF decreases in comparison to that without MAF (Figure 2.5). This indicates a preferential crystal growth of (110) faces parallel to the interface, which are marginally thicker perpendicular to the interface (see Figure 2.3b).[16] This result is in accordance with the change in morphology we observed with the SEM imaging (Figure 2.3b).
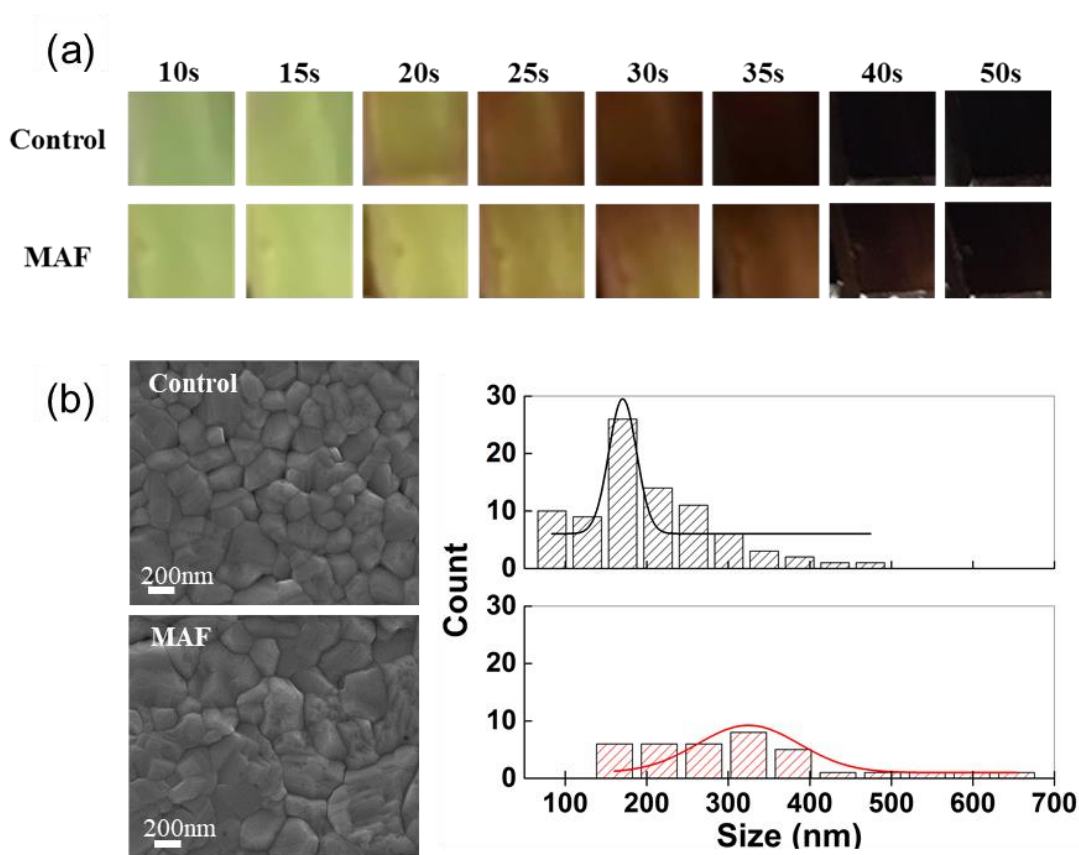
Figure 2.3 Morphological analysis of the perovskite films with and without MAF. (a) Pictures of perovskite films collected at subsequent delay times after posing the substrates on a hotplate at 100 °C. (b) (left) Top-view SEM images of perovskite films after 1 h of annealing at 100 °C. (right) Grain size distribution as estimated from the SEM images using Nano measurer 1.2 software.
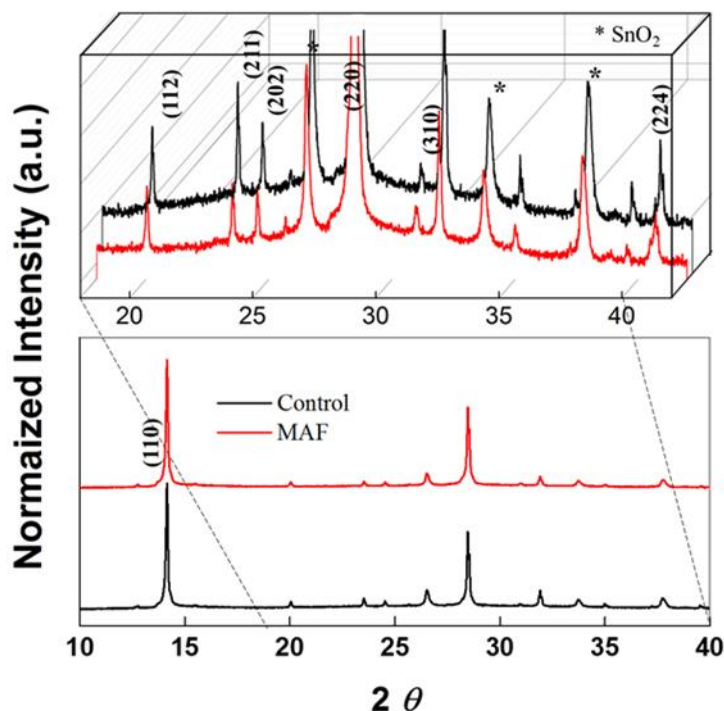
Figure 2.4. X-ray diffraction diagram of perovskite films deposited on SnO_2 substrates with and without MAF, the intensity is normalized to the peak at 14° (110). Inset: enlarged spectra displaying the relative intensities of the peaks between 18° and 42°.

Sample	Position (degree)	FWMH (degree)
Control	14.151	0.075481
MAF	14.154	0.074541
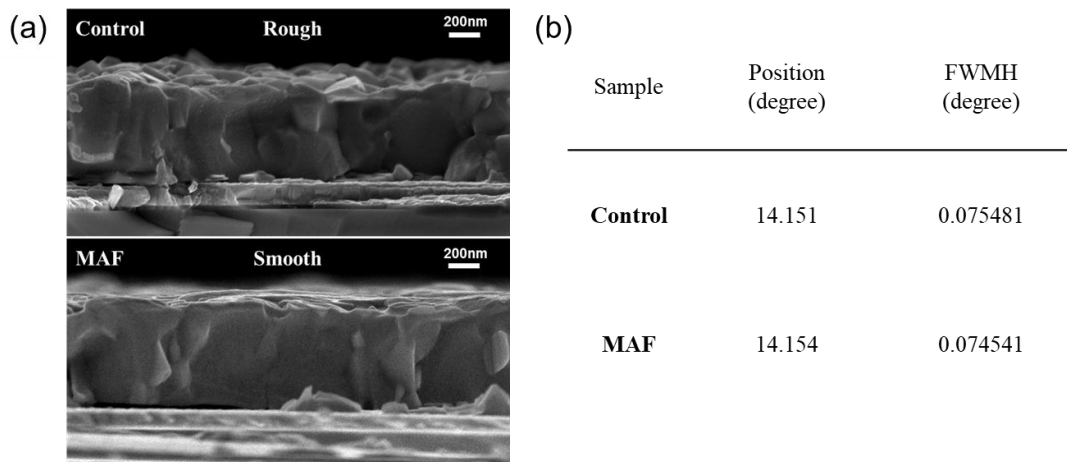
**Figure 2.5**. (a) SEM cross-section of a perovskite films on the ITO glasses. Control perovskite film shows rough surface induced by small crystals of perovskite. On the other hand, perovskite film with MAF has smooth and homogenous surface and almost single-grain crystals along horizontal (thickness) direction. (b) X-ray diffraction (110) peak full width at half maximum (FWHM) from the spectrum in Figure 2.4.

2.2.4 Photovoltaic Peroperties

Planar perovskite solar cells (PSCs) with and without MAF in perovskite precursor solution were prepared on compact SnO_2, following the procedures previously reported by Correa-Baena *et al.*[17] Figure 2.6a displays the current density-voltage (*J-V*) curves of the best PSCs with the corresponding metrics reported in Table 2.1. The data shows that MAF improves the short circuit current density (J_{sc}) by approximately 1 mA/cm^2. This was confirmed by the incident photon-to-current efficiency (IPCE), as shown in Figure 2.6b. We notice that the integrated current density is lower than what is measured from the *J-V* curves, with and without MAF. This trend has been systematically observed and reported previously, and it can in part be attributed to a small spectral mismatch between the solar simulator and the standard AM 1.5 G emission.[14,18] In Figure 2.6c we reported the statistical analyses of the maximum PCE collected from 7 independent devices, which confirmed the improvement with MAF. Moreover, to rule out the impact of the hysteresis on the estimated PCE, we tracked the device maximum power output for 5 min order to extract the stabilized maximum PCE (Figure 2.6d). It was found that the PCE stabilizes after about 50 s at 18.9% for the control and 19.5% for MAF device (see Table 2.1), which is in agreement with the values extracted from the *J-V* curves shown in Figure 2.6a. As our best control device matches the highest reported stabilized PCE for planar PSCs (~19%),[19,20] our findings highlight that the MAF treatment leads to improving the state-of-the-art, reaching a new record for planar PSC of 19.5% stabilized PCE.

**Table 2.1.** Photovoltaic parameters of champion devices with and without MAF.

	Scan Direction	Champion Devices					Average of 7 devices			
		J_{sc} mA cm^2	V_{oc} V	FF	PCE %	Stab. PCE %	J_{sc} mA/cm^2	V_{oc} V	FF	PCE %
CON	Backward	21.7	1.16	0.72	19.1		21.2	1.15	0.72	18.0
						18.9				
	Forward	21.7	1.15	0.69	18.1		±0.7	± 0.01	± 0.01	± 0.8
MAF	Backward	22.7	1.14	0.71	19.5		21.7	1.16	0.72	18.8
						19.5				
	Forward	22.7	1.13	0.69	18.6		± 0.8	± 0.02	± 0.02	± 0.6
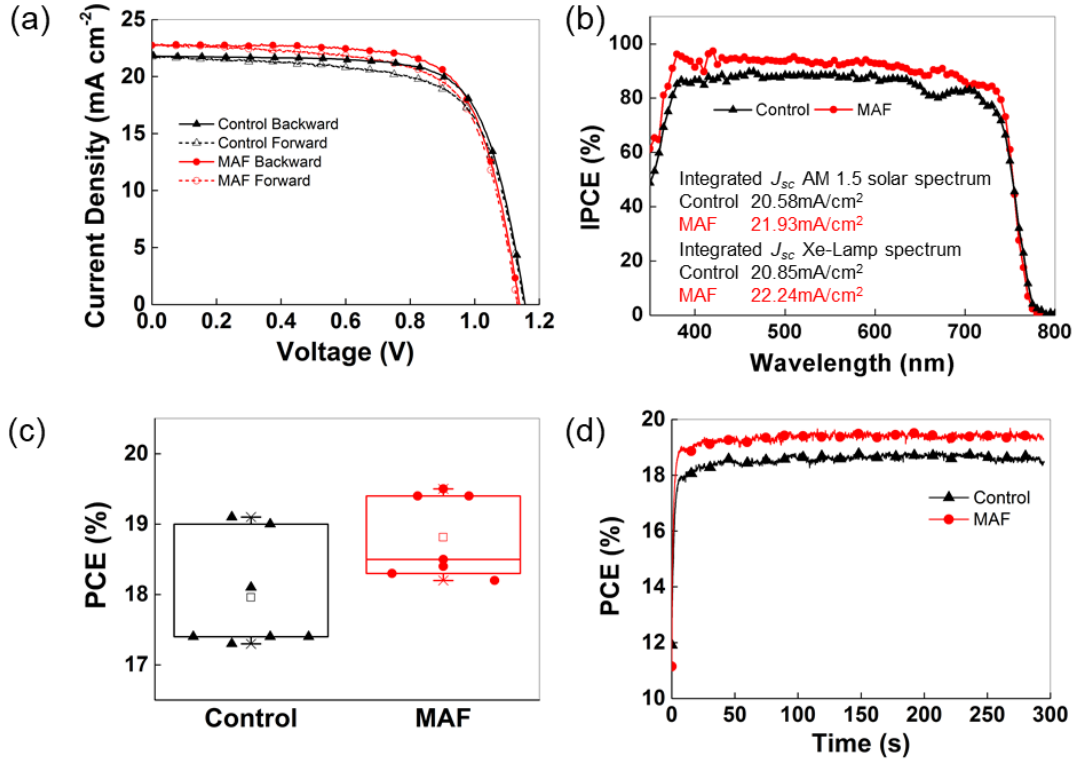
Figure 2.6. Photovoltaic metrics of perovskite solar cells prepared with and without MAF. (a) *J-V* curves were measured from forward bias to short circuit condition and vice versa at the scan rate of 10 mV/s under AM1.5 simulated solar light (94.8 mW/cm^2). The device active area was defined using a black metal shadow mask with an aperture of 0.16 cm^2. (b) Incident photon-to-current efficiency (IPCE) curve (solid line) and the integrated photocurrent (dashed line) for the MAF device. (c) Box plot of the PCE collected from 7 devices. (d) Maximum power conversion efficiency as function of time was extracted from the maximum power point tracking under AM1.5 simulated solar light.

In order to investigate the origin of the improved performances upon the MAF treatment, we performed intensity modulated photocurrent spectroscopy.[21] In Figure 2.7, we report the imaginary component frequency spectra of the current response to the light intensity modulated (10% of the stationary value) around 100 mW/cm^2 for devices with and without MAF. The spectra show three main features, which have been already reported by Correa-Baena *et al.* for similar planar PSCs.[22] The peak at low frequency (0.1 Hz – 100 Hz) has been correlated to the resonant frequencies of the ions and ion vacancies migration within the perovskite lattice. Here, we note that the peak of the MAF device is shifted towards higher frequency, indicating a faster ion migration. This is in line with the trend reported by Correa-Baena *et al.*, who demonstrated ions migrating faster in perovskite films composed

of larger grains. Moving to higher frequency, two more peaks are observed that have been assigned to the resonant frequencies of the charge dynamics within the perovskite and the other device components, such as the hole and the electron transporting layers. While the peak at highest frequency (fast charge dynamics) is rather similar with and without MAF, the peak at intermediated frequency (1 kHz – 100 KHz) is clearly visible only in the control, and almost vanishes in the MAF device. As we have previously shown, this peak provides information on the slow charge transport dynamics within the device.[23] The fact that its intensity is significantly lower suggests that the slow charge transport pathways are inhibited by the MAF. This behavior correlates with the crystal size distribution we presented in Figure 2.3b, where we showed that MAF reduces the formation of grains smaller than 150 nm, which represent a great portion of the size distribution in the film without the MAF. The cross-sectional SEM images (Figure 2.5a) of a perovskite film with MAF shows that larger grains can cross the whole thickness of the perovskite film, thus forming a sort of local single crystalline devices. The charge transport through a single crystal is significantly faster than through the grain boundaries of a polycrystalline film.[24,25] Therefore, inhibiting the formation of small crystals eliminates the slow charge transport pathways, which results in better device performances.
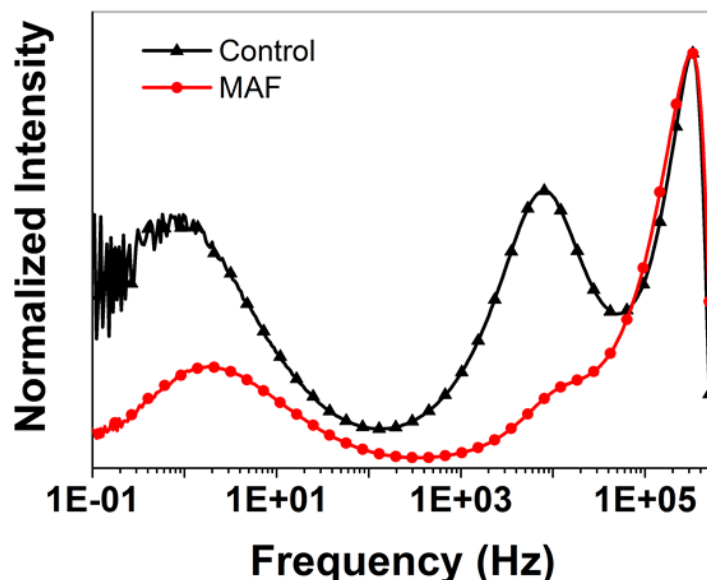
Figure 2.7. Imaginary component frequency spectra of the current response to the light intensity modulated around 100 mW cm^2 for devices with and without MAF. The intensities are normalized to the maximum value.

2.3   Conclusions

In conclusion, we reported planar perovskite solar cells with a record stabilized power conversion efficiency of 19.5%. We demonstrated that controlling the grain size distribution within the perovskite film is crucial to improve the state-of-the-art devices. We made use of a specific ionic liquid, methylammonium formate, to retard the perovskite crystal growth in order to form a compact layer with larger grain sizes. Powder XRD analysis showed that MAF induces formation of thicker and larger crystals perpendicular and parallel to the interface. Consequently, planar perovskite solar cells prepared with MAF exhibited more effective charge transport, which results in higher power conversion efficiency compared to the state-of-the-art devices. Using ionic liquids to control the morphology of the perovskite film is a simple, general, and effective method to enhance the efficiency of planar perovskite solar cells. Further advances are expected from using other ionic liquids that can selectively interact with the different elements composing the perovskite crystals.

2.4   Experimental

Chemicals and Reagents. All reagents and solvents, except methylammonium formate, were purchased from commercial sources and used without further purification, unless otherwise noted.

Chemical characterization. ^{1}H NMR spectra were obtained using a Bruker spectrometer (400 MHz) is reported in ppm using DMSO-*d$_6$* as an internal standard. X-ray powder (XRD) diagrams were recorded on an X'Pert MPD PRO (Panalytical) equipped with a ceramic tube (Cu anode, $\lambda = 1.54060$ Å), a secondary graphite (002) monochromator and a RTMS X'Celerator (Panalytical) in an angle range of $2\theta = 10°$ to $40°$.

Methylammnonium formate (MAF) was synthesized using a previously reported procedure.[17] CH$_3$NH$_3$(HCOO) was synthesized by dropping slowly 6 mL of formic acid (88wt% in water) in methanol to a solution of 20 mL methylamine (40wt% in water) in 10 mL absolute ethanol cooled at 0 °C. After mixing reagent, the solution was further stirred for 1h at 0 °C under vacuum. The solution was then dried at room temperature under vacuum for 2 days. ^{1}H NMR (400 MHz, DMSO-*d$_6$*): 2.30 (s, 3H), 8.40 (s, 1H) 8.64 (s, 3H).

Solar cells fabrication. Devices were fabricated on fluorine doped tin oxide (FTO) coated glass substrates. The substrates were cleaned sequentially with Hellmanex in ultrasonic bath for 30 min, then washed with acetone, isopropanol, and finally cleaned with oxygen plasma for 5 min. Electron selective layer preparation FTO

substrates were cleaned first with acetone, then for 10 min in piranha solution (H_2SO_4/H_2O_2 3:1 v/v) and then for 10 min in a plasma cleaner prior to ALD deposition. SnO_2 was deposited at 118 °C using TDMASn (99.99%-Sn, Strem Chemicals INC) and ozone at a constant growth rate of 0.065 nm per cycle measured by ellipsometry. TDMASn was held at 65 °C. Ozone was produced using an ozone generator (AC-2025, IN USA Incorporated) fed with oxygen gas (99.9995% pure, Carbagas) producing a concentration of 13% ozone in oxygen. Nitrogen was used as a carrier gas (99.9999% pure, Carbagas) with a flow rate of 10 sccm. Before perovskite deposition, the pre-made ALD layers were treated with UV ozone for 10 min to remove by-products from the deposition process. The perovskite films were deposited from a precursor solution containing MAI (1.1M, Dysol) and PbI_2 (1.1M, TCI Chemicals) in anhydrous DMSO (Acros) for $MAPbI_3$, FAI (1.1 M, Dyesol), PbI_2 (1.2 M, TCI Chemicals), MABr (0.2 M, Dyesol) and $PbBr_2$ (0.2 M, TCI Chemicals) in anhydrous DMF/DMSO 4:1 (v/v, Acros) for mixed perovskite. MAF was then added to the perovskite solution (5 mol% vs. perovskite). The spin coating program includes two steps, first 1000 rpm for 10 s with a ramp of 200 rpm s^{-1}, then 6000 rpm for 30 s with a ramp of 2000 rpm s^{-1}; 15 s before the end of the spin-coating program, chlorobenzene was carefully dropped on the spinning substrate. The substrate was then heated at 100 °C for 1 h on a hotplate in the nitrogen-filled glovebox. The HTM was subsequently deposited on the top of the perovskite layer by spin-coating from solution at 4000 rpm for 20 s with a ramp of 2000 rpm s^{-1}. The HTM solution was prepared by dissolvin spiro-OMeTAD in chlorobenzene at the concentration of 70 mM, with the addition of 50 mol% of Li-TFSI (Sigma-Aldrich) from a stock solution of 1.8 M in acetonitrile, 330 mol% of tBP (Sigma-Aldrich) and 3mol% of FK209 (Dyesol) from a stock solution 0.25 M in acetonitrile. Finally, 80 nm gold layer was deposited by thermal evaporation under high vacuum, using a shadow masking to pattern the electrodes.

Perovskite film characterization. A ZEISS Merlin HR-SEM was used to characterize the morphology of the device top view and cross-section. X-ray powder (XRD) diagrams were recorded on an X'Pert MPD PRO (Panalytical) equipped with a ceramic tube (Cu anode, λ = 1.54060 Å), a secondary graphite (002) monochromator and a RTMS X'Celerator (Panalytical) in an angle range of 2θ = 10° to 40°. Absorption spectral measurements were recorded using Varian Cary5 UV–visible spectrophotometer. Photoluminescence spectra were obtained with Florolog 322 (Horiba Jobin Ybon Ltd) with the range of wavelength from 620 to 850 nm by exciting at 460 nm. The samples were mounted at 60° and the emission recorded at 90° from the incident beam path.

Solar cell characterization. Current-voltage characteristics were recorded by applying an external potential bias to the cell while recording the generated photocurrent with a digital source meter (Keithley Model 2400). The light source was a 450 W Xenon lamp (Oriel) equipped with a SchottK113 Tempax sunlight filter (Praezisions Glas & Optik GmbH) to match the emission spectrum of the lamp to the AM1.5G standard. Before each measurement, the exact light intensity was determined using a calibrated Si reference diode equipped with an infrared cut-off filter (KG-3, Schott). The scan rate was 10 mV s^{-1}. Maximum power point tracking was performed with Keithley model 2400 driven by a homemade algorithm developed in IgorPro software. The cell was initially biased at 1 V. The bias voltage was decreased of 5 mV each 500 ms towards the maximum power point. For each voltage step the algorithm evaluates if the derivative of the power over the time is positive or negative. If the derivative is positive the scan direction remains the same. On the contrary, the algorithm changes direction if the derivative is negative. When the bias voltage reaches the maximum power point the applied bias oscillates within 10–15 mV perturbing and observing continuously the solar cell under illumination. IPCE spectra were recorded as functions of wavelength under a constant white light bias of approximately 10 mW cm^2 supplied by an array of white light emitting diodes. The excitation beam coming from a 300 W Xenon lamp (ILC Technology) was focused through a Gemini-180 double monochromator (Jobin Yvon Ltd) and chopped at approximately 2 Hz. The signal was recorded using a Model SR830 DSP Lock-In Amplifier (Stanford Research Systems). All measurements were conducted using a non-reflective metal aperture of 0.16 cm^2 to define the active area of the device and avoid light scattering through the sides. Intensity modulated photocurrent spectroscopy was performed using Autolab PGSTAT302N according to procedures reported previously.[21]

References

[1] Z. L. Ku, Y. G. Rong, M. Xu, T. F. Liu, H. W. Han, *Sci. Rep-Uk.* **2013**, *3*.

[2] S. Albrecht, M. Saliba, J. P. C. Baena, F. Lang, L. Kegelmann, M. Mews, L. Steier, A. Abate, J. Rappich, L. Korte, R. Schlatmann, M. K. Nazeeruddin, A. Hagfeldt, M. Graetzel, B. Rech, *Energ. Environ. Sci.* **2016**, *9*, 81-88.

[3] H. J. Snaith, A. Abate, J. M. Ball, G. E. Eperon, T. Leijtens, N. K. Noel, S. D. Stranks, J. T. W. Wang, K. Wojciechowski, W. Zhang, *J. Phys. Chem. Lett.* **2014**, *5*, 1511-1515.

[4] C. S. Ponseca, T. J. Savenije, M. Abdellah, K. B. Zheng, A. Yartsev, T. Pascher, T. Harlang, P. Chabera, T. Pullerits, A. Stepanov, J. P. Wolf, V. Sundstrom, *J. Am. Chem. Soc.* **2014**, *136*, 5189-5192.

[5] W. S. Yang, J. H. Noh, N. J. Jeon, Y. C. Kim, S. Ryu, J. Seo, S. I. Seok, *Science* **2015**, *348*, 1234-1237.

[6] Q. Chen, H. P. Zhou, Z. R. Hong, S. Luo, H. S. Duan, H. H. Wang, Y. S. Liu, G. Li, Y. Yang, *J. Am. Chem. Soc.* **2014**, *136*, 622-625.

[7] F. Z. Huang, Y. Dkhissi, W. C. Huang, M. D. Xiao, I. Benesperi, S. Rubanov, Y. Zhu, X. F. Lin, L. C. Jiang, Y. C. Zhou, A. Gray-Weale, J. Etheridge, C. R. McNeill, R. A. Caruso, U. Bach, L. Spiccia, Y. B. Cheng, *Nano Energy* **2014**, *10*, 10-18.

[8] D. Bi, W. Tress, M. I. Dar, P. Gao, J. Luo, C. Renevier, K. Schenk, A. Abate, F. Giordano, J. P. Correa Baena, J. D. Decoppet, S. M. Zakeeruddin, M. K. Nazeeruddin, M. Graetzel, A. Hagfeldt, *Sci. Adv.* **2016**, *2*, e1501170.

[9] P. W. Liang, C. Y. Liao, C. C. Chueh, F. Zuo, S. T. Williams, X. K. Xin, J. Lin, A. K. Jen, *Adv. Mater.* **2014**, *26*, 3748-3754.

[10] D. T. Moore, K. W. Tan, H. Sai, K. P. Barteau, U. Wiesner, L. A. Estroff, *Chem. Mater.* **2015**, *27*, 3197-3199.

[11] M. Shahiduzzaman, K. Yamamoto, Y. Furumoto, T. Kuwabara, K. Takahashi, T. Taima, *Rsc Adv* **2015**, *5*, 77495-77500.

[12] J. P. Belieres, C. A. Angell, *J. Phys. Chem. B* **2007**, *111*, 4926-4937

[13] J. Catalano, A. Murphy, Y. Yao, G. P. A. Yap, N. Zumbulyadis, S. A. Centeno, C. Dybowski, *Dalton Trans.* **2015**, *44*, 2340-2347.

[14] N. J. Jeon, J. H. Noh, Y. C. Kim, W. S. Yang, S. Ryu, S. Il Seol, *Nat. Mater.* **2014**, *13*, 897-903.

[15] F. Holtzberg, B. Post, I. Fankuchen, *J. Chem. Phys.* **1952**, *20*, 198-198.

[16] I. M. Hermes, S. A. Bretschneider, V. W. Bergmann, D. Li, A. Klasen, J. Mars, W. Tremel, F. Laquai, H. J. Butt, M. Mezger, R. Berger, B. J. Rodriguez, S. A. L. Weber, *J. Phys. Chem. C* **2016**, *120*, 5724-5731.

[17] J. P. Correa-Baena, L. Steier, W. Tress, M. Saliba, S. Neutzner, T. Matsui, F. Giordano, T. J. Jacobsson, A. R. S. Kandada, S. M. Zakeeruddin, A. Petrozza, A. Abate, M. K. Nazeeruddin, M. Gratzel, A. Hagfeldt, *Energ. Environ. Sci.* **2015**, *8*, 2928-2934.

[18] J. W. Lee, T. Y. Lee, P. J. Yoo, M. Gratzel, S. Mhaisalkar, N. G. Park, *J. Mater. Chem. A* **2014**, *2*, 9251-9259.

[19] J. H. Heo, M. H. Lee, H. J. Han, B. R. Patil, J. S. Yu, S. H. Im, *J. Mater. Chem. A* **2016**, *4*, 1572-1578.

[20] Y. Shao, Y. Yuan, J. Huang, *Nat. Energy* **2016**, *1*, 15001.

[21] K. Zhu, N. Kopidakis, N. R. Neale, J. van de Lagemaat, A. J. Frank, *J. Phys. Chem. B* **2006**, *110*, 25174-25180.

[22] Baena, J. P. C. Anaya. M; Lozano.G, *Adv. Mater* **2016** doi: 10.1002/adma.201600624.

[23] F. Giordano, A. Abate, J. P. Correa Baena, M. Saliba, T. Matsui, S. H. Im, S. M. Zakeeruddin, M. K. Nazeeruddin, A. Hagfeldt, M. Graetzel, *Nat. Commun.* **2016**, *7*, 10379.

[24] W. Zhang, M. Saliba, D. T. Moore, S. K. Pathak, M. T. Horantner, T. Stergiopoulos, S. D. Stranks, G. E. Eperon, J. A. Alexander-Webber, A. Abate, A. Sadhanala, S. Yao, Y. Chen, R. H. Friend, L. A. Estroff, U. Wiesner, H. J. Snaith, *Nat. Commun.* **2015**, *6*, 6142.

[25] J. H. Im, I. H. Jang, N. Pellet, M. Gratzel, N. G. Park, *Nat. Nanotechnology* **2014**, *9*, 927-932.

Chapter 3.

Cesium-Containing Triple Cation Perovskites as Light Harvesting Materials

In this Chapter, we describe the effect of cesium in mixed catrion (MA/FA) perovskites on the room temperature crystallization and show great potential for low temperature process of device fabrication.

The main body of the work detailed in this Chapter resulted in the following publication: Matsui, T.[#], Seo, J. Y. [#] et al. Room-Temperature Formation of Highly Crystalline Multication Perovskites for Efficient, Low-Cost Solar Cells. *Adv. Mater.*, **2017**, 29. # Authors contributed equally to this work.

3.1   Introduction

Perovskite solar cells (PSCs) based on lead halide $APbX_3$ (where A is a monovalent cation, X is a halide) continue to attract large attention, exhibiting currently a certified efficiency of 22.7%,[1] which exceeds that of commercial polycrystalline silicon solar cells.[2] This has prompted strong interest in the development of PSCs for large-scale practical deployment. Since PSCs can be manufactured by solution methods, judicious process design is of primary concern for commercialization, targeting especially lower cost methods compared with other solar cells. However, state-of-the-art perovskite materials that are mostly used for PSCs, such as $MAPbI_3$ or $FAPbI_3$ (MA = methylammonium, $CH_3NH_3^+$; FA = formamidinium, $CH(NH_2)_2^+$), require annealing at 70–150 °C for 30–60 min to form the black crystalline photoactive layer.[3-5] This process is not suitable for mass production. On the contrary, the roll-to-roll fabrication is a very attractive way for mass production, however the 30-60 min annealing process not only decreases throughput, but also requires large processing areas and annealing equipment, apart from consuming energy.

One way to address this problem is to employ an instant flash annealing technique, as reported by J.Troughton et al. initially, and other researchers who used NIR heat-

ing or photonic flash sintering.[6-10] Another approach is to avoid the annealing step altogether. Recently, there are several reports that appeared on A-cation combinations, such as FA and Cs and/or MA perovskite formulations to yield black photoactive perovskite phase without annealing.[11,12] PSCs have been prepared at RT in a short time with efficiency of 15-17% by two step sequential method[13] and one step method.[14,15] Zhou et al. showed room-temperature fabrication of perovskite layer by dipping spin-coated perovskite film into diethyl ether solvent bath to remove residual N-methyl-2-pyrrolidone solvent, yielding 15.2% PCE. Also, Yin et al. showed room-temperature fabrication of perovskite layer by casting ethyl acetate during spin-coating of perovskite precursor solution to remove mixture of g-butyrolactone (GBL) and dimethyl sulfoxide (DMSO), yielding 16.6% PCE.[15] Their concept is replacing the high boiling point solvents that is necessary for dissolving perovskite precursor by a volatile solvents to initiate crystallization.

Our work demonstrates that Cs ions in combination with MA facilitate greatly the rapid room temperature crystallization of perovskites. Moreover, we explore the role of Cs and MA ions in enhancing crystal formation. The device with optimized A-cation composition of $FA_{0.8}MA_{0.1}Cs_{0.1}$ showed a solar to electric power conversion efficiency (PCE) of 18.0%. Our method provides an attractive path to room temperature fabrication of PSCs by low-cost, large-scale manufacturing, such as the roll-to-roll process.

## 3.2   Results and Discussion

3.2.1   Characterization of Perovskite Films

We investigated FA/MA/Cs triple cation formulations for room temperature perovskites since they form high efficiency PSCs.[12],[16-19] Additionally, we explored low temperature, photoactive perovskite phase with combination of FA/MA, FA/Cs or FA/MA/Cs.[11],[20] From our previous study, we achieved the best efficiency by the $(FA_{0.79}MA_{0.16}Cs_{0.05})Pb(I_{0.83}Br_{0.17})_3$ composition.[12] Therefore, we fixed the the I/Br ratio as 0.83/0.17, and FA ratio of 0.8 as a framework, while varied MA/Cs ratios that were assumed to have an important role in the crystallization process. For convenience, we describe the $(FA_{0.8}MA_{0.2-x}Cs_x)Pb(I_{0.83}Br_{0.17})_3$ perovskite formulations as $FA_{0.8}MA_{0.2-x}Cs_x$. We spin coated the films and kept it for 5 min at room temperature (RT). For comparison, we also annealed films at 100 °C for 30 min.

The effect of the MA/Cs ratio on the photoluminescence (PL) emission spectra and UV-vis absorption spectra of the room temperature (RT) processed perovskite films are shown in Figure 3.1a. The data indicate a clear blue shift in the UV-vis absorp-

tion and PL with increasing Cs content, presumably due to lattice contraction in presence of the small Cs ions. While the Cs-free non-annealed $FA_{0.8}MA_{0.2}Cs_0$ sample is not fully converted to the perovskite phase at RT as shown in XRD (Figure 3.1b), the blue shift of the absorption and the emission indicates that mixed cations FA/MA/Cs are incorporated in the perovskite lattice.

In order to further assess the incorporation of the cations into the perovskite lattice, the films are analyzed by X-ray diffraction (XRD). Figure 3.1b shows the XRD patterns of the perovskite with different MA/Cs ratios for the films processed at RT. The (110) peak exhibits a strong intensity compared to the annealed Cs-free films. However, upon increasing the Cs/MA ratio, the relative intensity of the (112) peak is increased. This indicates that larger amounts of Cs affect the crystal orientation, which is in accordance with Cs incorporation into the lattice, yet it can be unfavorable for the device performance.[21] Upon annealing perovskite films after dripping anti-solvent, stabilized perovskite phases are formed in all conditions by suppressing the δ-phase (Figure 3.1c,d). On the contrary, for un-annealed films, formulations with less than 10% Cs exhibit several peaks between 5-10 degrees in the XRD patterns, arising from an intermediate $MA_2Pb_3I_8 \cdot 2DMSO$ phase (Figure 3.1b).[22] This indicates that films with less than 10% Cs are not fully converted to perovskite phase at RT. Also, these formulations contain some yellow (δ) phase of $FAPbI_3$, which is undesirable for photovoltaic applications. Importantly, upon addition of 10% Cs, the δ-phase completely vanishes.
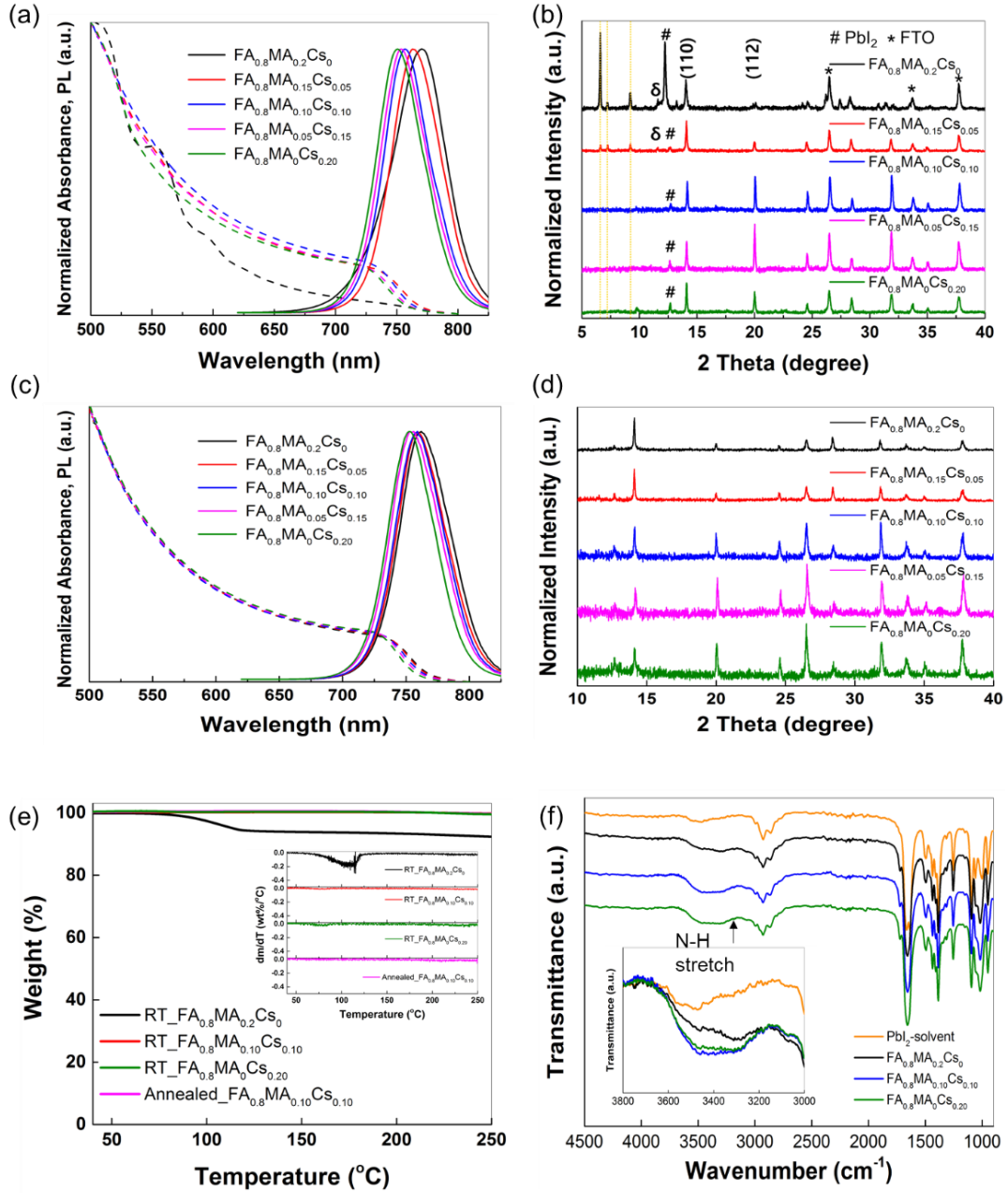
Figure 3.1. (a,c) PL and UV-vis absorption (dashed line) and (b,d) XRD spectra of the films either room temperature (RT) prepared and 100 °C annealed $FA_{0.8}MA_{0.2-x}Cs_x$ films of varying Cs content x. The orange colored dashed vertical lines in the XRD spectrum indicate the peak positions of the $MA_2Pb_3I_8 \cdot 2DMSO$ intermediate phase. (e) TGA curves and their first derivatives (insert) of $FA_{0.8}MA_{0.2-x}Cs_x$ powder. Heating rate is 5 °C/min (f) Fourier transform infrared spectrometer (FTIR) spectra of perovskite solution of $FA_{0.8}MA_{0.2-x}Cs_x$. Insert shows enlarged curves in the range of NH vibration from 3800 cm^{-1} to 3000 cm^{-1}.

Thermogravimetric analysis (TGA) was further performed to detect any residual solvent (Figure 3.1d), which is especially important for non-annealed films. Interestingly, the RT Cs-free ($FA_{0.8}MA_{0.2}Cs_0$) films show significant weight loss from temperatures around 70 °C, which corresponds to the evaporation temperature of DMF and DMSO.[23] However, the un-annealed films with the $FA_{0.8}MA_{0.1}Cs_{0.1}$ and $FA_{0.8}MA_0Cs_{0.2}$ composition display almost no weight loss, similarly to the annealed film. This indicates that the Cs-containing films enclose almost no residual solvent, which is in good agreement with the XRD data. In the absence of Cs, however, the perovskite undergoes strong complexation by DMSO, forming stable $DMSO-PbI_2$ or $MAI-DMSO-PbI_2$ complexes,[24] from which it is hard to remove the solvent (Figure 3.3). To confirm this hypothesis, we conducted FTIR for $FA_{0.8}MA_{0.2-x}Cs_x$ perovskite precursor solutions to observe the intermolecular interactions in solution (Figure 3.1f). FTIR shows that N-H stretching at 3300–3500 cm^{-1} becomes stronger when the Cs^+ is added to FA/MA perovskite precursor solution. This corresponds to hydrogen bonding interaction ($N^+-H\cdots I$) between the organic salts (MA^+/FA^+) and iodide of the $[PbI_6]^{4-}$ octahedra.[15],[25-28] This causes a contraction of the distance of adjacent $[PbI_6]^{4-}$ octahedral even in the solution state. Thus, we conclude that Cs helps not only stabilizing the α-phase, but also prevents incorporation of the solvent, facilitating the room temperature crystallization of the perovskite phase.

The effect of Cs ions on the film morphology was assessed by scanning electron microscopy (SEM). Figure 3.2 shows the SEM images of $FA_{0.8}MA_{0.2-x}Cs_x$ films for various Cs contents before annealing. The grain size of perovskite crystal becomes larger with increasing the MA/Cs ratio. To investigate whether this effect is related to MA, we also prepared the MA-free $FA_{0.9}MA_0Cs_{0.1}$ film. Comparing $FA_{0.9}MA_0Cs_{0.1}$ and $FA_{0.8}MA_{0.1}Cs_{0.1}$, we can observe larger crystals in $FA_{0.9}MA_0Cs_{0.1}$. In addition, XRD of the film with MA ($FA_{0.8}MA_{0.1}Cs_{0.1}$) shows less full width with half maximum (FWMH) value of (110) peak than that of the film without MA ($FA_{0.9}MA_0Cs_{0.1}$), which indicates that the film containing MA features better crystallinity (Figure 3.2e). Thus we conclude that MA helps to increase the grain size and crystallinity, presumably due to the interaction with DMSO[24]. Therefore, especially in non-annealed perovskites, both Cs and MA are necessary to convert the precursor to a pure photoactive perovskite phase of high quality crystals.
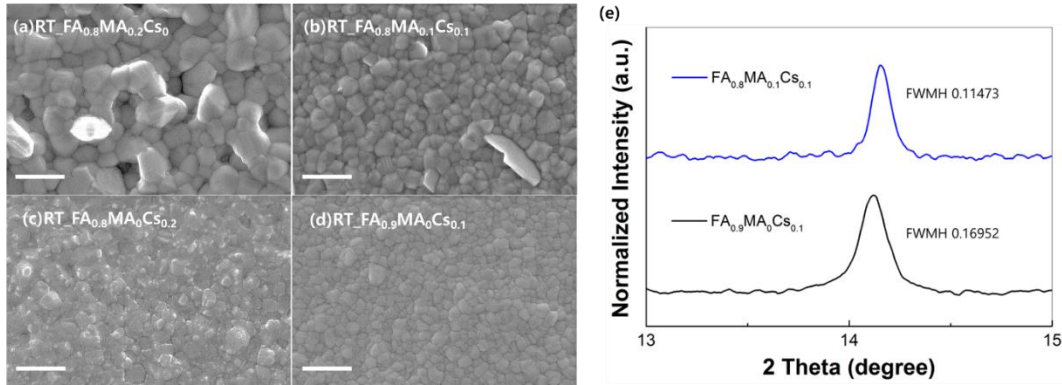
Figure 3.2. SEM image of perovskite films (a)$FA_{0.8}MA_{0.2}Cs_0$ (b)$FA_{0.8}MA_{0.1}Cs_{0.1}$ (c)$FA_{0.8}MA_0Cs_{0.2}$ (d)$FA_{0.9}MA_0Cs_{0.1}$ before annealing (Scale bar is 500 nm). (e) XRD spectra and calculated FWMH value from (110) peak of non-annealed $FA_{0.9}MA_0Cs_{0.1}$ and $FA_{0.8}MA_{0.1}Cs_{0.1}$ films.

3.2.2 Mechanism of Perovskite Formation

Based on charaterization of cesium containing perovskite solutions and films, the results indicates that Cs interacts strongly with the $[PbI_6]^{4-}$octahedra, replacing the intercalated solvent[11] and we establish the mechanism of perovskite formation for FA/MA perovskite and Cs/FA/MA perovskite. In case of double cation FA/MA perovskite, the intermediate phase of $MA_2Pb_3I_8 \cdot 2DMSO$ is formed with edge-sharing $[PbI_6]^{4-}$ octahedral layers after anti-solvent treatment to FA/MA(Figure 3.1b). Then, intermediate phase is converted to photoactive perovskite phase via solvent/cation exchange between octahedral layers after thermal annealing. In case of triple cation Cs/FA/MA perovskite, Cs is intercalated and pushes out solvent molecules from between the $[PbI_6]^{4-}$ octahedral layers since the intermolecular interaction of Cs-$[PbI_6]^{4-}$ is strong enough to remove the solvents when anti-solvent is treated on the films (Figure 3.1f). Immediately the perovskite film turnes to photoactive perovskite phase by Cs effect. Additional annealing process can enhances the crystallinity of perovskite (Figure 3.1d).[29]
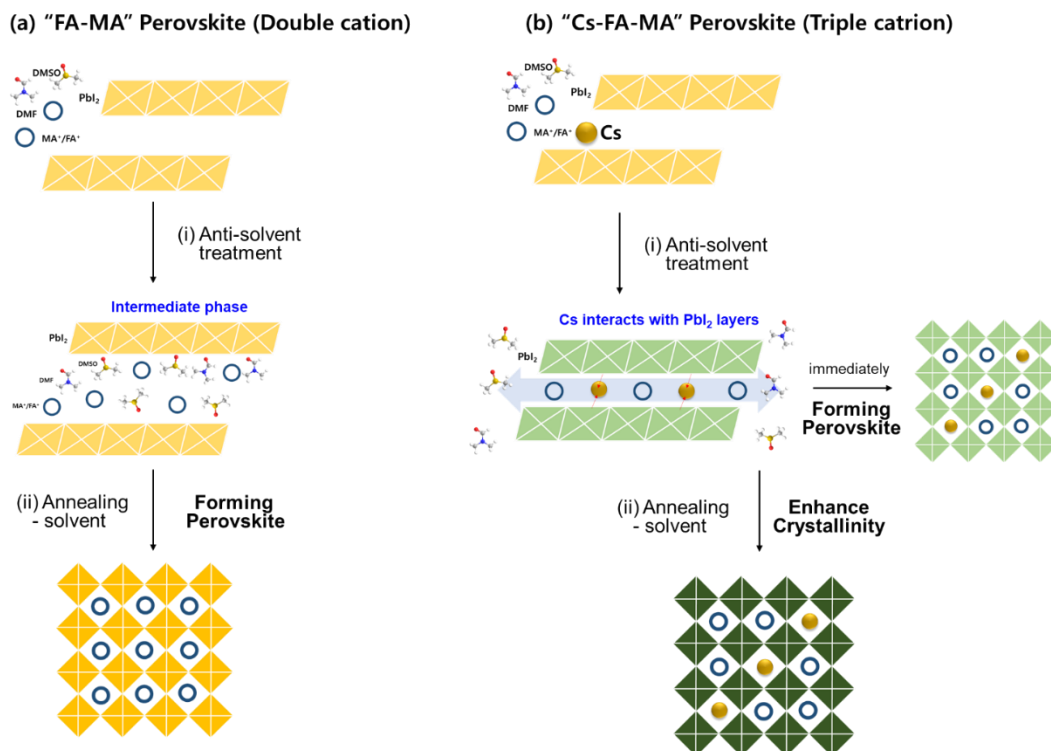
Figure 3.3. Illustration of different steps of the procedure for perovskite structure formation for either (a) FA/MA and (b)Cs/FA/MA perovskites by one step anti-solvet method.[29]

3.2.3 Photovoltaic Properties

Having elucidated the mechanism of perovskite formation in presence of Cs and MA ions, we proceeded to investigate the corresponding solar cell performance. We used a device structure consisting of fluorine doped tin oxide (FTO)/compact-TiO_2/Li-doped mesoporous-TiO_2/triple cation perovskite/spiro-OMeTAD/Au. For the first device optimization, we fabricated PSCs with various concentration of Cs in $FA_{0.8}MA_{0.2-x}Cs_x$. The corresponding current density-voltage (*J-V*) scans and incident photon-to-current efficiency (IPCE) are presented in Figure 3.4. As the Cs is added, the series of devices improves PV performance mainly in the current density reaching 21.5 mA/cm^2 at the optimum x = 10 % of Cs.
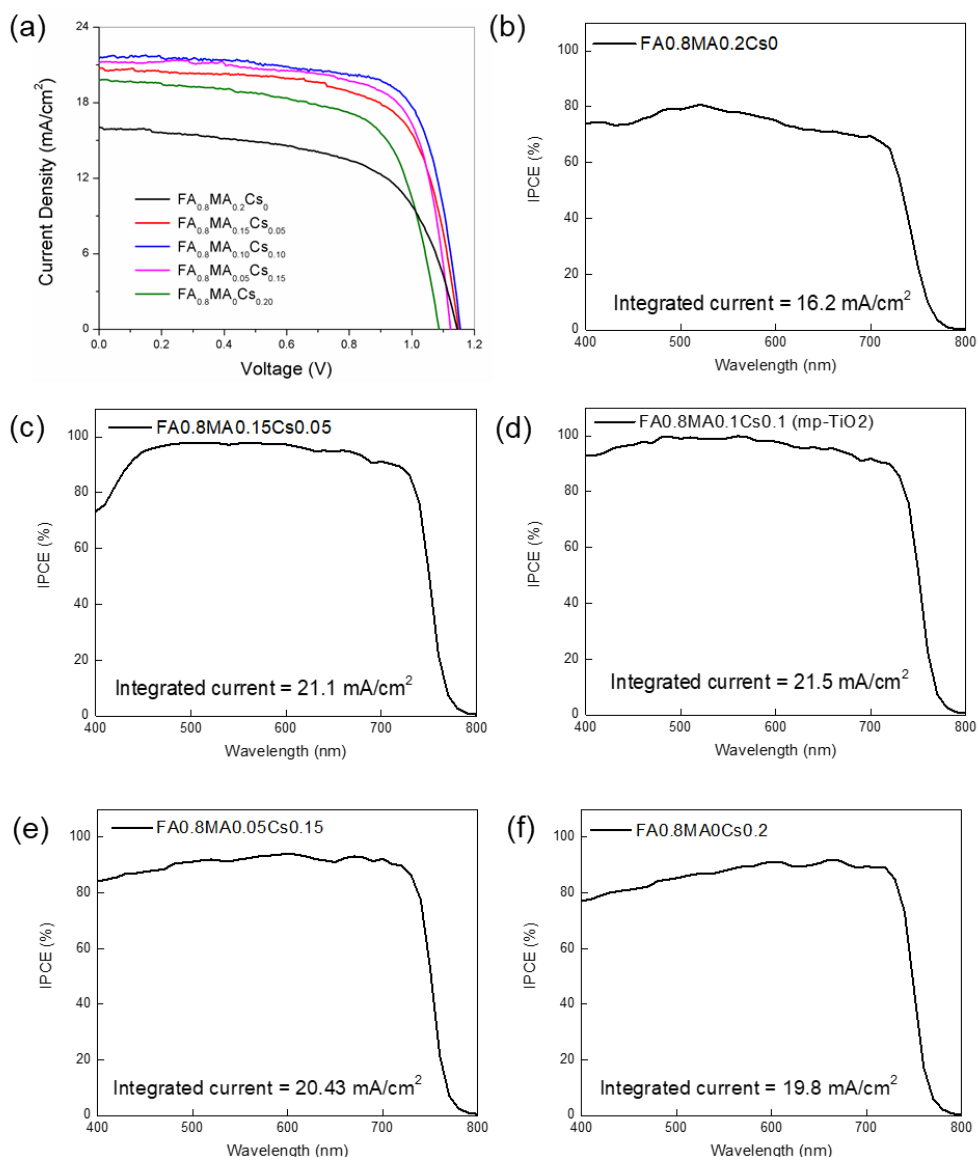
Figure 3.4. (a) *J-V* curves and (b-f) IPCE spectra of $FA_{0.8}MA_{0.2-x}Cs_x$ devices with varied x without annealing on mesoporous TiO_2. Devices were masked with an aperture of 0.1225 cm^2 to define the active area. *J-V* curves.

The dependence of the photovoltaic performance on the MA/Cs ratio with and without annealing (Figure 3.4b) reveals that mixtures of MA with Cs obtained the highest PCEs. This tendency was more pronounced for non-annealed devices, which is in accordance with the results from our XRD and SEM measurements. The cross-sectional SEM image of the device with 10% Cs without annealing shows a PCE of 18.0% (Figure 3.4a). Moreover, we note that the degree of hysteresis is not large and

does not correlate with either MA/Cs ratios or the annealing, as shown in Figure 3.4b. The current density-voltage (*J-V*) curves of the best RT device with the composition $FA_{0.8}MA_{0.1}Cs_{0.1}$ under standard AM 1.5G sunlight at 100 mW/cm^2 are shown in Figure 3c. The PCE derived from the *J-V* curve scanned in forward bias direction was 18.0% with an open-circuit voltage (V_{oc}) of 1088 mV, a short-circuit current density (J_{sc}) of 22.0 mA/cm^2, and a fill factor (FF) of 0.76. The power output was stabilized at 17.7% PCE, which is the highest PCE reported so far for a PSC prepared at room temperature. Importantly, there is only a 0.6% difference in PCE between non-annealed and annealed PSCs, which highlights the beneficial usage of cesium for low temperature manufacturing processes.
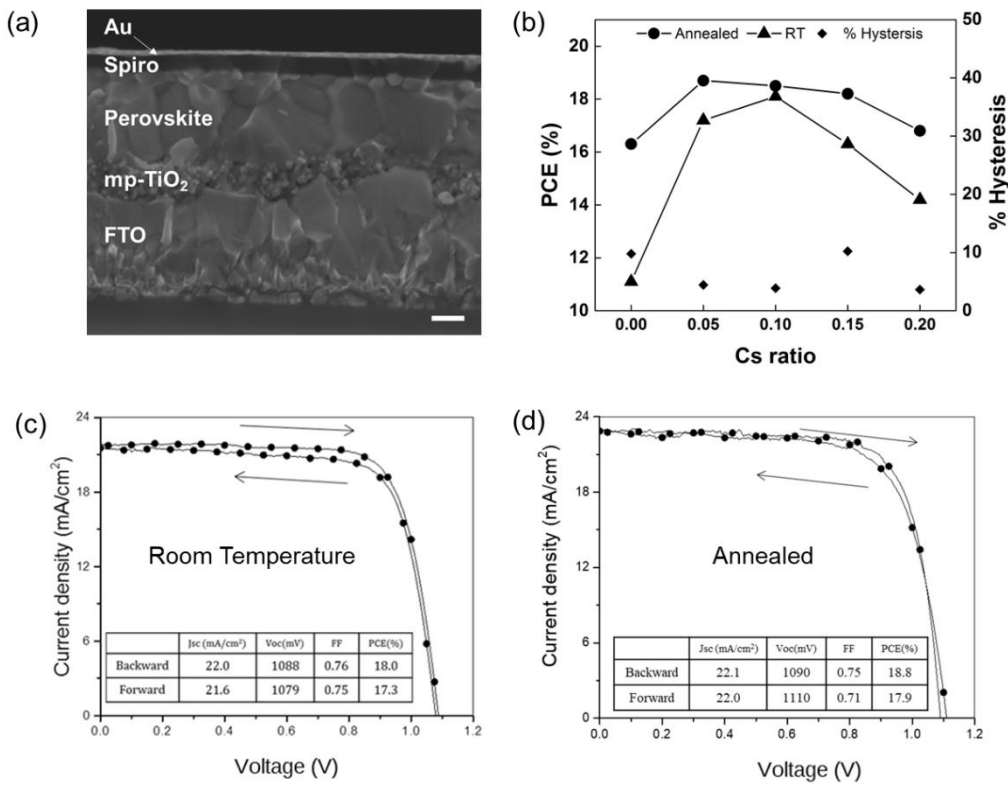

Figure 3.4 Top: (a) Cross sectional SEM image of the $FA_{0.8}MA_{0.1}Cs_{0.1}$ device without annealing. Scale bar is 200 nm. (b) Effect off the MA/Cs ratio on the PCE for annealed and un-annealed devices, along with the % hysteresis for un-annealed devices. % Hysteresis is determined by the equation 100×{PCE(reverse scan)-PCE(forward scan)}/ PCE(reverse scan). Bottom: *J-V* curves of the champion $FA_{0.8}MA_{0.1}Cs_{0.1}$ device (c) without annealing and (d) with annealing. *J-V* curves were measured from forward bias to short circuit condition and vice versa at the scan rate of 10 mV/s under AM1.5 simulated solar light (100 mW/cm^2). Devices were masked with an aperture of 0.1225 cm^2 to define the active area. Inset tables in Figure c) and d) present photovoltaic parameters extracted from the *J-V* curves.

In order to investigate its long-term shelf-life, we stored the device prepared at RT and the annealed device in the dark and under dry air conditions for 300 h (Figure 3.5). We detected no significant degradation under these conditions, as only 10% of PCE loss was observed for RT device and no loss for the annealed device after 300 h of storage.
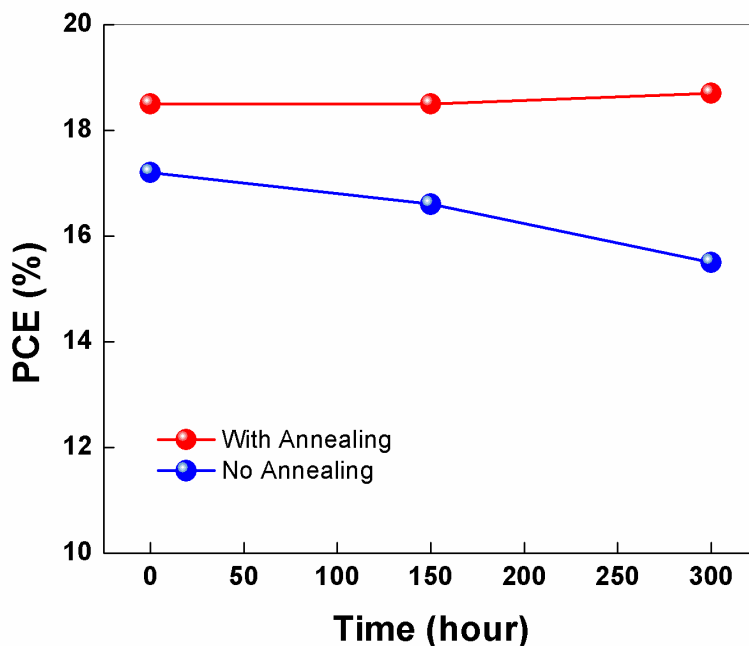
Figure 3.5. Long-term stability of annealed and non-annealed $FA_{0.8}MA_{0.1}Cs_{0.1}$ devices. Devices are stored in the dark and under dry air conditions.

Finally, in order to investigate the effect of Cs/MA ions on alternative solar cell architectures, we also prepared room temperature perovskite on planar substrate by employing SnO_2[30] as electron selective contact deposited by atomic layer deposition (ALD). The planar device achieved a PCE of 17.3% with a V_{oc} of 1129 mV, a J_{sc} of 22.4 mA/cm^2, and a *FF* of 0.68 derived from a forward scan, and a stabilized 17.0% PCE (Figure 3.6a). The current density was confirmed by the incident photon-to-current efficiency (IPCE), as shown in Figure 3.6b. This simple architecture employing $FTO/SnO_2/RT$-perovskite films is very attractive for large-scale manufacturing and preparation of flexible PSCs, facilitating future applications of Cs/MA perovskite solar cells.

(a)

(b)

	Jsc (mA/cm²)	Voc(mV)	FF	PCE(%)
Backward	22.8	1129	0.68	17.3
Forward	22.8	1132	0.60	15.1
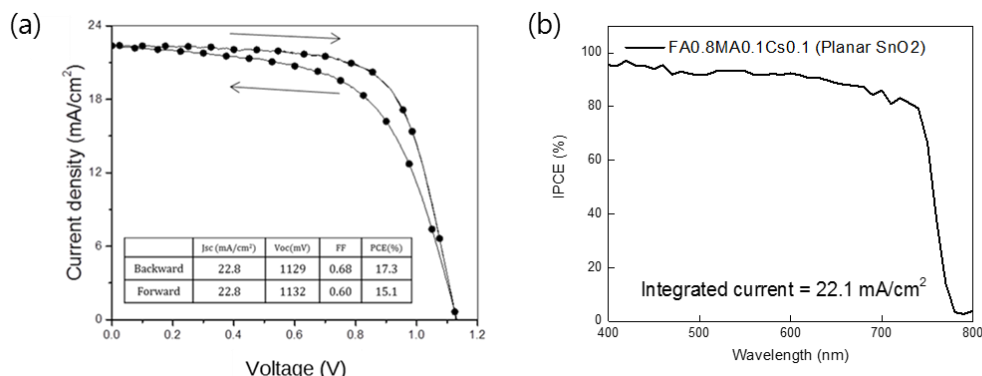
Figure 3.6. (a) *J-V* hysteresis and (b) Incident photon-to-current efficiency (IPCE) curve of $FA_{0.8}MA_{0.1}Cs_{0.1}$ device without annealing on planar SnO_2 substrates.

3.3   Conclusions

In conclusion, we examined the effect of Cs and MA in FA-based PSCs on the room temperature crystallization of mixed cation perovskites. The presence of both Cs and MA was necessary to obtain the photoactive crystalline perovskite phase and high-quality crystals. Remarkably, by using optimized cation mixture of $FA_{0.8}MA_{0.1}Cs_{0.1}$, we achieved a PCE of 18% without annealing or any post treatment, which was the record efficiency for perovskite solar cells under room temperature conditions. Moreover, the efficiencies of 17% were reproduced for planar perovskite solar cell architectures, which further highlights that this perovskite material shows great potential for low-cost, large-scale manufacturing procedures, such as the roll-to-roll process.

3.4   Experimental

Substrate preparation and Li-doping TiO_2. Nippon Sheet Glass 10 Ω/sq was cleaned by sonication in 2% Hellmanex water solution for 30 min. After rinsing with deionised water and ethanol, the substrates were further cleaned with UV ozone treatment for 15 min. Next, 30 nm TiO_2 compact layer was deposited on FTO via spray pyrolysis at 450 °C from a precursor solution of titanium diisopropoxide bis(acetylacetonate) in anhydrous ethanol. After spraying, the substrates were kept at 450 °C for 45 min and left to cool down to room temperature. The mesoporous TiO_2 layer was then deposited by spin-coating for 20 s at 4000 rpm with a ramp of 2000 rpm per second, using 30 nm particle paste (Dyesol 30 NR-D) diluted in ethanol to achieve a 150-200 nm thick layer. After the spin coating, the substrates were immediately dried at 100 °C for 10 min and then sintered again at 450 °C for 30 min un-

der dry air flow. Li-doping of mesoporous TiO_2 was accomplished by spin-coating a 0.1 M solution of Li-TFSI in acetonitrile at 3000 rpm for 30 s, followed by another sintering step at 450 °C for 30 minutes. After cooling down to 150 °C, the substrates were immediately transferred in a nitrogen atmosphere glove box for depositing the perovskite films.

Perovskite precursor solution and film preparation. The commercial precursors for organic cations were purchased from Dyesol; the lead compounds from TCI; and CsI from abcr GmbH. The perovskite precursor were dissolved in anhydrous DMF:DMSO 4:1 (v/v). The 10% excess of PbI_2 and $PbBr_2$ were used for perovskite precursor solution. The perovskite solution was spin-coated in a two steps program at 1000 and 4000 rpm for 10 and 20 s, respectively. During the second step, 200 μL of chlorobenzene was poured on the spinning substrate 15 s prior to the end of the program. The substrates were then annealed at 100 °C for 30 min in a nitrogen-filled glove box in case for the devices with the annealed perovskite.

Hole transporting layer and counter electrode. After the perovskite annealing, the substrates were cooled down for few minutes and a spiro-OMeTAD (Merck) solution (70 mM in chlorobenzene) was spin-coated at 4000 rpm for 20 s. Spiro-OMeTAD was doped with Li-TFSI(Sigma-Aldrich), FK209 (Dynamo) and tBP, (Sigma-Aldrich). The molar ratio of additives for spiro-OMeTAD was: 0.5, 0.03 and 3.3 for Li-TFSI, FK209 and TBP respectively. Finally, 70-80 nm of gold top electrode was thermally evaporated under high vacuum.

SnO_2 layer preparation. SnO_2 was deposited through atomic layer deposition (ALD) of TDMASn (99.99%-Sn, Strem Chemicals INC, heated at 55 °C) and ozone in a Savannah ALD 100 instrument (Cambridge Nanotech Inc.) at 118 °C. Oxygen gas (99.9995% pure, Carbagas) was used for production of ozone (13% in O_2) by a generator (AC-2025, IN USA Incorporated). The carrier gas was Nitrogen (99.9999% pure, Carbagas) with a flow rate of 10 sccm. The growth rate (0.065 nm/cycle) was measured by ellipsometry.

Photovoltaic device testing. The solar cells were measured using a 450 W Xenon light source (Oriel). The spectral mismatch between AM 1.5 G and the simulated illumination was reduced by the use of a Schott K113 Tempax filter (Präzisions Glas & Optik GmbH). The light intensity was calibrated with a Si photodiode equipped with an IR-cutoff filter (KG3, Schott), and it was recorded during each measurement. Current-voltage characteristics of the cells were obtained by applying an external voltage bias while measuring the current response with a digital source meter (Keithley 2400). The voltage scan rate was 10 mV/s and no device pre-conditioning,

such as light soaking or forward voltage bias applied for long time, was applied before starting the measurement. The starting voltage was determined as the potential at which the cells furnish 1 mA in forward bias, no equilibration time was used. The cells were masked with a black metal mask (0.1225 cm^2) to fix the active area and reduce the influence of the scattered light. The current was matched according to the intensity of the light source.

Perovskite characterization. A ZEISS Merlin HR-SEM was used to characterize the morphology of the device top view and cross-section. X-ray diffraction (XRD) were recorded on an X'Pert MPD PRO (Panalytical) equipped with a ceramic tube (Cu anode, λ = 1.54060 Å), a secondary graphite (002) monochromator and a RTMS X'Celerator (Panalytical) in an angle range of 2θ = 5° to 40° under ambient condition. Absorption spectral measurements were recorded using Varian Cary5 UV–visible spectrophotometer. Photoluminescence spectra were obtained with Florolog 322 (Horiba Jobin Ybon Ltd) with the range of wavelength from 620 to 850 nm by exciting at 460 nm. The samples were mounted at 60° and the emission recorded at 90° from the incident beam path. Thermogravimetric analyses (TGA) were carried out using a PerkinElmer TGA4000 with the perovskite powders that were gathered from perovskite films prepared by using the same method as the one for devices. The measurements were carried out under dry nitrogen at 20 mL/min by heating 5 °C/min. FT-IR spectrometer with attenuated total reflectance (ATR) collected by Digilab FTS 7000 spectral data for perovskite precursor in DMF/DMSO (4:1) as a liquid phase without dilution.

References

[1]   NREL chart, http://www.nrel.gov/ncpv/images/efficiency_chart.jpg

[2]   K. Masuko, M. Shigematsu, T. Hashiguchi, D. Fujishima, M. Kai, N. Yo-shimura, T. Yamaguchi, Y. Ichihashi, T. Mishima, N. Matsubara, T. Yamanishi, T. Takahama, M. Taguchi, E. Maruyama, S. Okamoto, *IEEE J. Photovolt.* **2014**, *4*, 1433.

[3]   A. Dualeh, N. Tetreault, T. Moehl, P. Gao, M. K. Nazeeruddin, M. Gratzel, *Adv. Funct. Mater.* **2014**, *24*, 3250.

[4]   N. J. Jeon, J. H. Noh, W. S. Yang, Y. C. Kim, S. Ryu, J. Seo, S. I. Seok, *Nature* **2015**, *517*, 476.

[5]   J.-W. Lee, D.-J. Seol, A.-N. Cho, N.-G. Park, *Adv. Mater.* **2014**, *26*, 4991.

[6]   J. Troughton, M. J. Carnie, M. L. Davies, C. Charbonneau, E. H. Jewell, D. A. Worsley, T. M. Watson, *J. Mater. Chem. A.* **2016**, *4*, 3471.

[7]   J. Troughton, C. Charbonneau, M. J. Carnie, M. L. Davies, D. A. Worsley, T. M. Watson, *J. Mater. Chem. A.* **2015**, *3*, 9123.

[8]   T. Jeon, H. M. Jin, S. H. Lee, J. M. Lee, H. I. Park, M. K. Kim, K. J. Lee, B. Shin, S. O. Kim, *ACS Nano* **2016**, *10*, 7907.

[9]   F. Li, W. Zhu, C. Bao, T. Yu, Y. Wang, X. Zhou, Z. Zou, *Chem. Commun.* **2016**, *52*, 5394.

[10]   G. Mincuzzi, A. L. Palma, A. Di Carlo, T. M. Brown, *ChemElectroChem* **2016**, *3*, 9.

[11]   J. W. Lee, D. H. Kim, H. S. Kim, S. W. Seo, S. M. Cho, N. G. Park, *Adv. Energy. Mater.* **2015**, *5*.

[12]   M. Saliba, T. Matsui, J.-Y. Seo, K. Domanski, J.-P. Correa-Baena, M. K. Nazeeruddin, S. M. Zakeeruddin, W. Tress, A. Abate, A. Hagfeldt, M. Gratzel, *Energ. Environ. Sci.* **2016**. 1989.

[13]   D. Liu, T. L. Kelly, *Nat. Photon.* **2014**, *8*, 133.

[14]   Y. Zhou, M. Yang, W. Wu, A. L. Vasiliev, K. Zhu, N. P. Padture, *J. Mater. Chem. A* **2015**, *3*, 8178.

[15] M. Yin, F. Xie, H. Chen, X. Yang, F. Ye, E. Bi, Y. Wu, M. Cai, L. Han, *J. Mater. Chem. A* **2016**, *4*, 8548.

[16] M. Saliba, S. Orlandi, T. Matsui, S. Aghazada, M. Cavazzini, J.-P. Correa-Baena, P. Gao, R. Scopelliti, E. Mosconi, K.-H. Dahmen, F. De Angelis, A. Abate, A. Hagfeldt, G. Pozzi, M. Graetzel, M. K. Nazeeruddin, *Nat. Energy* **2016**, *1*, 15017.

[17] D. Bi, W. Tress, M. I. Dar, P. Gao, J. Luo, C. Renevier, K. Schenk, A. Abate, F. Giordano, J.-P. Correa Baena, J.-D. Decoppet, S. M. Zakeeruddin, M. K. Nazeeruddin, M. Grätzel, A. Hagfeldt, *Sci. Adv.* **2016**, *2*, e1501170.

[18] Y. C. Kim, N. J. Jeon, J. H. Noh, W. S. Yang, J. Seo, J. S. Yun, A. Ho-Baillie, S. Huang, M. A. Green, J. Seidel, T. K. Ahn, S. I. Seok, *Adv. Energy. Mater.* **2016**, *6*, 1502104

[19] W. S. Yang, J. H. Noh, N. J. Jeon, Y. C. Kim, S. Ryu, J. Seo, S. I. Seok, *Science* **2015**, *348*, 1234.

[20] J. Pan, C. Mu, Q. Li, W. Li, D. Ma, D. Xu, *Adv. Mater.* **2016**, *28, 37*, 8309.

[21] S. Bae, S. J. Han, T. J. Shin, W. H. Jo, *J. Mater. Chem. A* **2015**, *3*, 23964.

[22] Y. G. Rong, Z. J. Tang, Y. F. Zhao, X. Zhong, S. Venkatesan, H. Graham, M. Patton, Y. Jing, A. M. Guloy, Y. Yao, *Nanoscale* **2015**, *7*, 10595.

[23] D. P. Nenon, J. A. Christians, L. M. Wheeler, J. L. Blackburn, E. M. Sanehira, B. J. Dou, M. L. Olsen, K. Zhu, J. J. Berrya, J. M. Luther, *Energ. Environ. Sci.* **2016**, *9*, 2072.

[24] N. Ahn, D.-Y. Son, I.-H. Jang, S. M. Kang, M. Choi, N.-G. Park, *J. Am. Chem. Soc.* **2015**, *137*, 8696.

[25] T. Glaser, C. Müller, M. Sendner, C. Krekeler, O. E. Semonin, T. D. Hull, O. Yaffe, J. S. Owen, W. Kowalsky, A. Pucci, R. Lovrinčić, *J. Phys. Chem. Lett.* **2015**, *6*, 2913.

[26] N. J. Jeon, J. H. Noh, Y. C. Kim, W. S. Yang, S. Ryu, S. I. Seok, *Nat. Mater.* **2014**, *13*, 897.

[27] D. Shen, X. Yu, X. Cai, M. Peng, Y. Ma, X. Su, L. Xiao, D. Zou, *J. Mater. Chem. A* **2014**, *2*, 20454.

[28]   X. Guo, C. McCleese, C. Kolodziej, A. C. S. Samia, Y. Zhao, C. Burda, *Dalton Trans.* **2016**, *45*, 3806.

[29]   P. Gratia, I. Zimmermann, P. Schouwink, J. H. Yum, J. N. Audinot, K. Sivula, T. Wirtz, M. K. Nazeeruddin, *ACS Energy Lett.* **2017**, *2*, 2686.

[30]   J. P. C. Baena, L. Steier, W. Tress, M. Saliba, S. Neutzner, T. Matsui, F. Giordano, T. J. Jacobsson, A. R. S. Kandada, S. M. Zakeeruddin, A. Petrozza, A. Abate, M. K. Nazeeruddin, M. Gratzel, A. Hagfeldt, *Energ. Environ. Sci.* **2015**, *8*, 2928.

Chapter 4.

Modification of Mesoporous TiO$_2$ as Electron Transport Materials

In this Chapter, we study for the first time 40 nm size TiO$_2$ particles being endowed with mesopores to augment the contact area with the perovskite from 60 m^2/g for the conventional scaffold to over 200 m^2/g. In addition, we passivate electronically the surface of the mesoporous TiO$_2$-beads (mp-TiO$_2$) by treatment with cesium halide (CsX, X = I or Br). We show that this ESL architecture leads to efficient PSCs by enhancement of the contact area and interface passivation between perovskite and mp-TiO$_2$ resulting in PCEs up to 21% with negligible hysteresis.

This Chapter is based on published work: Seo, J. Y. et al. Boosting the Efficiency of Perovskite Solar Cells with CsBr-Modified Mesoporous TiO$_2$ Beads as Electron-Selective Contact. *Adv. Funct. Mater.*, **2018**, 1705763

4.1   Introduction

There have been numerous studies on perovskite solar cells (PSCs) and solid state dye sensitized solar cells, focusing mainly on optimizing methods for film formation and compositional engineering to achieve high power conversion efficiency (PCE), as well as stability of perovskite solar cells (PSCs), culminating in a certified PCE of 22.7.[1–8]

Studies on electron-selective layers (ESLs) have also progressed, improving device performance. For example, Sargent et al. used chlorine-capped TiO$_2$ nanoparticles in their planar perovskite solar cells to enhance the device performance due to defect passivation of the interface between perovskite layer and the charge selective contact.[9] Other studies of TiO$_2$ modification with metal halides also showed stability and performance improvement of planar PSCs.[10-14] Nevertheless, today's most efficient devices still employ a mesoscopic TiO$_2$ scaffold as electron selective layer (ESL) despite significant progress on planar PSCs.[2],[9],[15–17]

Although the mesoporous TiO_2 scaffold is considered to be beneficial for PSCs as an electron transport material, there are only few studies of the effect of its architecture and surface modification on the PSC performance. Indeed, mesoscopic perovskite solar cells so far used 30 nm sized TiO_2 nanoparticles that constitute the mesoscopic scaffold acting as ESL, which lack any porosity, their surface being composed of smooth facets with mainly (101) and 001 orientations. By contrast, there have been several encouraging reports about introducing mesopores in the TiO_2 particles in the area of dye sensitized solar cells (DSSCs) where this resulted in improved device performance.[18,19] Another issue with TiO_2 is that electron trapping by coordinatively unsaturated Ti (IV) ions is likely to occur at its interface with the perovskite, which hampers charge transport and enhances radiationless charge carrier recombination, as well as the appearance of a hysteresis in the *J-V* curves.[20] Theoretical calculations for TiO_2 suggest that electrons prefer to localize just below the surface being trapped by oxygen vacancies and Ti (IV) ions.[21],[22] One of the most effective methods to reduce the trap states in the TiO_2 is surface or bulk doping, which has been widely investigated for mesoporous TiO_2 electrodes in dye-sensitized solar cells, and more recently in PSCs.[23-25] Some dopants reduce the charge recombination and increase electron transport by passivating oxygen defects in the TiO_2 lattice, and reducing trap states below the conduction band (CB) of TiO_2 in PSCs. Another effect of doping is the stabilization of power conversion efficiency and the suppression of hysteresis.[25-30]

Herein, we examine the effect of introducing nanopores in the TiO_2 particles that constitute the ESL scaffold on the photovoltaic performance and stability.

4.2   Results and Discussion

### 4.2.1   Geometry Effect of TiO_2 on Perovskite Solar Cell Perfromance

The morphology of the TiO_2 film was probed by comparing scanning electron microscopy images (SEM) for the conventional films constituted by nonporous particles produced from a commercial paste, 30NR-D (Dyesol) and with the new HPX-100 material (Cristal; Figure 4.1). The particle size of the latter is found to be larger than that of the standard, and the particles are endowed with pores of a few nanometer diameter. These mesoporous beads exhibit a high Brunauer Emmett and Teller (BET) surface area of 206.31 m^2/g, offering a larger contact area to the perovskite than the standard formulation (60 m^2/g).
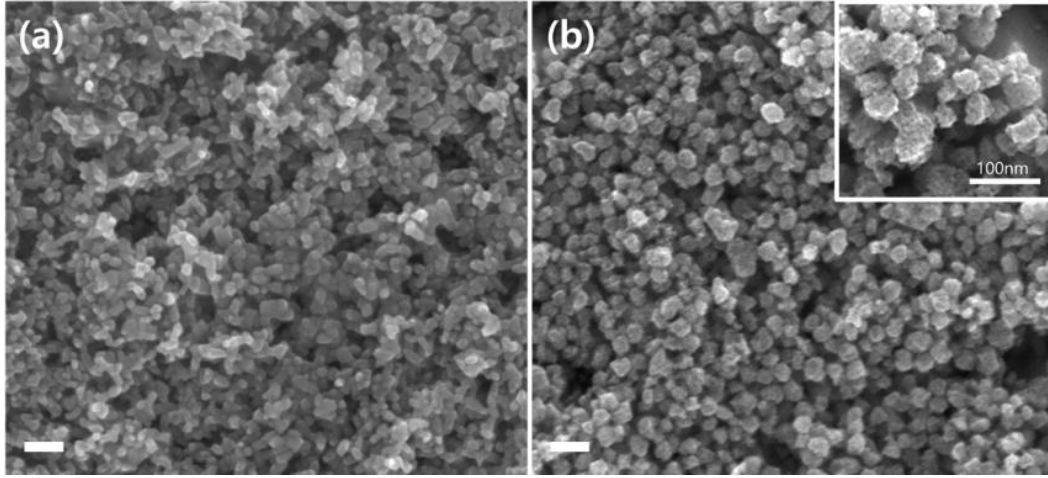
**Figure 4.1**. SEM images of the TiO₂ nano-particles. (a) 30NR-D and (b) HPX-100, respectively. Scale bar is 100 nm.

To investigate the effect of surface porosity of TiO₂ on device performance, we prepared PSCs with the same thickness of TiO₂ scaffold layer using non-porous (Figure 4.1a) and the mesoporous beads (Figure 4.1b), respectively. As shown in Figure 4.2, the photovoltaic parameters show an improved V_{OC} and *FF* for the mesoporous beads. Hence, the films made of the mesoporous beads were used in further studies.
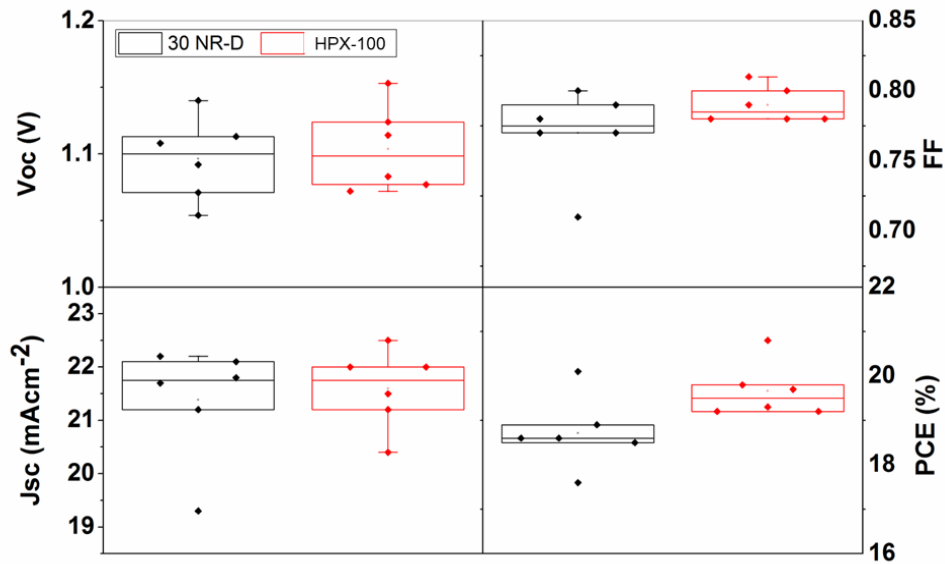
Figure 4.2. Statistics of Rb/Cs/FA$_{0.85}$/MA$_{0.15}$ perovskite device performance with nonporous nanocrystals of TiO₂ (anatase, 30 NR-D, Dyesol) and mesoporous nanocrystals of TiO₂ (anatase HPX-100, Cristal) as electron selective contact layers to the perovskite.

## 4.2.2 Effect of Cesium Modification on TiO$_2$

Cs-ion-doped mp-TiO$_2$ films were prepared by sintering CsX (X = I, Br) premixed TiO$_2$ paste for 30 min at 450 °C (as described in the Experimental Section). Transmission electron microscope (TEM) images of the mp-TiO$_2$ nanoparticles (NPs) with (CsI, CsBr) and without doping (Control) are shown in Figure 4.3. The TiO$_2$ nanocrystals are mesoporous with an average size of 40 nm (Figure 4.3a). After treatment with CsX, the morphology of the nanocrystals shows negligible difference compared to the untreated TiO$_2$ scaffold. The Cs ions are well dispersed in the TiO$_2$ structure, as confirmed by scanning transmission electron microscopy (STEM) coupled with energy-dispersive X-ray spectroscopy (EDX) elemental mapping measurements (Figure 4.3c,d), indicating successful and homogenous doping.
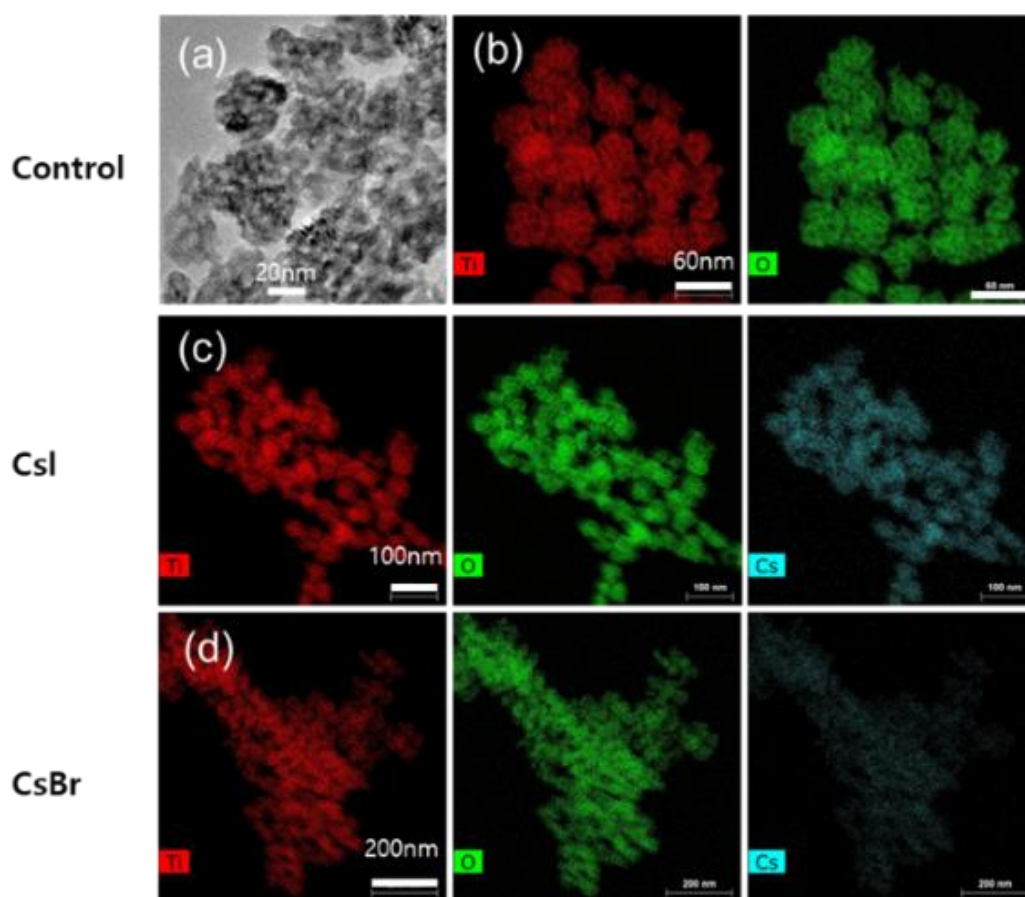
Figure 4.3. TEM and EDX elemental mapping characterizations of the mesoporous TiO$_2$ particles. (a) High-resolution TEM image and element mapping of (b) Ti and O for control and (c-d) element mapping of Ti, O and Cs for a CsI and CsBr doped TiO$_2$ particles, respectively.

X-ray photoemission spectroscopy (XPS) was performed to further investigate the elemental composition of the Cs doped and undoped TiO_2 (Figure 4.4; Table 4.1). In Figure 4.4a, we observed that the peak of Ti 2p slightly shifted to lower energy from 459.0 eV to 458.4 eV and 457.9 eV by doping with CsI and CsBr, respectively. We also observed that the O 1s peak shifted to lower energy as shown in Figure 4.4b. The full range of XPS spectra and atomic percentage ratio can be found in Figure 4.5c and Table 4.1. Cs more predominantly affected these shifts to lower energy than halides because the amount of halide on mp-TiO_2 is small compared to Cs. We rationalize this observation by Cs cation adsorption on the surface of TiO_2 *via* cation exchange against protons.
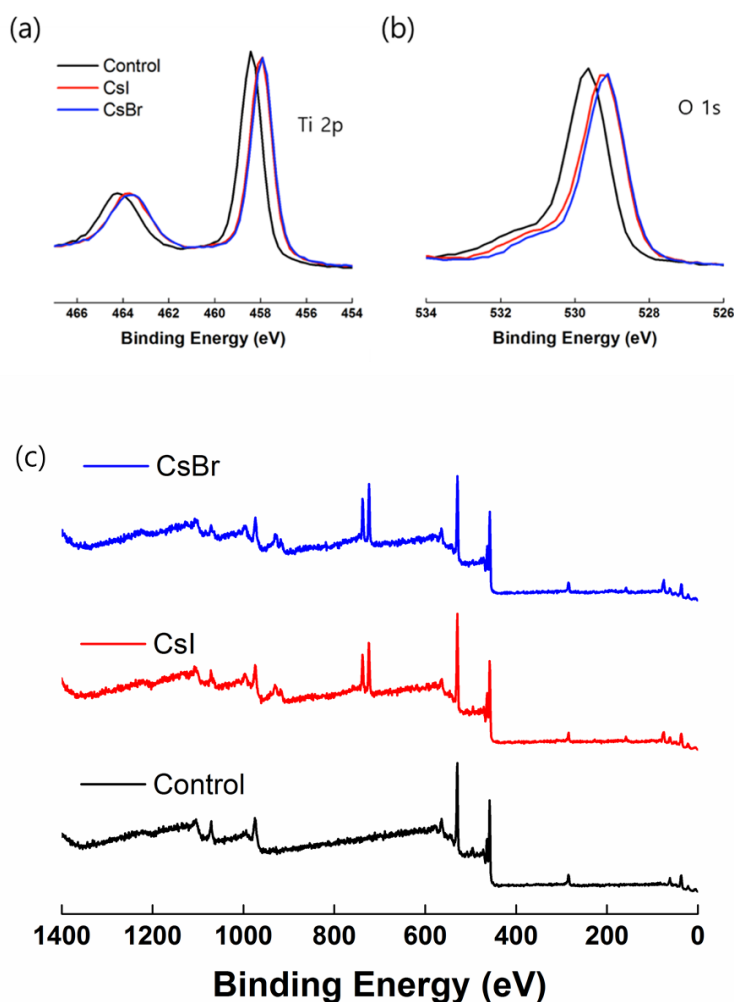

Figure 4.4. X-ray photoelectron spectroscopy spectra of mesoporous TiO_2 layers. (a) Ti 2p peaks and (b) O 1s peaks of non-doped sample (control, black), CsI doped sample (red) and CsBr doped sample (blue) respectively. (c) Full range of XPS spectra.

Table 4.1. Atomic percentage of C1s, O1s, Ti2p, Cs3d and X3d (X = I, Br) obtained from the XPS survey (Figure 4.4b)

Atomic %	**C1s**	**O1s**	**Ti2p**	**Cs3d**	**X3d**
Control	17.08	54.98	19.75	-	-
CsI	13.75	59.19	22.43	3.7	0.93
CsBr	17.45	53.94	20.61	3.32	0.26

The XPS peak shifts indicate that thermally introduced electron transfer from surface adsorbed halides to neighboring oxygen vacancies, and partial reduction of Ti^{4+} to Ti^{3+} within the TiO_2 lattice. This explains low level of halides found after thermal treatment by XPS analysis. This can passivate the electronic defects or trap states that originate from oxygen vacancies, resulting in improved charge transport properties.[27],[31–33]

To study the impact of Cs doping on the charge transport within the mp-TiO_2, we prepared dye-sensitized solar cells (DSSCs) using Cs doped mp-TiO_2 as electron transporting layer, as the charge extraction measurement method is well established to determine the density of state distribution below the TiO_2 conduction band.[34] In Figure 4.5, we report the extracted charge curves from the DSSCs at open circuit condition as a function of the open circuit voltage (V_{OC}). At the same V_{OC}, the devices prepared with Cs doped mp-TiO_2 exhibit significantly less charges than the control using mp-TiO_2 without doping, because of a lower density of trap state below the CB. This suggests that the Cs doping reduces oxygen vacancies of mp-TiO_2 by partial reduction of Ti^{4+} to Ti^{3+}, which helps to passivate the trapping states associated with oxygen vacancies within the TiO_2 lattice. These results show that CsBr is more efficient for doping mp-TiO_2 than CsI.
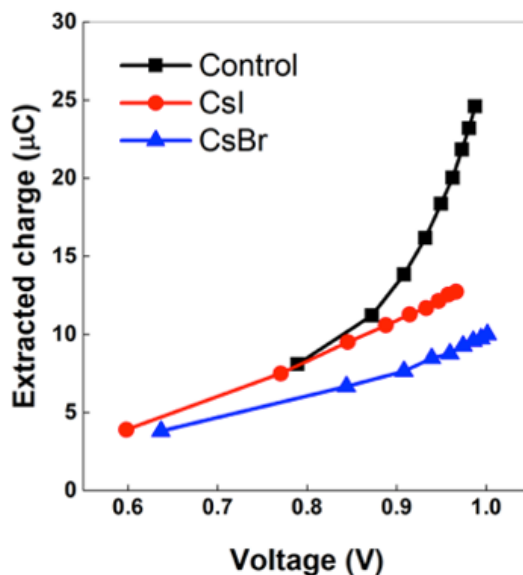
Figure 4.5. Charge extracted at open circuit as function of voltage for dye-sensitized solar cells prepared without and with Cs-doped mesoporous TiO$_2$.

4.2.3 Mophology and Optical Properties of the Perovskite

To further illustrate the effect of Cs doping on perovskite solar cells, we conducted characterization of perovskite films on the control and CsX doped TiO$_2$ films. Here, we used the quadruple-A catiton perovskite (Rb/Cs/FA$_{1-x}$/MA$_x$) for PSCs, which was developed in our previous study.[15] In order to investigate the impact of the Cs-doped mp-TiO$_2$ on the morphology and crystal structure of the perovskite film, we collected scanning electron microscopy (SEM) images and X-ray diffraction (XRD) patterns from perovskite films prepared on mp-TiO$_2$ substrates with and without CsX. In Figure 4.6a, the SEM images show all substrates form pinhole-free perovskite films of similar grain size. In Figure 4.6b, the XRD data shows that all substrates exhibit the same pattern with a strong typical perovskite peak at 14.2° corresponding to the (110) facet. Full width at half maximum (FWHM) of the (110) peak also shows almost no difference between the doped and undoped TiO$_2$.[35] Therefore, we conclude that CsX doping of the mp-TiO$_2$ does not influence the crystal growth or morphology of the perovskite films.
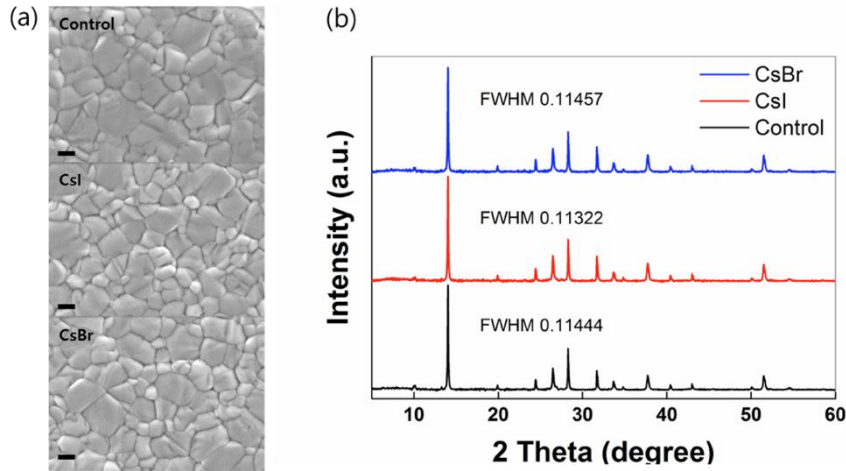
Figure 4.6. Morphological analysis of perovskite films with and without CsX (X = I and Br). (a) Top-view SEM images and (b)X-ray diffraction diagram (XRD) of perovskite films deposited on various mp-TiO$_2$/cp-TiO$_2$/FTO substrates annealed at 100°C for 1h. The intensity of XRD is normalized to the peak at 14° (110) and FWHM is calculated from (110) peak.

Steady-state and time-resolved PL spectroscopy were used to study the charge transfer kinetics between perovskite and different ESLs.[36] The steady-state PL was quenched more strongly when the perovskite films were formed on Cs-doped mp-TiO$_2$ (Figure 4.7a). PL decay curves of perovskite films on the control and Cs-doped mp-TiO$_2$ are shown in Figure 4.7b. The decay lifetime (τ) is shorter for films doped with CsI (79.30 ns) and CsBr (49.75 ns) than for the control (117.27 ns). The fitting parameters for PL decays are summarized in Table 4.2. These results indicate faster electron extraction at the CsX mp-TiO$_2$/perovskite interface compared to pristine TiO$_2$.
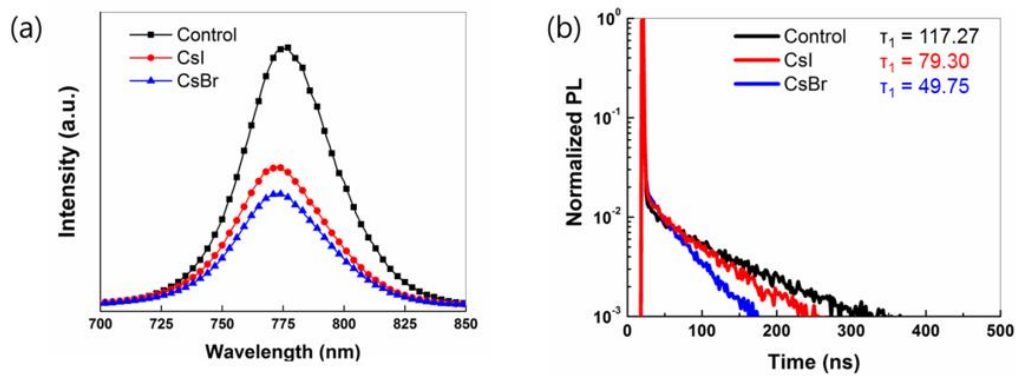
Figure 4.7. Photoluminescence characterization. (a) Steady-state photoluminescence (PL) emission spectra and (b) Normalized time-resolved photoluminescence (TRPL) decay plots of the perovskite films on various substrates with and without CsX doping (X=I and Br).

Table 4.2. Fitting parameters for the time-resolved PL measurements shown in Figure 4.7b. The PL decay can be fitted by a single exponential function: $y = y_0 + A_1 \exp(-(t-t_0)/\tau_1)$*.

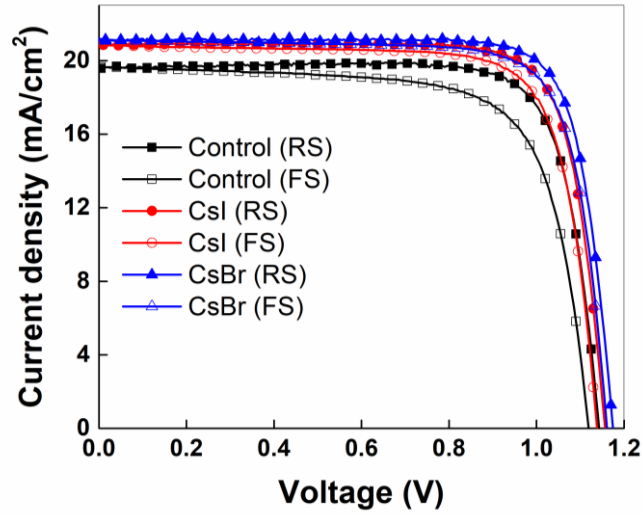|	Control	CsI	CsBr
y_0	3.78	3.42	2.48
t_0	33.17	29.00	27.79
A_1	480.21	617.26	740.36
τ_1	117.27	79.30	49.75

* y_0, t and A represent the time at the peak

4.2.4 Photovoltaic Properties upon CsX (X = I, Br) Treatment

To explore the effect of CsX loading of the mesoporous TiO$_2$ beads on the photovoltaic performance of PSCs, we prepared devices with the layered architecture of FTO/cp-TiO$_2$/mp-TiO$_2$/Perovskite/spiro-OMeTAD/Au. Figure 4.8 presents current density–voltage (*J-V*) curves for the Rb/Cs/FA$_{0.85}$ MA$_{0.15}$ perovskite devices with the pristine mp-TiO$_2$ (Control), CsI-doped mp-TiO$_2$ (CsI) and CsBr-doped mp-TiO$_2$ (CsBr) (with the parameters summarized in Table 4.3). Devices with Cs-doped mp-TiO$_2$ showed a higher open circuit voltage (V_{OC}), short circuit current (J_{SC}) and fill factor (FF) compared to the undoped reference. Moreover, hysteresis of devices was smaller using CsBr (4.5%) and CsI (5.2%) compared to the control (10.6%). The percentage of hysteresis is defined by following equation

$$100 \times \{PCE(\text{reverse scan}) - PCE(\text{forward scan})\}/PCE(\text{reverse scan}) \quad (4.1)$$

Statistics of device performance with Rb/Cs/FA$_{1-x}$MA$_x$ perovskite on various substrates convince that PSCs are more efficient with CsBr than CsI (Figure 4.9). The better performance of CsBr compared to CsI is explained by XPS study showing more extensive reduction of Ti^{4+} to Ti^{3+} (Figure 4.4). Concerning the function of halides, the small amount of residual halides (X = I and Br) on the mp-TiO$_2$ are used to form perovskite since both iodide and bromide are a constituents of Rb/Cs/FA$_{1-x}$MA$_x$ perovskite. The advantage of the bromide in the perovskite layer is that it enhances the crystal quality during the crystal growth, as shown in the previous study by Dar et al.[37] Additionally, as the Cs doping passivated surface traps and reduced recombination in ESLs, the devices produced enhanced performance in PCEs, with superior performance in case of treatment with CsBr.

Figure 4.8. Current density–voltage curves for the Rb/Cs/FA$_{0.85}$ MA$_{0.15}$ perovskite devices with the pristine mp-TiO$_2$ (Control), CsI-doped mp-TiO$_2$ (CsI) and CsBr-doped mp-TiO$_2$ (CsBr). The curves were measured from open circuit forward bias to short circuit condition (RS) and vice versa (FS) at the scan rate of 10 mV/s under AM1.5 simulated solar light. The device active area was defined using a black metal shadow mask with an aperture of 0.16 cm^2. The photovoltaic parameters of the devices were summarized in Table 4.3

Table 4.3. Photovoltaic parameters of best devices with and without CsX doping (X=I and Br): open-circuit voltage (V_{oc}), short circuit current (J_{sc}), fill factor (FF) as extracted from the *J-V* curves (PCE, reverse and forward scan) and of the devices in Figure 4.8.

	Scan direction	V_{oc} (V)	J_{sc} (mA/cm^2)	FF	Input Power (mW/cm^2)	PCE (%)
Control	Reverse	1.14	19.66	0.793	99.4	17.9
	Forward	1.12	19.64	0.722		16.0
CsI	Reverse	1.16	20.87	0.797	99.0	19.4
	Forward	1.14	20.86	0.772		18.4
CsBr	Reverse	1.18	21.07	0.811	99.3	20.2
	Forward	1.16	21.13	0.781		19.3
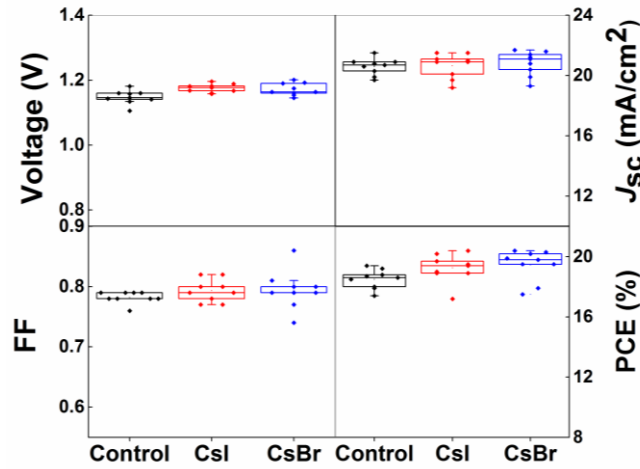
Figure 4.9. Statistics of Rb/Cs/FA$_{0.85}$ MA$_{0.15}$ perovskite device performance on cesium halide-doped and undoped (control) mp-TiO₂.

4.2.5 CsBr Treatment Compositional Engineering and Photovoltaic Properties

To identify the best perovskite composition for CsBr-doped mp-TiO₂, we conducted compositional engineering by tuning the ratio of MAPbBr₃ to FAPbI₃ from x = 0 to 0.15 (as shown in Figure 4.10). The average of V_{OC} and J_{SC} obtained from 15 devices with CsBr-treated mp-TiO₂ are plotted to reveal tradeoff between V_{OC} and J_{SC} (Figure 4.11). The best perovskite composition for CsBr doped mp-TiO₂ is achieved with x = 0.05, which is 10% less than our previous best composition on Li-treated mp-TiO₂.[15] This is due to the residual bromide on the mp-TiO₂ scaffold participating in formation of perovskite.
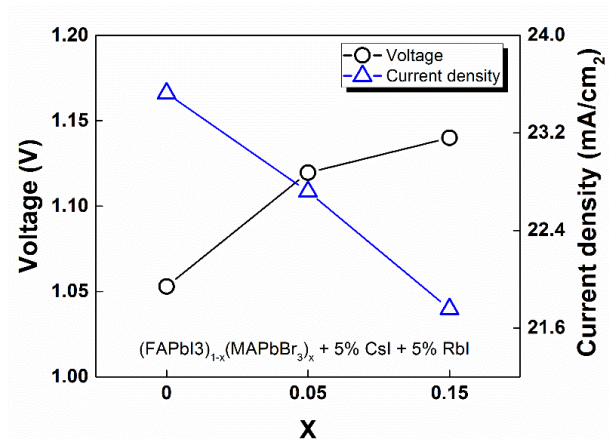

Figure 4.10. Photovoltaic performance of PSCs. (a) Compositional engineering to optimize the MAPbBr₃/FAPbI₃ ratio effect on the open circuit voltage and current density.

With optimized condition, we prepared devices with SEM images and *J-V* curves of the control and champion devices with the composition $Rb/Cs/FA_{0.95}MA_{0.05}$ under standard AM 1.5G sunlight at 98.5 mW/cm^2 shown in Figure 4.12. The average efficiency scanned in revers and forward bias direction was 21% with an open-circuit voltage (V_{OC}) of 1.14 V, a short-circuit current density (J_{SC}) of 23.2 mA/cm^2, and a fill factor (*FF*) of 0.78 with less than 4% hysteresis. The photovoltaic parameters are summarized in Table 4.4. The J_{SC} was confirmed by the integration of the incident photon-to-current efficiency (IPCE; Figure 4.13).
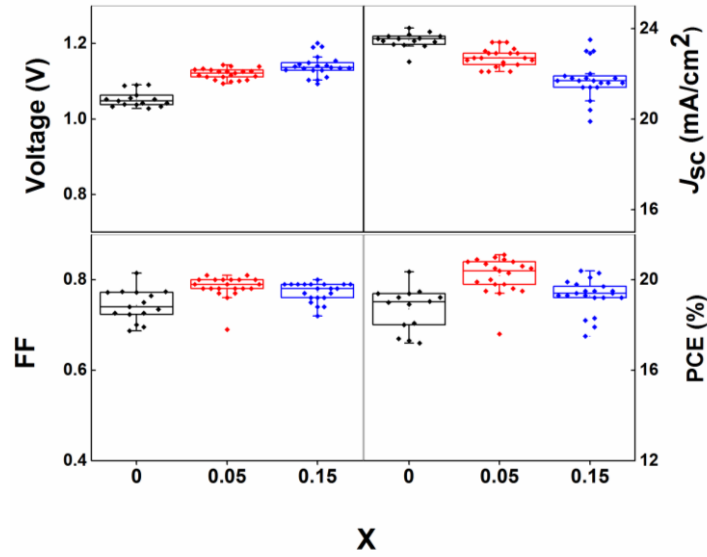
Figure 4.11. Statistics of $Rb/Cs/FA_{(1-x)}MA_x$ perovskite device performance on CsBr doped mp-TiO_2.
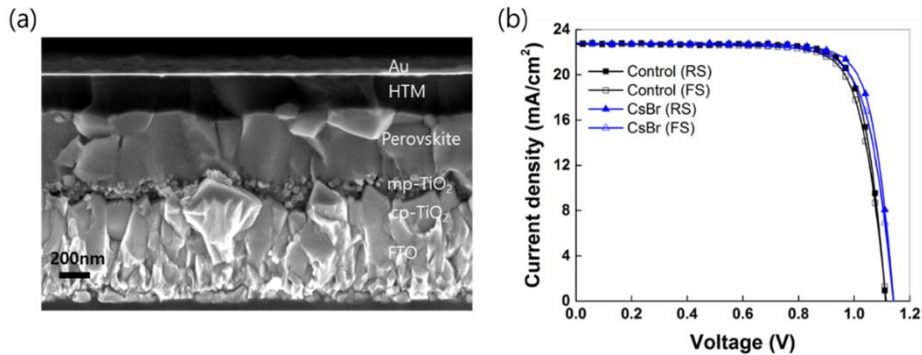
Figure 4.12. (a) Cross-sectional SEM images of champion device of CsBr-doped mp-TiO_2. (b) *J–V* curves for the perovskite devices with the pristine mp-TiO_2 and CsBr-doped mp-TiO_2 (CsBr). The curves were measured from open circuit to short circuit condition (RS) and vice versa (FS) at the scan rate of 10 mV/s under AM1.5 simulated solar light. The device active area was defined using a black shadow mask with an aperture of 0.16 cm^2. The photovoltaic parameters are summarized in Table 4.4.

Table 4.4. Photovoltaic parameters of best devices with CsBr-treated and pristine mp-TiO$_2$ (control): open-circuit voltage (*V$_{oc}$*), short circuit current (*J$_{sc}$*), fill factor (*FF*) as extracted from the *J-V* curves (PCE, reverse and forward scan) and of the devices in Figure 4.12b.

	Scan direction	V$_{oc}$ (V)	J$_{sc}$ (mA/cm^2)	FF	Input Power (mW/cm^2)	PCE (%)
Control	Reverse	1.11	22.7	0.798		20.4
	Forward	1.11	22.6	0.779	98.7	19.9
	Average	1.11	22.7	0.789		20.2
CsBr	Reverse	1.14	23.2	0.797		21.4
	Forward	1.14	23.1	0.771	98.5	20.6
	Average	1.14	23.2	0.784		21.0
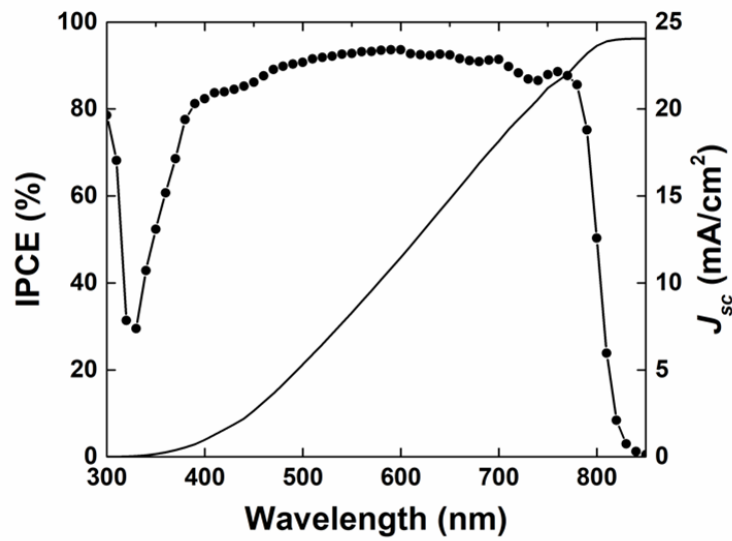
Figure 4.13. IPCE spectra of champion device on CsBr doped mp-TiO$_2$. Integrated current is 24.0 mA/cm^2.

In order to pinpoint the benefit of the CsBr treatment of TiO$_2$, we performed intensity-modulated voltage and photocurrent spectroscopy (IMVS and IMPS) measurements.[38] The results (Figure 4.15) were fitted to the reduced equivalent circuit model shown in Figure 4.14. The IMVS characterization confirmed the added benefit of

passivating the TiO$_2$ surface by cesium by slowing down recombination. This reduced recombination rate directly relates to the increased open circuit voltage observed. We also observed a higher series resistance and a higher charge transfer resistance for the cells treated with CsBr at the same voltage, which resulted in an unchanged collection efficiency around the maximum power point (Figure 4.15b). However, the result of collection efficiency can also be interpreted through CsBr-doped mp-TiO$_2$ involvement increasing the voltage of devices, because photocurrents show almost same value in Figure 4.12b of the devices with and without CsBr treatment in TiO$_2$.
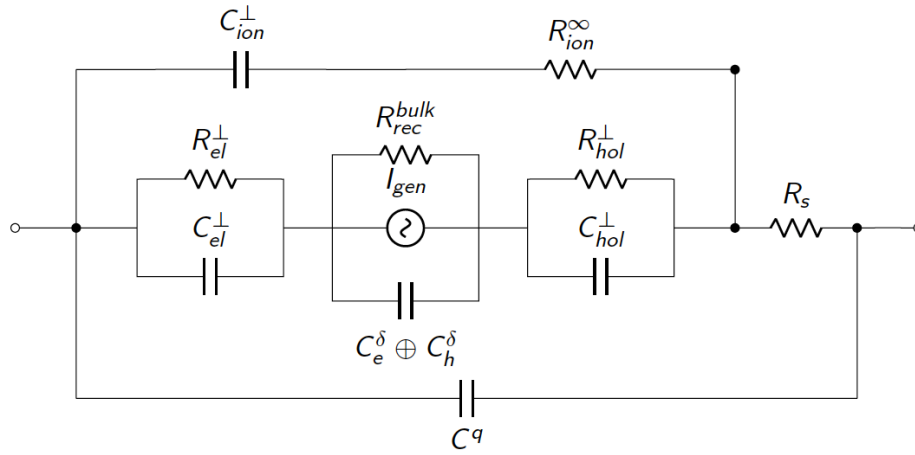
**Figure 4.14**. Diagram of the equivalent circuit diagram used to fit the IMPS and IMVS measurements.
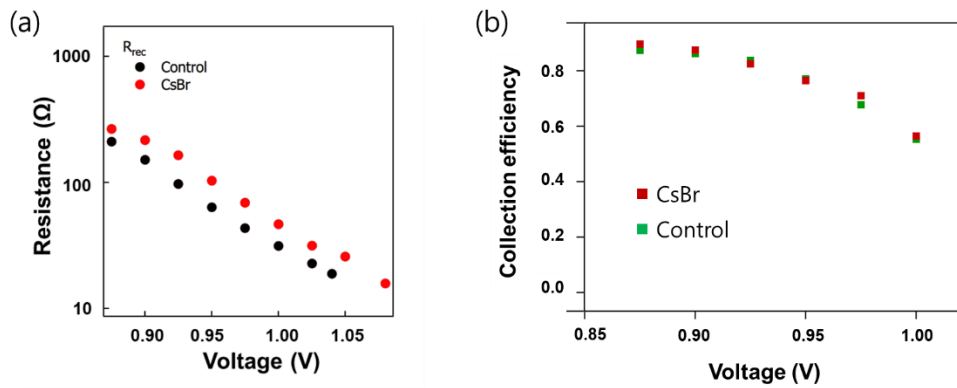
Figure 4.15. (a) IMVS and IMPS measurements. Recombination resistance (R$_{rec}$) of the control device (black circles) and the optimized device with CsBr doped mp-TiO$_2$ (red circles). (b) Collection efficiency of devices obtained from mesoporous TiO$_2$ beads with and without CsBr doping.

4.2.6 Stability

Finally, in order to investigate the long-term shelf-life of the devices, we stored the CsBr-doped and control mp-TiO$_2$ devices in the dark under dry air condition for one month (720 h). We observed high stability of CsBr devices, considering the relative value of loss being less than the control device under these conditions (Figure 4.16).
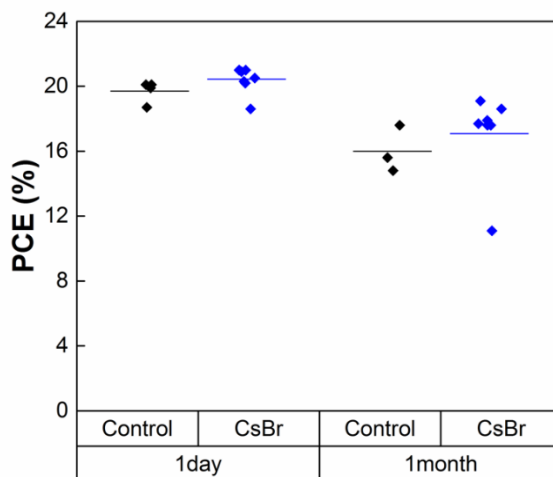
Figure 4.16. Long-term shelve life of the devices with and without CsBr doping of the mp-TiO$_2$ surface. Devices are stored in the dark under dry air condition.

4.3   Conclusions

We test for the first time 40 nm size TiO$_2$ particles being endowed with mesopores to augment the contact area with the perovskite from 60 m^2/g for the conventional scaffold to over 200 m^2/g. Additionally, we passivate electronically the surface of the mesoporous TiO$_2$-beads (mp-TiO$_2$) by treatment with cesium halide (CsX; X = I or Br). We show that this ESL architecture leads to efficient PSCs by enhancement of the contact area and interface passivation between the perovskite and the mp-TiO$_2$ layer. We demonstrate that Cs doping induces a shift of both oxygen (O) 1s and titanium (Ti) 2p peaks to lower energy, which implies decrease of oxygen vacancies that operates electron traps. As a result, PSCs based on Cs-doped mp-TiO$_2$ and quadruple-cation (Rb/Cs/FA/MA) perovskites exhibit enhanced electron transport and PCEs up to 21% with negligible hysteresis. These findings are of interest to further development of both perovskite and dye sensitized solar cell technologies in the future.

4.4   Experimental

Mesoporous TiO₂ paste. Mesoporous titania gel (washed CristalACTiV™ HPX-100™ prior to spray drying) was modified by treating with cesium iodide (HPX-100CsI) or cesium bromide (HPX-100CsBr) to obtain a 5% mole fraction of cesium halides on the titania, respectively. CristalACTiV™ HPX-100™ is available from Cristal and is a mesoporous titania nanoparticulate. The gel was then dried for 12 h at 105 °C. The dried powder was milled in a planetary mill in terpineol at a solids concentration of 20%. Untreated HPX-100™ was dried and milled using the same conditions.

Substrate preparation and Cs-doping TiO₂. Nippon Sheet Glass 10 Ω/sq was cleaned by sonication in 2% Hellmanex water solution for 30 min. After rinsing with deionised water and ethanol, the substrates were further cleaned with UV ozone treatment for 15 min. Then, 30 nm TiO₂ compact layer was deposited on FTO via spray pyrolysis at 450 °C from a precursor solution of titanium diisopropoxide bis(acetylacetonate) in anhydrous ethanol. After the spraying, the substrates were kept at 450 °C for 45 min and left to cool down to room temperature. TiO₂ pastes was used 30 NR-D (Dyesol) and HPX-100 (Cristal). 5 wt% of CsX (X= I and Br) premixed mp-TiO₂ paste was obtained from Cristal (HPX100CsI and HPX100CsBr Product code) for the mp-TiO₂ layer. mp-TiO₂ layer was deposited by spin coating for 20 s at 4000 rpm with a ramp of 2000 rpm per second to achieve a 150-200 nm thick layer. After the spin coating, the substrates were immediately dried at 100 °C for 10 min and then sintered again at 450 °C for 30 min under dry air flow. After cooling down to 150 °C, the substrates were immediately transferred in a nitrogen atmosphere glove box for depositing the perovskite films.

Perovskite precursor solution and film preparation. The organic cations were purchased from Dyesol; the lead compounds from TCI; CsI from abcr GmbH. The perovskite precursor were dissolved in anhydrous DMF/DMSO 4:1 (v/v). The 10% excess PbI₂ and PbBr₂ were used for perovskite precursor solution. The Rb/Cs/FA₁₋ₓMAₓ perovskite precursor solutions were deposited from a precursor solution containing FAI 1.2×(1-x) M, PbI₂ 1.3× (1-x) M, MABr 1.2×x M and PbBr₂ 1.3×x M in anhydrous DMF/DMSO 4:1 (v/v) (x = 0, 0.05, 0.15). Then CsI, predissolved as a 1.5 M stock solution in DMSO, was added to the mixed perovskite (FA/MA) precursor to make Cs/FA/MA triple cation perovskite. RbI was also predissolved as a 1.5 M stock solution in DMF/DMSO 4:1 (v/v) and then was added to the Cs/FA/MA triple cation perovskite to achieve the desired quadruple composition. The perovskite solution was spin-coated in a two steps program at 1000 and 4000 rpm for 10 and 20 s respectively. During the second step, 200 µL of chlorobenzene was poured

on the spinning substrate 15 s prior to the end of the program. The substrates were then annealed at 100 °C for 30 min in a nitrogen filled glove box.

Hole transporting layer and top electrode. After the perovskite annealing, the substrates were cooled down for few minutes and a spiro-OMeTAD (Merck) solution (70 mM in chlorobenzene) was spin-coated at 4000 rpm for 20 s. Spiro-OMeTAD was doped with Li-TFSI (Sigma-Aldrich), FK209 (Dynamo) and tBP (Sigma-Aldrich). The molar ratio of additives for spiro-OMeTAD was: 0.5, 0.03 and 3.3 for Li-TFSI, FK209 and TBP respectively. Finally, 70-80 nm of gold top electrode was thermally evaporated under high vacuum.

DSSC preparation procedure. In order to prepare the DSC devices, FTO substrates (NSG-10, Nippon Sheet Glass) were pre-treated with a detergent solution (Deconex) in ultrasonic bath and UV/O₃ (Model no.256-220, Jelight Company, Inc.), respectively. A TiO₂ underlayer is prepared by immersing the substrates in 40 mM TiCl₄ solution at 70 ℃ for 30 min. The pastes were screen-printed (≈ 3 μm) on the substrates prior to the sintering process. The Working electrodes were dipped for 16 h in 0.1 mM of Y123 dye solution (Dyenamo AB). For counter electrodes, FTO glass (TEC 6, Pilkington) were coated with PEDOT via electrodeposition[39],[40] 25 μm Surlyn spacer (Dupont) used for assembling the working electrode and counter electrodes and electrolyte encapsulation. The electrolytes prepared with 0.2 M Cu(I)tmby and 0.04 M Cu(II)tmby complexes, 0.1 M LiTFSI and 0.6 M tBP in acetonitrile. A detailed device preparation description can be found in the reported work of Saygili et al.[39]

Charge extraction techniques. Charge extraction and electron transport times in DSC devices as a function of open-circuit voltages were measured with the DYEN-AMO Toolbox System. The system mainly consists of a white LED light source (Seoul Semiconductors), a 16-bit resolution digital acquisition board (National Instruments) in order to record voltage traces and a current amplifier (Thorlabs PDA200C). For charge extraction, firstly, the DSCs were kept at open-circuit conditions and then they were illuminated by the light source. After 1 s the light was turned off and the device was switched to short-circuit condition. The total charge was obtained through the integration of current with respect to time. The complete charge-potential curve was obtained by using different light intensities.

Photovoltaic device testing. The solar cells were measured using a 450 W Xenon light source (Oriel). The spectral mismatch between AM1.5G and the simulated illumination was reduced by the use of a Schott K113 Tempax filter (Präzisions Glas & Optik GmbH). The light intensity was calibrated with a Si photodiode equipped with an IR-cutoff filter (KG3, Schott), and it was recorded during each measurement. Current-voltage characteristics of the cells were obtained by applying an external voltage bias while measuring the current response with a digital source meter (Keithley 2400). The voltage scan rate was 10 mV/s and no device preconditioning, such as light soaking or forward voltage bias applied for long time, was applied before starting the measurement. The starting voltage was determined as the potential at which the cells furnish 1 mA in forward bias, no equilibration time was used. The cells were masked with a black metal mask (0.16 cm^2) to fix the active area and reduce the influence of the scattered light. The current was matched according to the intensity of the light source. Incident photon to current efficiency (IPCE) spectra were recorded using the Ariadne system (Cicci Research). A non-reflective metallic mask with an aperture of 0.16 cm^2 was used during both measurements.

Perovskite characterization. A ZEISS Merlin HR-SEM was used to characterize the morphology of the device top view and cross-section. TiO$_2$ particles were characterized by a high-resolution transmission electron microscope (Technai Osiris, FEI). The composition of TiO$_2$ nanoparticles were characterized by the energy-dispersive X-ray (EDX) spectra obtained in scanning transmission electron microscopy (STEM) mode with Technai Osiris. X-Ray Photoelectron Spectroscopy (XPS) measurements were carried out using a PHI VersaProbe II scanning XPS microprobe (Physical Instruments AG, Germany). X-ray diffraction (XRD) were recorded on an Empyrean (Panalytical) equipped with a ceramic tube (Cu anode, $\lambda = 1.54060$ Å), Reflection-Transmission Spinner, a PIXcel^{1D} (Panalytical) in an angle range of $2\theta = 5°$ to $60°$ under ambient condition. Absorption spectral measurements were recorded using Varian Cary5 UV–visible spectrophotometer. Photoluminescence spectra were obtained with Florolog 322 (Horiba Jobin Ybon Ltd) with the range of wavelength from 620 to 850 nm by exciting at 460 nm. The samples were mounted at 60° and the emission recorded at 90° from the incident beam path. The time-resolved photoluminescence (TRPL) is incorporated into the same Fluorolog-312 spectrofluorometer. The exciting source is now a NANOLed 408 nm pulsed diode laser with a pulse width of less than 200 ps and repetition rate of 1 MHz.

The IMVS and IMPS measurements. IMVS and IMPS spectra were recorded as a function of voltage using a home-made instrumentation. The modulated light source consisted of Coherent OBIS 422 CW laser diode. The light beam was split into two

components (Thorlabs EBP1). The first component was directed into a 50-Ohm loaded biased silicon reference diode (Thorlabs DET10A). The second component was directed onto a beam diffuser (Thorlabs DG220) behind which the sample was placed (~2 cm away from the diffuser). A DC light bias was provided by additional blue LEDs, such that the total illumination intensity reached about 10 mW/cm^2. The device was connected to a home-made preamplifier that enforces galvanostatic or potentiostatic conditions and provide an amplified signal for the frequency response analyzer (FRA). The FRA (Metrohm Autolab FRA2) v-channel was connected to the analog remote of the laser diode, the x-channel was connected to the reference diode and the y-channel to the preamplifier. All measurements were recorded as a function of voltage and both IMPS and IMVS spectra were fitted together using a Levenberg-Marquart non-linear least square fitting algorithm (Igor Pro 6.3). For each iteration of the fitting loop, the solution of the model shown in Figure 4.14 was generated using an AC solver (SPICE), which input parameters were provided by the fitting loop. The collection efficiency was calculated based on the transport and recombination resistance, excluding the charge transfer resistance. We note that this interpretation remains valid even if interfacial recombination were the leading loss pathway.[38]

References

[1]   B. Li, L. Wang, B. Kang, P. Wang and Y. Qiu, *Sol. Energy Mater. Sol. Cells* **2006**, 90, 549.

[2]   D. Bi, W. Tress, M. I. Dar, P. Gao, J. Luo, C. Renevier, K. Schenk, A. Abate, F. Giordano, J.-P. Correa Baena, J.-D. Decoppet, S. M. Zakeeruddin, M. K. Nazeeruddin, M. Gra tzel and A. Hagfeldt, *Sci. Adv.* **2016**, *2*, 1501170.

[3]   N. J. Jeon, J. H. Noh, Y. C. Kim, W. S. Yang, S. Ryu and S. Il Seok, *Nat. Mater.* **2014**, *13*, 897.

[4]   M. M. T. Lee J Miyasaka, T Murakami, TN Snaith, HJ, *Science.* **2012**, *338*, 647.

[5]   A. Kojima, K. Teshima, Y. Shirai and T. Miyasaka, *J. Am. Chem. Soc.* **2009**, *131*, 6050.

[6]   N. J. Jeon, J. H. Noh, W. S. Yang, Y. C. Kim, S. Ryu, J. Seo and S. Il Seok, *Nature* **2015**, *517*, 476.

[7]   https://www.nrel.gov/pv/assets/images/efficiency-chart.png.

[8]   H.-S. Kim, C.-R. Lee, J.-H. Im, K.-B. Lee, T. Moehl, A. Marchioro, S.-J. Moon, R. Humphry-Baker, J.-H. Yum, J. E. Moser, M. Grätzel and N.-G. Park, *Sci. Rep.* **2012**, *2*, 591.

[9]   H. Tan, A. Jain, O. Voznyy, X. Lan, F. P. García de Arquer, J. Z. Fan, R. Quintero-Bermudez, M. Yuan, B. Zhang, Y. Zhao, F. Fan, P. Li, L. N. Quan, Y. Zhao, Z.-H. Lu, Z. Yang, S. Hoogland and E. H. Sargent, *Science.* **2017**, *355*, 722.

[10]   L. Qin, Z. Xie, L. Yao, Y. Yan, S. Pang, F. Wei and G. G. Qin, *Phys. Status Solidi - Rapid Res. Lett.* **2014**, *8*, 912.

[11]   H. Zhang, J. Shi, X. Xu, L. Zhu, Y. Luo, D. Li and Q. Meng, *J. Mater. Chem. A* **2016**, *4*, 15383.

[12]   D. Liu, S. Li, P. Zhang, Y. Wang, R. Zhang, H. Sarvari, F. Wang, J. Wu, Z. Wang and Z. D. Chen, *Nano Energy* **2017**, *31*, 462.

[13]   X. Zhang, Z. Bao, X. Tao, H. Sun, W. Chen and X. Zhou, *RSC Adv.* **2014**, *4*, 64001.

[14]   W. Li, J. Li, G. Niu and L. Wang, *J. Mater. Chem. A* **2016**, *4*, 11688.

[15] M. Saliba, T. Matsui, K. Domanski, J.-Y. Seo, A. Ummadisingu, S. M. Zakeeruddin, J.-P. Correa-Baena, W. R. Tress, A. Abate, A. Hagfeldt and M. Graetzel, *Science.* **2016**, *354*, 206.

[16] X. Li, D. Bi, C. Yi, J.-D. Décoppet, J. Luo, S. M. Zakeeruddin, A. Hagfeldt and M. Grätzel, *Science.* **2016**, *353*, 58.

[17] S. S. Shin, E. J. Yeom, W. S. Yang, S. Hur, M. G. Kim, J. Im, J. Seo, J. H. Noh, S. Il Seok, *Science.* **2017**, *356*, 167.

[18] A. Tricoli, A. S. Wallerand and M. Righettoni, *J. Mater. Chem.* **2012**, *22*, 14254.

[19] D. Chen, F. Huang, Y. B. Cheng and R. A. Caruso, *Adv. Mater.* **2009**, *21*, 2206.

[20] C. Di Valentin and A. Selloni, *J. Phys. Chem. Lett.* **2011**, *2*, 2223.

[21] Y. F. Ji, B. Wang and Y. Luo, *J. Phys. Chem. C* **2012**, *116*, 7863.

[22] N. A. Deskins, R. Rousseau and M. Dupuis, *J. Phys. Chem. C* **2009**, *113*, 14583.

[23] F. Giordano, A. Abate, J. Pablo, C. Baena, M. Saliba, T. Matsui, S. H. Im, S. M. Zakeeruddin, M. K. Nazeeruddin, A. Hagfeldt and M. Graetzel, *Nat. Commun.* **2016**, *7*, 10379.

[24] M. Kitahara, Y. Shimasaki, T. Matsuno, Y. Kuroda, A. Shimojima, H. Wada and K. Kuroda, *Chem. - A Eur. J.* **2015**, *21*, 13073.

[25] B. Roose, S. Pathak and U. Steiner, *Chem. Soc. Rev.* **2015**, *44*, 8326.

[26] H. Zhou, Q. Chen, G. Li, S. Luo, T. -b. Song, H.-S. Duan, Z. Hong, J. You, Y. Liu and Y. Yang, *Science.* **2014**, *345*, 542.

[27] U. B. Cappel, A. L. Smeigh, S. Plogmaker, E. M. J. Johansson, H. Rensmo, L. Hammarström, A. Hagfeldt and G. Boschloo, *J. Phys. Chem. C* **2011**, *115*, 4345.

[28] A. K. Chandiran, F. Sauvage, M. Casas-Cabanas, P. Comte, S. M. Zakeeruddin and M. Graetzel, *J. Phys. Chem. C* **2010**, *114*, 15849.

[29] F. Huang, Y. B. Cheng and R. A. Caruso, *Aust. J. Chem.* **2011**, *64*, 820.

[30] M. Wang, S. Bai, A. Chen, Y. Duan, Q. Liu, D. Li and Y. Lin, *Electrochim. Acta* **2012**, *77*, 54.

[31] M. A. Henderson, W. S. Epling, C. H. F. Peden and C. L. Perkins, *J. Phys. Chem. B* **2003**, *107*, 534.

[32] C. L. Olson, J. Nelson and M. S. Islam, *J. Phys. Chem. B* **2006**, *110*, 9995.

[33] A. Abate, T. Leijtens, S. Pathak, J. Teuscher, R. Avolio, M. E. Errico, J. Kirkpatrik, J. M. Ball, P. Docampo, I. McPherson and H. J. Snaith, *Phys. Chem. Chem. Phys.* **2013**, *15*, 2572.

[34] P. R. F. Barnes, K. Miettunen, X. Li, A. Y. Anderson, T. Bessho, M. Gratzel and B. C. O'Regan, *Adv. Mater.* **2013**, *25*, 1881–1922.

[35] J. Burschka, N. Pellet, S.-J. Moon, R. Humphry-Baker, P. Gao, M. K. Nazeeruddin and M. Grätzel, *Nature* **2013**, *499*, 316.

[36] Y. H. Lee, J. Luo, M. K. Son, P. Gao, K. T. Cho, J. Seo, S. M. Zakeeruddin, M. Grätzel and M. K. Nazeeruddin, *Adv. Mater.* **2016**, *28*, 3966.

[37] M. Ibrahim Dar, M. Abdi-Jalebi, N. Arora, T. Moehl, M. Grätzel, M. K. Nazeeruddin, *Adv. Mater.* **2015**, *27*, 7221.

[38] P. Norman, PhD Thesis No.7749 2017, Polytechnique Federale de Lausanne.

[39] H. Ellis, N. Vlachopoulos, L. Häggman, C. Perruchot, M. Jouini, G. Boschloo and A. Hagfeldt, *Electrochim. Acta* **2013**, *107*, 45.

[40] Y. Saygili, M. Söderberg, N. Pellet, F. Giordano, Y. Cao, A. B. Munoz-García, S. M. Zakeeruddin, N. Vlachopoulos, M. Pavone, G. Boschloo, L. Kavan, J. E. Moser, M. Grätzel, A. Hagfeldt and M. Freitag, *J. Am. Chem. Soc.* **2016**, *138*, 15087.

Chapter 5.

Molecular Dopant Zn(TFSI)$_2$ in spiro-MeOTAD as a Hole Transport Material

In this Chapter, we introduce a novel p-dopant for spiro-MeOTAD, namely Zn(TFSI)$_2$, which considerably enhanced both photovoltaic performance and long-term stability. Remarkably, the device employing Zn(TFSI)$_2$ demonstrated a high PCE of 22% and a superb photo-stability, showing even a 2% increase in PCE after 600 h at maximum power point (mpp) under full sun, while the PCE of the device with conventional p-dopant, Li-TFSI, decreased by 20% under the same measurement condition.

5.1 Introduction

The normal perovskite solar cell structure (n-i-p) was intially introduced in 2012, as the device architecture comprising compact (cp) and mesoporous (mp) TiO$_2$ as an electron transport material (ETM) and 2,2',7,7'-tetrakis[*N*,*N*-di(4-methoxyphenyl)amino]-9,9'-spirobifluorene (spiro-MeOTAD) as a hole transport material (HTM ; Figure 5.1a).[1] This remains the most representative structure of the perovskite solar cells for persistently achiving the record highest efficiencies. However, the poor device stability of the normal structure, mainly due to low hole mobility of spiro-MeOTAD that requires employing lithium bis(trifluoromethylsulfonyl)imide (Li-TFSI) as a dopant (Figure 5.1b), raised doubts about the long-term operational stability of the PSC..[10-12] Various dopants were studied with the aim of replacing the conventional Li-TFSI and improving the stability, such as Ag-TFSI,[13] Co(III) complexes,[14] and CuI.[15] These were nonetheless still unable to compete against the performance of Li-TFSI, and are thus often applied in addition to Li-TFSI for achieving higher efficiency.[13,15]

Alternatively, a dicationic salt of spiro-MeOTAD, spiro(TFSI)$_2$, was used as a replacement for Li-TFSI to increase the conductivity of spiro-MeOTAD, reaching a PCE of around 10%.[16] Similarly, molybdenum tris(dithiolene)s successfully replaced Li-TFSI and showed the efficiency of 16.7%, with particularly improved thermal stability.[17] The discovery of a new dopant for the spiro-MeOTAD therefore remains appealing, particularly in conjunction with the well-established normal device structure.

Towards this goal, the TFSI couterion is an attractive candidate, considering its remarkable stability, hydrophobicity and conductivity owing to well delocalized charge on the overall TFSI anion. [18,19] Moreover, the trifluoromethylsulphonyl (CF$_3$SO$_2$-) group acts as a particularly strong electron-withdrawing group, which is thus able to effectively distribute the negative charge away from the nitrogen atom, leading to weaker basicity and, consequently, lower chemical reactivity.[18,19]

In this study, a new dopant, Zn(TFSI)$_2$ (Figure 5.1c), was proposed to overcome the stability issues without compromising the efficiency of the conventional device. The beneficial effect of Zn(TFSI)$_2$ on photovoltaic performance was investigated in comparison with Li-TFSI, and the origin of long-term stability was elucidated by decoupling the photo- and thermal-stability at maximum power point.

5.2   Results and Discussion

5.2.1   Structure of the Dopant

The molecular structure of Li-TFSI, the conventional dopant for spiro-MeOTAD, differs from Zn(TFSI)$_2$, a dopant employed in this study (Figure 5.1), in such a way that ensures lower diffusion rates of the latter. This was assumed to play an important role in suppressing the critical instability of the perovskite solar cells arising from the Li -ion migration to the adjacent layers.[34] Moreover, Li-TFSI was found to act as a dopant for spiro-MeOTAD in ambient air by the aid of oxygen, leading to the oxidized spiro-MeOTAD coupled with the reduction of oxygen to peroxide or superoxide that is stabilized by forming lithium-oxygen complexes.[20]
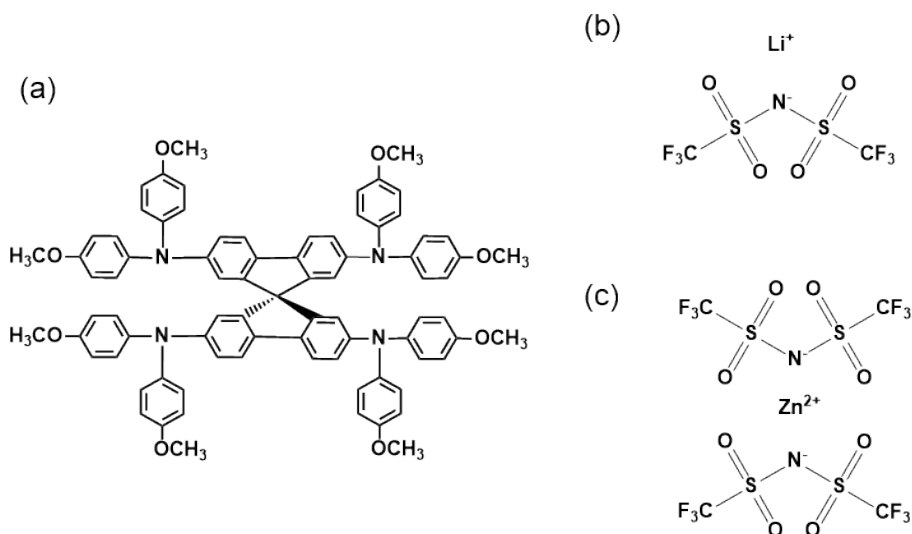
Figure 5.1. Molecular structure of dopants (a) spiro-MeOTAD, (b) Li-TFSI and (c) Zn(TFSI)$_2$.

5.2.1 Dopant Effect on the Hole Mobility of spiro-MeOTAD

The hole mobility of spiro-MeOTAD was measured to clarify the effect of dopant by space charge limited current (SCLC) with the solution-processed thin film (Figure 4.2). The concentration of Zn(TFSI)$_2$ was set to half of Li-TFSI for a rational comparison in this study due to the charge difference of the two dopants. The composition of HTM for the hole mobility measurements was equal to the one for photovoltaic devices where the spiro-MeOTAD employed cobalt complex (tris[2-((1H-pyrazol-1-yl)-4-tert-butylpyridine)cobalt(III)tris(bis(trifluoromethylsulfonyl)imide)], FK209), 4-tert-butylpyridine (tBP), and either Zn(TFSI)$_2$ or Li-TFSI (for details refer to the Experimental Section). The obtained results are shown in Table 5.1. The pristine spiro-MeOTAD without any additive showed a hole mobility of $2.69 \cdot 10^{-5}$ cm^2 V^{-1}s^{-1}, which increased to $3.78 \cdot 10^{-3}$ cm^2 V^{-1}s^{-1} by adding Li-TFSI and tBP. When Li-TFSI was replaced by Zn(TFSI)$_2$, the hole mobility of the spiro-MeOTAD solution was enhanced more than two times to $3.83 \cdot 10^{-2}$ cm^2 V^{-1}s^{-1}. These results indicate a beneficial effect of Zn(TFSI)$_2$ on the hole mobility of the HTM layer.
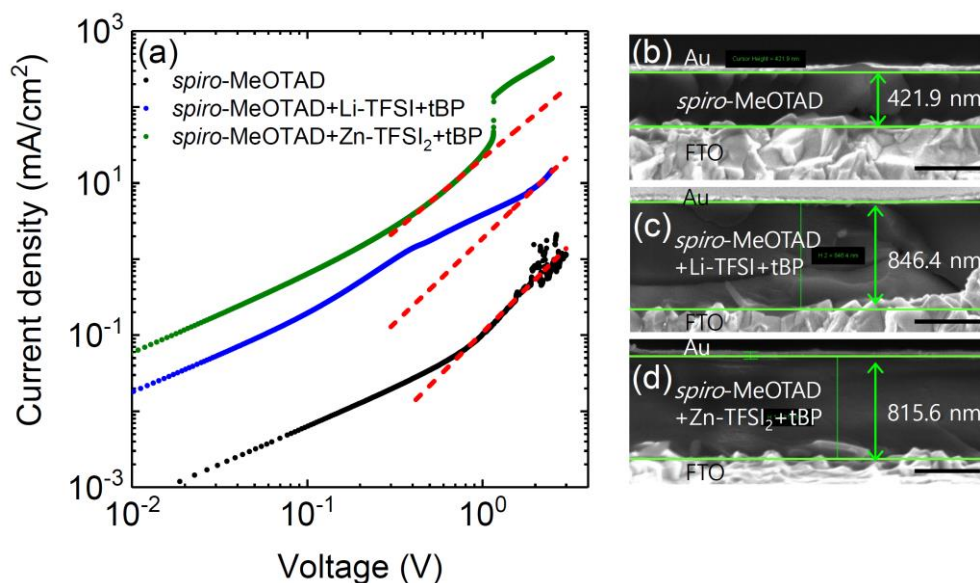
Figure 5.2 (a) Current (J)-voltage (V) plot of hole only devices. Cross-sectional SEM images of the hole only devices employing (b) spiro-MeOTAD, (c) spiro-MeOTAD with Li-TFSI and tBP, and (d) spiro-MeOTAD with Zn-TFSI2 and tBP. Scale bars in (b)-(d) represent 500 nm.

Table 5.1 Hole mobility of spiro-MeOTAD depending on the dopants.

Composition of hole transport material (HTM)	Hole mobility ($cm^2 V^{-1} s^{-1}$)
Pristine spiro-MeOTAD	$2.69 \cdot 10^{-5}$
spiro-MeOTAD+Li-TFSI +tBP	$3.78 \cdot 10^{-3}$
spiro-MeOTAD+Zn(TFSI)$_2$+tBP	$3.83 \cdot 10^{-2}$

The architecture of the devices and the morphology of the corresponding films were analyzed by the cross-section scanning electron microscopy (SEM) measurements (Figure 5.2b).

In order to examine the hole capture at the interface with spiro-MeOTAD, photoluminescence (PL) spectra of the perovskite films were measured. Perovskite films used in this study were composed of mixed triple cations (formamidinium, me-

thylammonium and cesium) and double halides (iodide and bromide) in $Cs_{0.05}(FA_{0.85}MA_{0.15})_{(100-x)}Pb(I_{0.85}Br_{0.10})_3$ composition to assure a high quality of the perovskite film coupled with a stable phase.[21] The perovskite film shows a clear PL peak at 760 nm (gray line) corresponding to the radiative recombination between photogenerated electron and hole at the respective band edge (Figure 5.3). The strong PL intensity of perovskite was substantially diminished by attaching the spiro-MeOTAD layer, leading to a hole injection from the perovskite to the HTM. A larger PL quenching was observed from the spiro-MeOTAD with Zn(TFSI)₂ compared to the one with Li-TFSI, indicating that the spiro-MeOTAD doped by Zn(TFSI)₂ facilitated more efficient hole separation at the interface with the perovskite. In summary, the replacement of Li-TFSI by Zn(TFSI)₂ was found to effectively improve both hole separation and mobility. Therefore, the incorporation of Zn(TFSI)₂ as a dopant for spiro-MeOTAD was highly encouraging in terms of beneficial hole extraction in the photovoltaic device, which was further probed through the investigation of the photovoltaic and electronic properties of the corresponding devices.
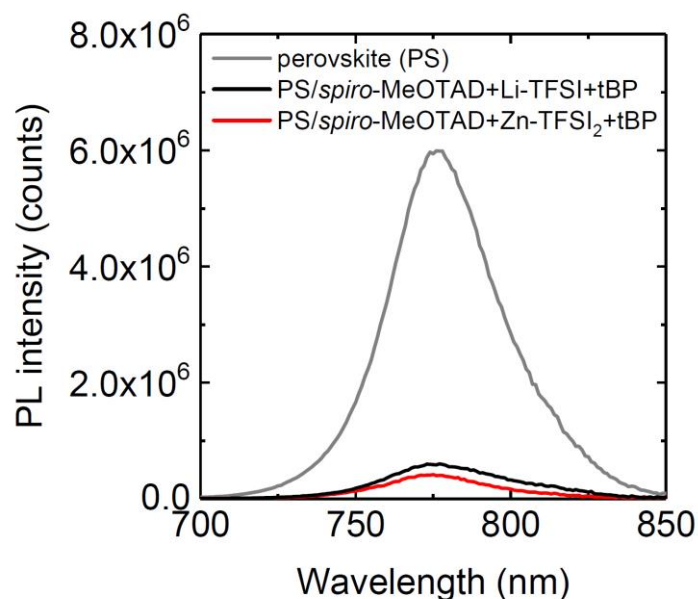
Figure 5.3 Photoluminescence (PL) curves of perovskite film (gray), perovskite/spiro-MeOTAD film with Li-TFSI and tBP (black) and perovskite/spiro-MeOTAD film with Zn-TFSI2 and tBP(red) on a glass substrate. Excitation with 450 nm light was from the film side.

5.2.2 Photovoltaic Performance

Devices were prepared to investigate the effect of $Zn(TFSI)_2$ on the overall photovoltaic performance based on the normal structure where cp-TiO$_2$ and mp-TiO$_2$ were incorporated as an ETM, and spiro-MeOTAD containing either of dopants (Li-TFSI or $Zn(TFSI)_2$), and tBP was employed as a HTM. Cross-sectional images of the devices allowed for the estimation of the thickness of spiro-MeOTAD layers to about ca. 200 nm independent of the dopant.
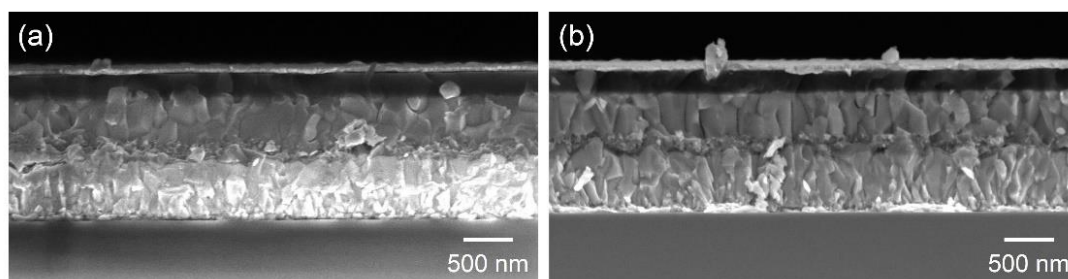
Figure 5.4 Cross-sectional scanning electron microscope (SEM) images of devices employing (a) Li-TFSI and (b) $Zn(TFSI)_2$ as dopants for spiro-MeOTAD.

The current-voltage (*IV*) curves of the devices depending on the dopant were recorded (Figure 5.5a) and the numerical values of the corresponding photovoltaic parameters are represented in Table 5.2. The device with $Zn(TFSI)_2$ demonstrated higher power conversion efficiency (PCE) of 21.06% at the reverse scan (RS) and 20.47% at the forward scan (FS). This was significantly higher compared to the devices with Li-TFSI, showing 19.38% at RS and 17.75% at FS. An obvious increase was observed in both open-circuit voltage (V_{OC}) and fill factor (FF) of the device with $Zn(TFSI)_2$ while its short-circuit photocurrent density (J_{SC}) was comparable to the one with Li-TFSI. It was also notable that the replacement of Li-TFSI with $Zn(TFSI)_2$ reduced the *I-V* hysteresis. The overall high incident photon-to-current efficiency (IPCE) was shown to be above 80% (Figure 5.5b), irrespective of the dopant, for the whole visible wavelengths, with a steep breakdown around 760 nm, corresponding to the bandgap of perovskite. The integrated J_{SC} calculated from the IPCE matches well with the measured value. The summary of the photovoltaic parameters for a series of devices as a function of the dopant can be found in Figure 5.6, showing that the average PCEs for Li-TFSI and $Zn(TFSI)_2$ were 18.08% and 19.60%, respectively.
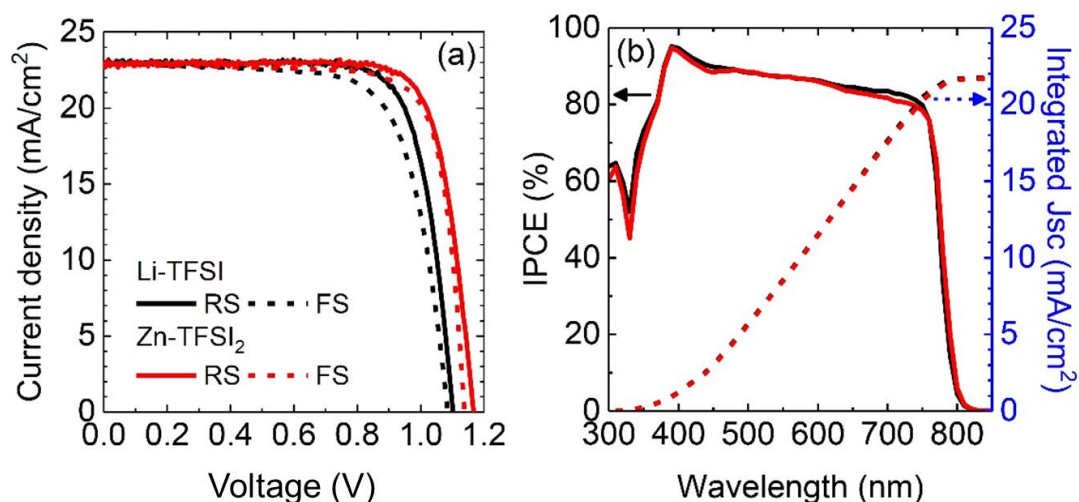
Figure 5.5 (a) Current-voltage (*IV*) curves and (b) incident photon-to-current efficiency (IPCE) spectra of devices employing Li-TFSI and Zn(TFSI)₂ as a dopant for spiro-MeOTAD. Reverse scan (RS) indicates the scan direction from the open-circuit to the short-circuit condition. Forward scan (FS) is the opposite way from the short-circuit to open-circuit condition.

Table 5.2 Photovoltaic parameters of the devices employing Li-TFSI and Zn(TFSI)₂ as a dopant for spiro-MeOTAD. RS = reverse scan, FS = forward scan.

| Dopant	Scan direction	Jsc (mA/cm^2)	Voc (V)	FF	PCE (%)
Li-TFSI	RS	22.9	1.102	0.768	19.38
	FS	22.9	1.086	0.714	17.75
Zn(TFSI)₂	RS	22.6	1.168	0.798	21.06
	FS	23.0	1.138	0.783	20.47
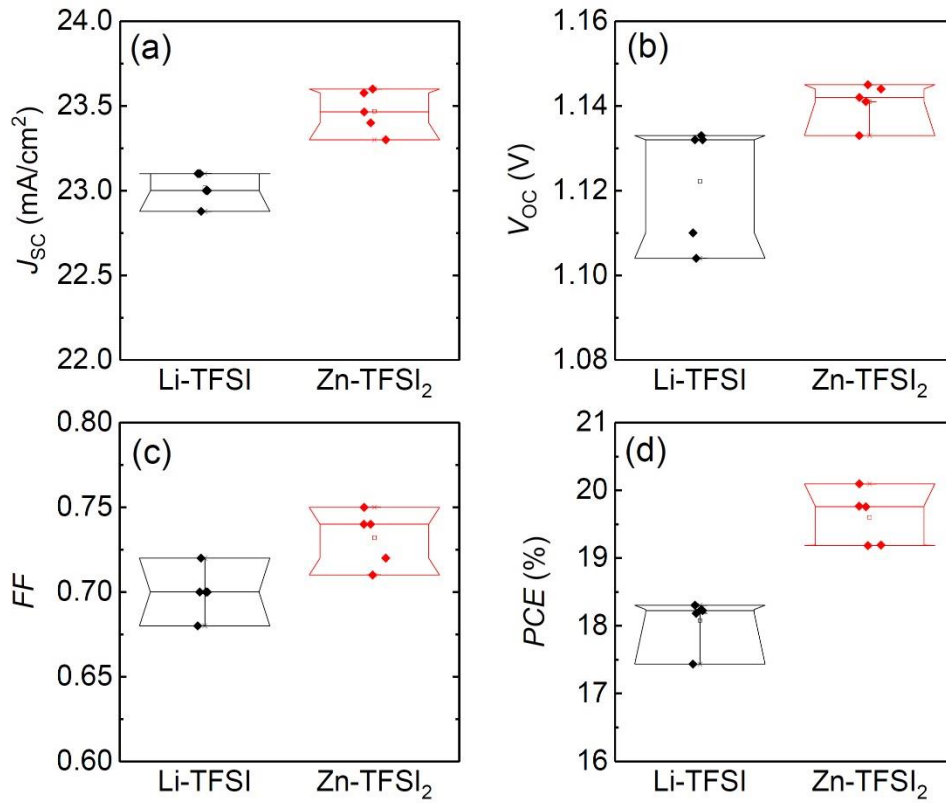
Figure 5.6 Statistical box charts for the photovoltaic parameters (a) J_{SC}, (b) V_{OC}, (c) *FF* and (d) PCE of the devices as a function of the dopant of spiro-MeOTAD (black for Li-TFSI and red for Zn(TFSI)$_2$).

5.2.3 Photovoltaic and Electronic Properties

Impedance spectroscopy (IS) measurements were carried out under illumination to study charge recombination behavior related to the photovoltaic properties. At certain applied bias voltage, two distinctive arcs were observed from Nyquist plot (Figure 5.7). To date, various equivalent circuits were adopted for adequate interpretations of charge-transfer mechanism in the perovskite solar cell. Nevertheless, a determination of the eligible equivalent circuit is still under debate owing to the unusual phenomena relating with the ion migration.[22-24] Here, we used a simplified equivalent circuit, consisting of one resistance (R) and two parallel resistance (R) and capacitance (C) components in series, where the latter R-C component assigned to low frequency range was used to estimate the recombination resistance (R$_{rec}$).[11,25] Figure 5.8 shows R$_{rec}$ as a function of applied voltage (*V$_{app}$*, forward bias) from short circuit condition to near open-circuit condition. Little difference was found in R$_{rec}$ at short-circuit condition (*V$_{app}$*=0 V), which was in accordance with comparable *J$_{SC}$*

values for Li-TFSI and Zn(TFSI)$_2$. However, the difference in R$_{rec}$ became intensified with increasing V_{app} from 0 V to 0.6 V due to the rapid decrease in R$_{rec}$ of Li-TFSI, leading to roughly one order magnitude of larger R$_{rec}$ for Zn(TFSI)$_2$ at 0.6 V. As V_{app} further increased, the external bias voltage (V_{app}) was applied across the device in the reverse direction of the internal electric field, where the carriers were prone to recombine, resulting in the low R$_{rec}$. The substantial difference of R$_{rec}$ between Zn(TFSI)$_2$ and Li-TFSI was maintained up to 0.9 V and then decreased as approaching toward V_{OC}. The significant difference in R$_{rec}$ near maximum power point (~0.9 V) was immediately reflected in the *FF* of devices and thus demonstrated higher *FF* for Zn(TFSI)$_2$.
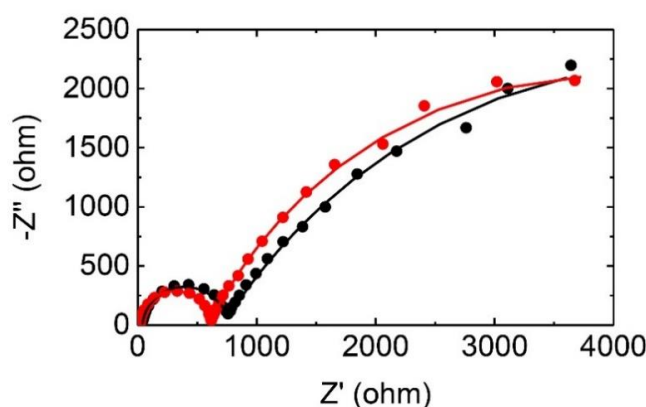
Figure 5.7 Nyquist plots (dots) and fitting curves (line) (V_{app}=0.0 V) of the devices with Li-TFSI (black) and Zn(TFSI)$_2$ (red) as dopants for spiro-MeOTAD.
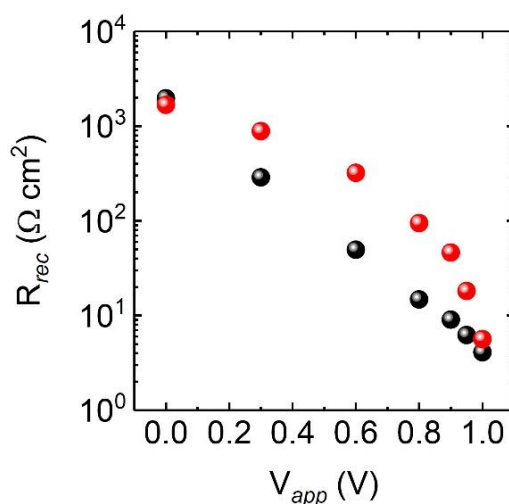

Figure 5.8 Recombination resistance (R$_{rec}$) of the devices employing Li-TFSI (black) and Zn(TFSI)$_2$ (red) as a function of applied voltage (V_{app}).

It was found that the devices with Zn(TFSI)$_2$ showed overall higher V_{OC} compared to the ones with Li-TFSI (Figures 4.5– 4.6). This can be related to the shift of the Fermi level of spiro-MeOTAD by adding a dopant.[26] The Mott-Schottky analysis was thus considered to understand the origin of the difference in V_{OC}. For the reliable data acquisition of the depletion layer capacitance (C_{dl}), the measurement frequency must be carefully selected to avoid being influenced by the huge accumulation capacitance (C_s) near the selective contact.[27] Therefore, the frequency (13.4 kHz) was chosen from the clear capacitive plateau of the capacitance (C)-frequency (f) curve in the intermediate frequency range, corresponding to dielectric response. In Figure 5.9, three distinctive capacitive features, geometric capacitance (C_g), C_{dl} and C_s, are clearly shown as a function of bias voltage (V_{app}), which allowed us to extract C_{dl} and subsequently obtain the built-in potential (V_{bi}) according to the following equation

$$C_{dl}{}^{-2} = 2(V_{bi} - V)/q\varepsilon\varepsilon_0 N \qquad (5.1)$$

where q, ε, ε_0 and N are elementary charge, relative dielectric constant, vacuum permittivity and defect density, respectively.[27,28] The V_{bi} of the device with Zn(TFSI)$_2$ was found to be 1.28 V which was 80 mV higher than the one with Li-TFSI (V_{bi}=1.20 V). In the semiconductor heterojunction, a depletion layer is generated to compensate the potential barrier by equalizing the Fermi levels. [28] Consequently, the difference in V_{bi} indicates that the employment of Zn(TFSI)$_2$ instead of Li-TFSI effectively shifted the Fermi level of the spiro-MeOTAD downward by reaching high p-doping level resulting in higher V_{OC}. Decreasing the voltage increases the depletion layer width until at about 0.6 V it spans across the whole perovskite film and no further extension is possible. As a consequence, the C_{dl} remains constant upon further reduction of applied potential
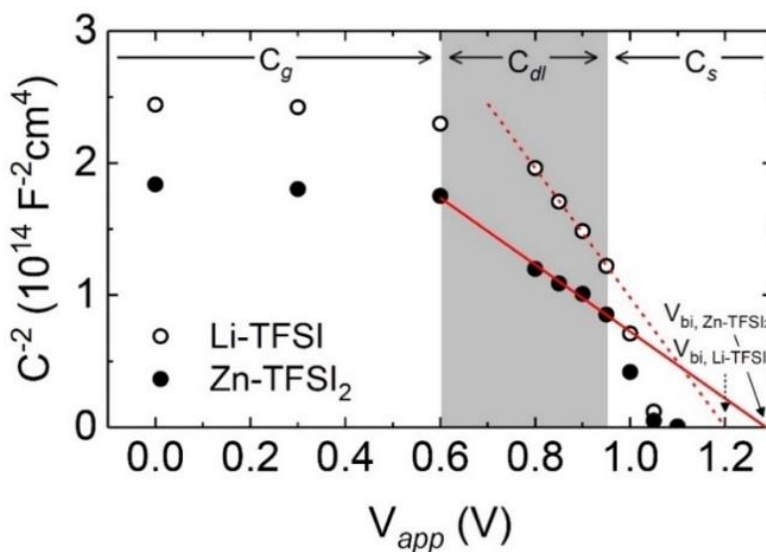
Figure 5.9 Mott-Schottky plots of devices using Li-TFSI (open circle, dash line) and Zn(TFSI)$_2$ (closed circle, solid line) as dopants for spiro-MeOTAD. The capacitance was measured in the dark at the intermediate frequency (13.4 kHz).

The introduction of Zn(TFSI)$_2$ as a dopant for the spiro-MeOTAD showed evident enhancement in photovoltaic performance compared to the conventional Li-TFSI. The concentration of Zn(TFSI)$_2$ was thus varied to find the optimal composition of HTM (as shown in Figure 5.10). The best performance was obtained from 0.30 molar ratio of Zn-TFSI$_2$ to the spiro-MeOTAD. The corresponding *I-V* curves are shown in Figure 5.11a, demonstrating 23.78 mA/cm^2 of J_{SC}, 1.162 V of V_{OC}, 0.788 of FF and 22.00% of PCE at RS under 0.989 sun intensity. The FS under the same sun intensity produced 23.75 mA/cm^2 of J_{SC}, 1.153 V of V_{OC}, 0.729 of FF and 20.17% of PCE. The corresponding IPCE spectrum is shown in Figure 5.12. Therefore, the stabilized power was monitored at maximum power point (mpp) as a function of time (Figure 5.11b), showing the resulting power output of 22 mW/cm^2.
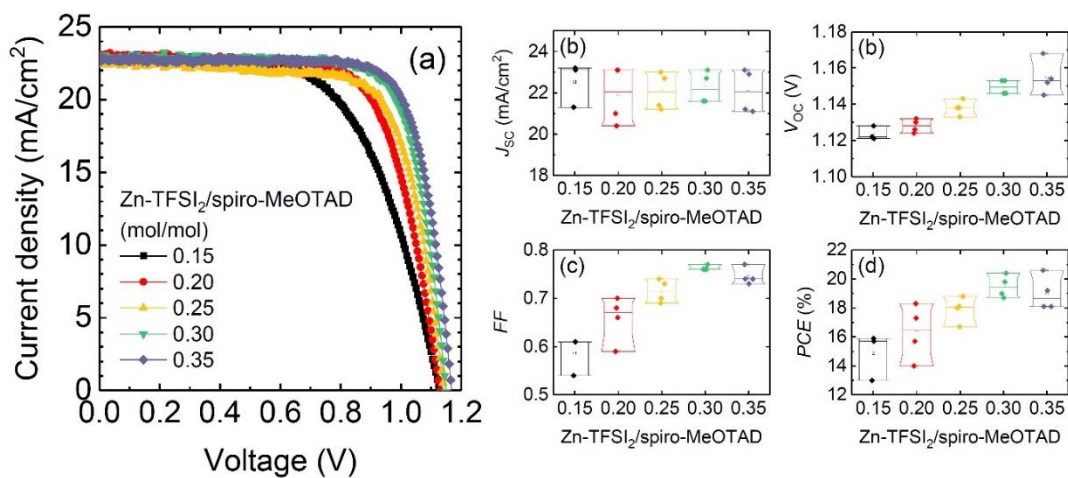
Figure 5.10 (a) *I-V* curves of the devices depending on the concentration of $Zn(TFSI)_2$ in comparison to the spiro-MeOTAD. Statistical box charts of (b) J_{SC}, (c) V_{OC}, (d) FF and (e) PCE as a function of the concentration of $Zn(TFSI)_2$.
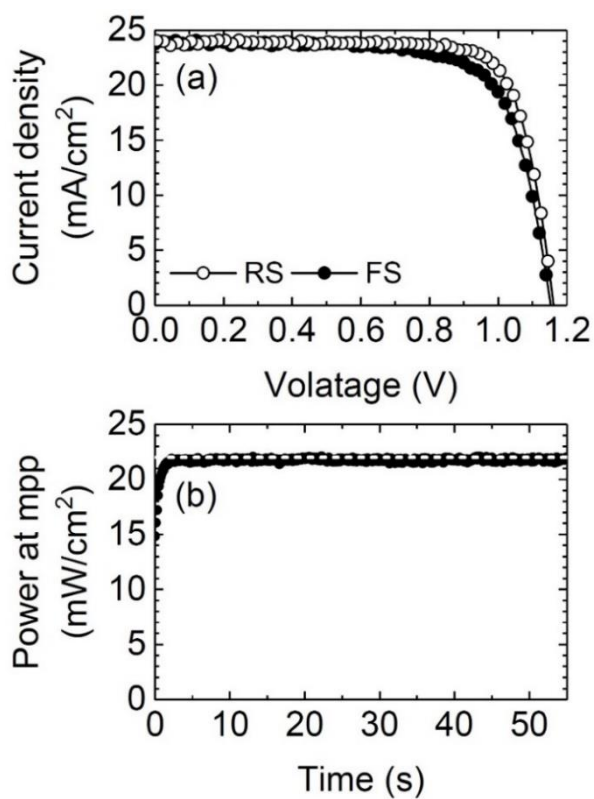

Figure 5.11 The (a) *I-V* curve and (b) time-dependent PCE at the maximum power point of the best efficiency device with $Zn(TFSI)_2$.
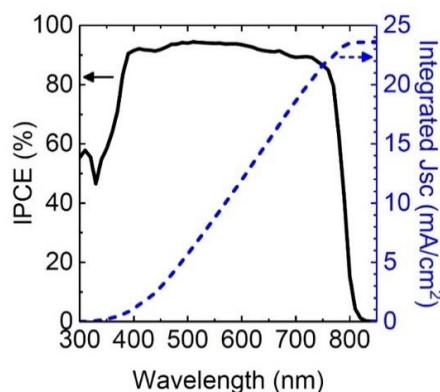
Figure 5.12 IPCE spectra of the best efficiency device with Zn(TFSI)$_2$.

5.2.4 Operational Stability

The long-term stability measurements were carried out to reveal the effect of Zn(TFSI)$_2$. During the long-term measurements, the devices were kept at mpp under continuous one sun illumination (100 mW/cm^2) in an inert atmosphere (N$_2$) at 25 °C (Figure 5.13). Strikingly, the device with Zn(TFSI)$_2$ demonstrated an outstanding photo-stability, showing even 2% increase in the beginning and stable performance for 600 h. On the contrary, the PCE of the device with Li-TFSI gradually decreased by 20% over 600 h, mainly due to the FF drop (Figure 5.14). Thermal stability under light was also measured at 50 °C (Figure 5.13b); the performance of the device with Zn(TFSI)$_2$ decreased by 21% during 100 h while the one with Li-TFSI showed 55% reduction of PCE in the same condition.
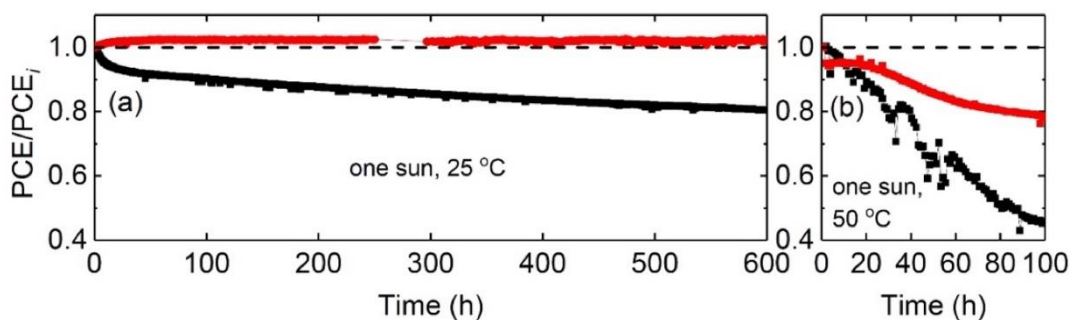
Figure 5.13 Long-term stability of devices at 25 °C (left) and (b) 50 °C (right) as a function of the dopant for the spiro-MeOTAD. Black and red symbols represent Li-TFSI and Zn(TFSI)$_2$, respectively. PCE values were divided by its initial value (PCE$_i$). Black horizontal dash line of normalized PCE at 25 °C is a guideline indicating 1.0. The devices were maintained at the maximum power point (mpp) under one sun (100 mW/cm^2) and N$_2$ atmosphere.
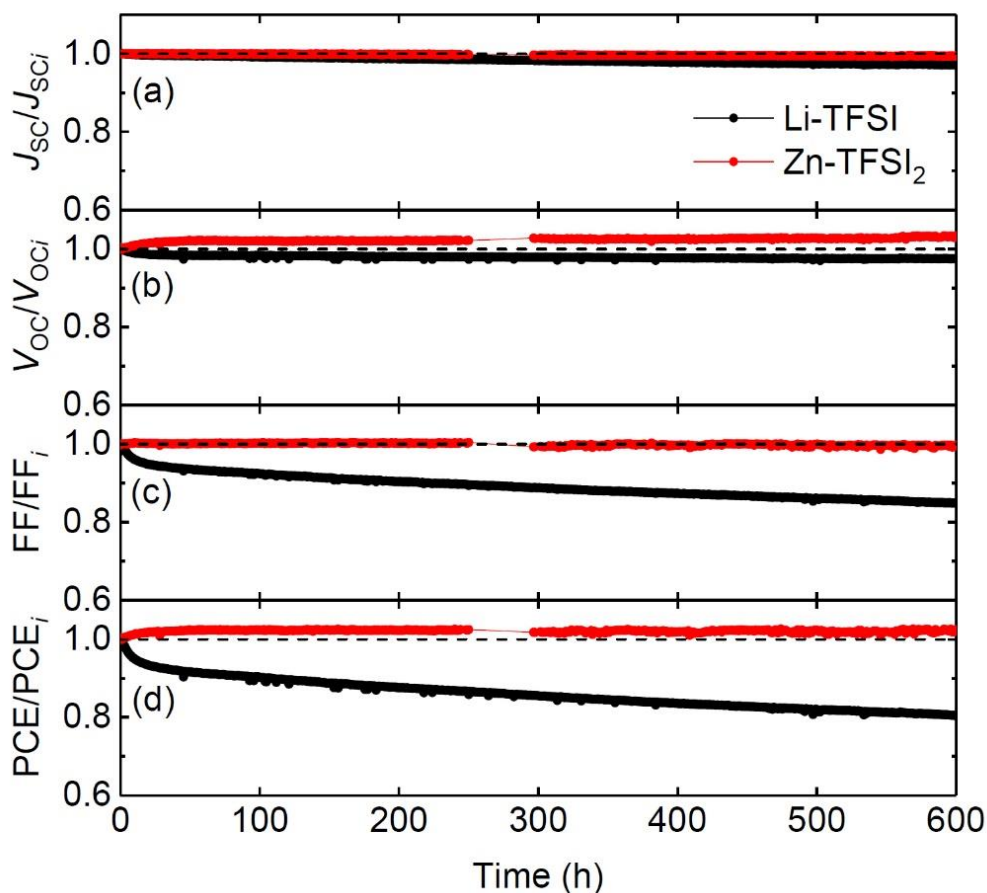
Figure 5.14 Long-term stability of photovoltaic parameters, (a) J_{SC}, (b) V_{OC}, (c) FF and (d) PCE, under one sun at 25 °C as a function of the dopant for the spiro-MeOTAD. Black and red represent Li-TFSI and Zn(TFSI)$_2$. The devices were maintained at the maximum power point (mpp) under the N$_2$ atmosphere.

The origin of photo- and thermal-stability as a function of the dopant was further investigated. It was assumed that the employment of Zn(TFSI)$_2$ instead of Li-TFSI would ensure the superb stability with outstanding efficiency, which was in accordance with the poor photo-stability of the conventional normal structure (FTO/TiO$_2$/perovskite/spiro-MeOTAD/Au) that dominantly originated from the Li-TFSI.[34] During the stability measurement at mpp, lithium cations are prone to migrate toward the perovskite layer to screen the external bias and eventually lead to degradation [29,30] In the perovskite solar cell, lithium cation migrated from the spiro-MeOTAD to the perovskite and even the TiO$_2$ layer during the device operation.[29] In case of solid-state dye-sensitized solar cells, the lithium cation was also found to migrate toward TiO$_2$ surface and directly influence the Fermi level of TiO$_2$.[30] On

the contrary, Zn-TFSI$_2$ suppressed this effect, underlying stable presence of Zn^{2+} ions in the HTM layer. The observed difference correlates with the difference in the Li$^+$and Zn^{2+}charge and ionic radii. The electric-field strength (E) of zinc ion is almost twice that of lithium ion based on the equation

$$E = q/r^2 \tag{5.2}$$

where *q* is ionic charge and *r* is ionic radius.[31] The higher *E* of Zn^{2+} would induce a strong electrostatic interaction within the spiro-MeOTAD matrix, which would hence enable the zinc ions to be well stabilized in the matrix without being significantly affected by the external bias under illumination. This was further attempted in the devices used for the long-term measurements (600 h under illumination at 25 $^\circ$C) to clarify the role of the dopant in the photo-stability. It was found that detecting the lithium or zinc distribution is very challenging in practice due to very low atomic (at) concentration of lithium (<ca. 0.4 at% with the exclusion of hydrogen) and zinc (<ca. 0.2 at% with the exclusion of hydrogen), with especially low atomic sensitivity factor (ASF) of Li 1s (ASF = 0.06) in the HTM layer.[32] Accordingly, the devices were also examined by cross-sectional SEM (Figure 5.15) after the long-term stability measurements to show little apparent difference from the device as prepared (Figure 5.15).
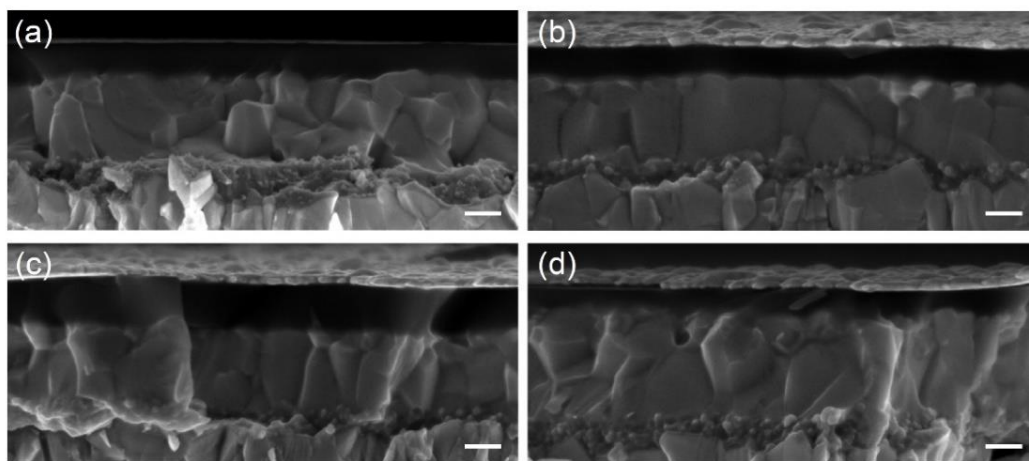
Figure 5.15 Cross-sectional scanning electron microscope (SEM) images of devices after long-term stability measurements at mpp under one sun and N$_2$ atmosphere. Device with (a) Li-TFSI and (b) Zn(TFSI)$_2$ after 600 h at 25 $^\circ$C. Device with (c) Li-TFSI and (d) Zn(TFSI)$_2$ after 100 h at 50 $^\circ$C. Scale bars represent 200 nm.

On the contrary, the poor thermal stability was mostly ascribed to the fragile morphology of the spiro-MeOTAD in the presence of the additives. In order to demon-

strate the effect, we monitored the glass transition temperature (T_g) of spiro-MeOTAD as a function of the presence of the additives. It was found that T_g significantly decreased from 154 °C to 91 °C by adding Li-TFSI, FK209 and tBP (4.16), underlying that the deteriorated stability of amorphous state can easily induce the crystallization, particularly at the elevated temperature.[10,33] The spiro-MeOTAD with Zn(TFSI)$_2$, FK209 and tBP showed slightly higher T_g of 99 °C (Figure 5.16), implying relatively improved morphological stability of spiro-MeOTAD with Zn(TFSI)$_2$ as compared to Li-TFSI. The performance drop as compared to the pristine spiro-MeOTAD however seemed inevitable irrespective of dopant. After the thermal stability measurement, the crystallization of the spiro-MeOTAD was observed by a microscope for both Li-TFSI and Zn(TFSI)$_2$ (Figure 5.17) to find crystallization of spiro-MeOTAD. Nevertheless, the enhancement of thermal stability by a careful cation design of the '-TFSI$^-$'dopant remains promising, even to potentially replace other additives and thus lead to a more stable morphology.
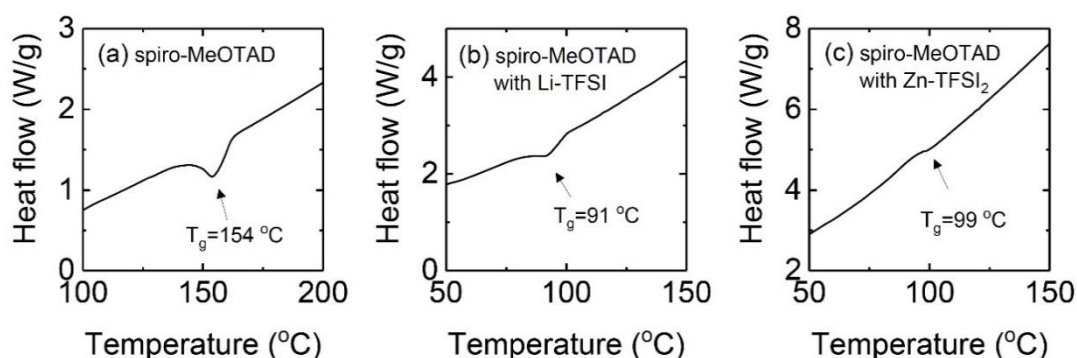
Figure 5.16 Differential scanning calorimetry (DSC) curves of (a) pristine spiro-MeOTAD, (b) spiro-MeOTAD with Li-TFSI, FK209 and tBP, and (c) spiro-MeOTAD with Zn-TFSI$_2$, FK209 and tBP. The compositional ratio was exactly the same as reported within the devices. The DSC curves were obtained from the first heating.
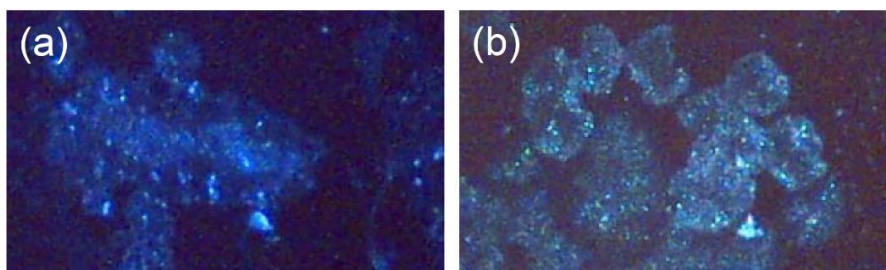
Figure 5.17 Microscope images (200x magnitude) of spiro-MeOTAD with (a) Li-TFSI and (b) Zn(TFSI)$_2$ after the thermal stability test for 100 h at 50 °C.

Finally, a possibility of Au or iodine migration at high temperature is known to be a major reason for the poor thermal-stability.[34] However, the effect of Au or iodine migration was negligible in this study,[10] where the Au layers maintained intact, showing a clear interface of Au layer even after the thermal stability measurements (Figure 5.15). A depth profiling with X-ray photoelectron spectroscopy (XPS) was also carried out for the device with Li-TFSI after the thermal stability measurements (Figure 5.18), which confirmed well separated Au, HTM and perovskite layers in accordance with the enhanced stability of the devices.
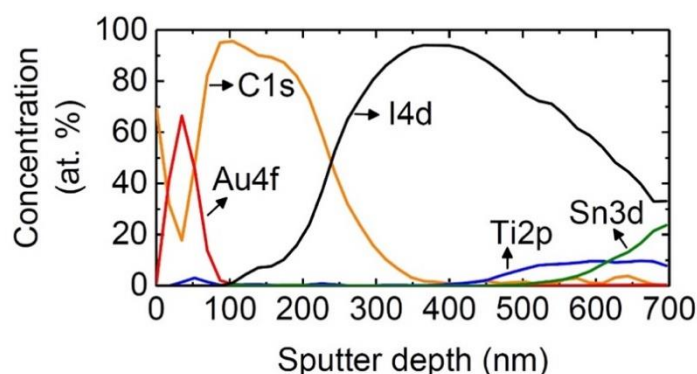
Figure 5.18 X-ray photoelectron spectroscopy (XPS) depth profiling of the device with Li-TFSI after the thermal stability test for 100 h at 50 $^\circ$C.

5.3   Conclusions

In conclusion, $Zn(TFSI)_2$ was successfully employed in spiro-MeOTAD as an efficient dopant, leading to the improved hole separation and hole mobility compared to the conventional dopant, Li-TFSI. The replacement of Li-TFSI with $Zn(TFSI)_2$ effectively shifted the Fermi level of spiro-MeOTAD downward that resulted in higher V_{OC} of the photovoltaic device. The device with $Zn(TFSI)_2$ also demonstrated improved FF based on about one order magnitude higher recombination resistance than the one with Li-TFSI, particularly near the maximum power point. Consequently, the perovskite solar cell based on spiro-MeOTAD with $Zn(TFSI)_2$ achieved outstanding stabilized PCE of 22%. Furthermore, the long-term stability of the perovskite solar cell was remarkably enhanced by incorporating $Zn(TFSI)_2$, which suggested a stronger interaction between $Zn(TFSI)_2$ and spiro-MeOTAD, which suppressed the migration of cations that would occur in case of Li-TFSI. Thermal stability of the device with $Zn-TFSI_2$ was also significantly improved in comparison with the one with Li-TFSI, owing to a higher T_g for $Zn(TFSI)_2$. This study provides a

basis for promising stability of the high efficiency perovskite devices with spiro-MeOTAD through dopant design.

5.4   Experimental

Substrate preparation. Nippon Sheet Glass 10 Ω/sq was cleaned by sonication in 2% Hellmanex (Hellma GmbH) water solution for 20 min and further cleaned in ethanol and acetone for 15 min, respectively. After solvent cleaning, the substrates were cleaned with UV ozone treatment for 15 min. Then, 30nm-thick TiO_2 compact (cp) layer was deposited by spray pyrolysis with a precursor solution of titanium diiso-propoxide bis(acetylacetonate) (75 wt% in isopropanol, Sigma-Aldrich) in anhydrous ethanol ($\geq$ 99.5% Fischer Scientific) at 450 °C. After the spraying, the substrates were kept at 450 °C for 30 min and cooled down to room temperature. Then, 150-200 nm thick mesoporous (mp) TiO_2 layer was deposited by spin coating method at 4000 rpm for 20 s with an acceleration of 2000 rpm s^{-1}, using the TiO_2 paste (Dyesol 30 NR-D) diluted in ethanol. After the spin coating, the substrates were immediately dried at 120 °C for 10 min and then sintered at 500 °C for 30 min under dry air flow.

Preparation of perovskite precursor solution. 1.5 M PbI_2 (99.99%, TCI) and 1.5 M $PbBr_2$ (99.99%, TCI) were predissolved in a mixture of dimethylformamide (DMF, 99.8%, Acros) and dimethyl sulfoxide (DMSO, 99.7%, Acros) (DMF:DMSO = 4:1 v/v) as stock solutions, respectively. 1.5 M Cesium iodide (99.998%, ABCR) was also pre-dissolved in DMSO as stock solution. To make a perovskite precursor solution based on mixed triple cations and double halides, first the 1.22 M $FAPbI_3$ and $MAPbBr_3$ with 9 mol% excess lead were prepared by mixing 1.5 M lead stock solutions with formamidinium iodide ($\geq$98%, FAI, Dyesol) and methylammonium bromide (98%, MABr, Dyesol), respectively. Then, to make triple cation perovskite solutions, CsI, $FAPbI_3$ and $MAPbBr_3$ solutions were mixed with 0.3:5:1 in volume ratio.

Hole transporting layer. 70 mM Spiro-MeOTAD (99%, Merck) solution in chlorobenzene (99.8%, Acros) was doped with bis(trifluoromethylsulfonyl)imide lithium salt (Li-TFSI, 99.95%, Sigma-Aldrich) or bis(trifluoromethylsulfonyl)imide zinc salt ($Zn(TFSI)_2$, 99.5%, Solvionic), tris(2-(1H-pyrazol-1-yl)-4-tert-butylpyridine)- cobalt(III) tris(bis(trifluoromethylsulfonyl)imide) ($\geq$99.5%, FK209, Dynamo) and 4-tert-Butylpyridine (tBP, 96%, Sigma-Aldrich). The molar ratio of additives for spiro-MeOTAD was 0.5, 0.03 and 3.3 for Li-TFSI, FK209 and tBP, respectively. The molar ratio of additives for spiro-MeOTAD was x (x = 0.15, 0.20, 0.25, 0.30 or 0.35), 0.03, and 3.3 for $Zn(TFSI)_2$, FK209 and tBP, respectively.

Preparation of device. Perovskite films were deposited by anti-solvent (chloroben-zene, 99.8%, Acros) method in the N_2 atmosphere gloves box with triplication perovskite precursor solutions at 4000 rpm for 20 s with an acceleration of 2000 rpm s^{-1}. The wet perovskite films immediately were annealed for 50 min ~ 1 h at 100 $^{\circ}$C. After the films were cooled down to room temperature, spiro-MeOTAD solutions were coated on the perovskite films at 4000 rpm for 20 s with an acceleration of 2000 rpm s^{-1}. To finalize preparation of devices, 80 nm thick Au electrode was further deposited on the FTO/cp-TiO$_2$/mp-TiO$_2$/perovskite/spiro-MeOTAD films.

Devices measurement. Current-voltage (*IV*) property of the hole-only device (FTO/spiro-MeOTAD/Au) was measured in dark to obtain charge limited current (SCLC). The hole mobility was calculated according to following the equation,

$$J = 9/8\varepsilon_r\varepsilon_0\mu V^2 L^{-3} \quad (5.3)$$

where *J*, ε_r, ε_0, μ, *V*, and *L* denote current, relative dielectric constant ($\varepsilon_r = 3$ was used here), vacuum permittivity, hole mobility, applied voltage, and film thickness, respectively. The scanning electron microscopy (SEM) images were collected from high resolution SEM (ZEISS Merlin) with In-lens detector. Florolog 322 (Horiba Jobin Ybon Ltd) instrument was used to record the steady-state photoluminescence (PL). The samples were mounted at 60° and the emission was detected at 90° from the incident beam path. 450 nm was used as an excitation wavelength for perovskite. Current density-voltage (*IV*) curves and time-dependent power conversion efficiency of the devices were measured using a 450 W xenon light source (Oriel). Schott K113 Tempax filter (Präzisions Glas & Optik GmbH was used to reduce mismatch of spectrum between AM 1.5G and the simulated illumination. For calibration of light intensity, a Si photodiode equipped with an IR-cutoff filter (KG3, Schott) was recorded during each measurement. *I-V* characteristics of the cells were obtained by applying an external voltage bias while measuring the current response with a digital source meter (Keithley 2400) with voltage scan rate was 10 mVs^{-1} and without any device preconditioning on devices. A black metal mask (0.16 cm^2) was used during the measurements to avoid overestimation by scattered light. Impedance spectroscopy (IS) measurements were performed using a potentiostat (BioLogic, MPG2) equipped with LED light source. 20 mV of sinusoidal AC perturbation, ranging from 1 MHz to 10 mHz, was put on the DC bias voltage from 0 V to 1 V. A black aperture mask (0.25 cm^2) was also used for the IS measurement under the light. The obtained IS data were fit by using a software (ZView2) where one resistance and two resistance (R)-capacitance (C) (R-C in parallel) in series were used as an equivalent circuit. Capacitance was measured in dark as a function of bias voltage (forward bias)

for the Mott-Schottky plots. Frequency scan was done before the C-V measurements to find out the optimal frequency where three distinctive capacitance regions were observed. Subsequently, a sinusoidal AC voltage (20 mV) with 13.4 kHz was applied on the DC bias voltage and resultant capacitance was recorded. Stability measurements were performed with a Biologic MPG2 potentiostat under an AM 1.5G Sun-equivalent white LED lamp. The devices with a metal aperture mask (0.16 cm^2) were mounted in the sample holder flushed with nitrogen. The devices were measured with a maximum power point (mpp) tracking under constant illumination. The mpp was updated every 10 s by a standard perturb and the resulting *I-V* curves was recorded for every 60 min in order to track the evolution of individual *I-V* parameters. Glass transition temperature (T$_g$) were obtained from differential scanning calorimetric (DSC) measurements. The samples were submitted to two consecutive heating cycles from room temperature to 300 °C at a scanning rate of 10 °C/min under nitrogen atmosphere using a PerkinElmer DSC8000 differential scanning calorimeter. X-ray photoelectron spectroscopy (XPS) measurements were used to investigate element composition with PHI VersaProbe II scanning XPS microprobe (Physical Instruments AG, Germany). 2 kV Ar ion sputtering was used for depth analysis and data was collected at a rate of 7 nm/min. The microscope images (x200 magnification) were obtained by electronic microscope (Intel Play QX3 Microscope, Intel) with software (QXScope 1.0.5.). Incident-photon-to-current efficiency (IPCE) spectra were measured by the Ariadne system (Cicci Research) with an aperture mask (0.16 cm^2) for the device. X-ray photoelectron spectroscopy (XPS) measurements were used to investigate element composition with PHI VersaProbe II scanning XPS microprobe (Physical Instruments AG, Germany). 2 kV Ar ion sputtering was used for depth analysis and data was collected at a rate of 7 nm/min. The microscope images (x200 magnification) were obtained by electronic microscope (Intel Play QX3 Microscope, Intel) with software (QXScope 1.0.5.). Incident-photon-to-current efficiency (IPCE) spectra were measured by the Ariadne system (Cicci Research) with an aperture mask (0.16 cm^2) for the device.

References

[1] H. S. Kim, C. R. Lee, J. H. Im, K. B. Lee, T. Moehl, A. Marchioro, S. J. Moon, R. Humphry-Baker, J. H. Yum, J. E. Moser, M. Grätzel, N. G. Park, *Sci. Rep.* **2012**, *2*.

[2] M. M. Lee, J. Teuscher, T. Miyasaka, T Murakami, TN Snaith, HJ, *Science.* **2012**, *338*, 647.

[3] http://www.nrel.gov/pv/assets/images/efficiency-chart.png.

[4] G. Giorgi, J. I. Fujisawa, H. Segawa, K. Yamashita, *J. Phys. Chem. Lett.* **2013**, *4*, 4213.

[5] G. Xing, N. Mathews, S. Sun, S. S. Lim, Y. M. Lam, M. Graïzel, S. Mhaisalkar, T. C. Sum, *Science.* **2013**, *342*, 344.

[6] S. D. Stranks, G. E. Eperon, G. Grancini, C. Menelaou, M. J. P. Alcocer, T. Leijtens, L. M. Herz, A. Petrozza, H. J. Snaith, *Science.* **2013**, *342*, 341.

[7] H. Zhu, K. Miyata, Y. Fu, J. Wang, P. P. Joshi, D. Niesner, K. W. Williams, S. Jin, X. Y. Zhu, *Science.* **2016**, *353*, 1409.

[8] K. Miyata, T. L. Atallah, X. Y. Zhu, *Sci. Adv.* **2017**, *3*, DOI 10.1126/sciadv.1701469.

[9] K. X. Steirer, P. Schulz, G. Teeter, V. Stevanovic, M. Yang, K. Zhu, J. J. Berry, *ACS Energy Lett.* **2016**, *1*, 360.

[10] X. Zhao, H.-S. Kim, J.-Y. Seo, N.-G. Park, *ACS Appl. Mater. Interfaces* **2017**, *9*, 7148.

[11] H. S. Kim, J. Y. Seo, N. G. Park, *J. Phys. Chem. C* **2016**, *120*, 27840.

[12] H. S. Kim, J. Y. Seo, N. G. Park, *ChemSusChem* **2016**, *9*, 2528.

[13] B. Xu, J. Huang, H. A˚gren, L. Kloo, A. Hagfeldt, L. Sun, *ChemSusChem* **2014**, *7*, 3252.

[14] J. Burschka, F. Kessler, M. K. Nazeeruddin, M. Grätzel, *Chem. Mater.* **2013**, *25*, 2986.

[15] P. Wang, J. Zhang, Z. Zeng, R. Chen, X. Huang, L. Wang, J. Xu, Z. Hu, Y. Zhu, *J. Mater. Chem. C* **2016**, *4*, 9003.

[16] W. H. Nguyen, C. D. Bailie, E. L. Unger, M. D. Mcgehee, *J. Am. Chem. Soc.* **2014**, *136*, 10996.

[17] A. Pellaroque, N. K. Noel, S. N. Habisreutinger, Y. Zhang, S. Barlow, S. R. Marder, H. J. Snaith, *ACS Energy Lett.* **2017**, *2*, 2044.

[18] H. Djellab, M. Armand, D. Delabouglise, *Synth. Met.* **1995**, *74*, 223.

[19] M. Armand, F. Endres, D. R. MacFarlane, H. Ohno, B. Scrosati, *Nat. Mater.* **2009**, *8*, 621.

[20] A. Abate, T. Leijtens, S. Pathak, J. Teuscher, R. Avolio, M. E. Errico, J. Kirkpatrik, J. M. Ball, P. Docampo, I. McPherson, H. J. Snaith, *Phys. Chem. Chem. Phys.* **2013**, *15*, 2572.

[21] M. Saliba, T. Matsui, J.-Y. Seo, K. Domanski, J.-P. Correa-Baena, M. K. Nazeeruddin, S. M. Zakeeruddin, W. Tress, A. Abate, A. Hagfeldt, M. Grätzel, *Energy Environ. Sci.* **2016**, *9*, 1989.

[22] C. Eames, J. M. Frost, P. R. F. Barnes, B. C. O'Regan, A. Walsh, M. S. Islam, *Nat. Commun.* **2015**, *6*, 7497.

[23] B. Chen, M. Yang, X. Zheng, C. Wu, W. Li, Y. Yan, J. Bisquert, G. Garcia-Belmonte, K. Zhu, S. Priya, *J. Phys. Chem. Lett.* **2015**, *6*, 4693.

[24] H. S. Kim, I. H. Jang, N. Ahn, M. Choi, A. Guerrero, J. Bisquert, N. G. Park, *J. Phys. Chem. Lett.* **2015**, *6*, 4633.

[25] E. J. Juarez-Perez, M. Wußler, F. Fabregat-Santiago, K. Lakus-Wollny, E. Mankel, T. Mayer, W. Jaegermann, I. Mora-Sero, *J. Phys. Chem. Lett.* **2014**, *5*, 680.

[26] R. Schölin, M. H. Karlsson, S. K. Eriksson, H. Siegbahn, E. M. J. Johansson, H. Rensmo, *J. Phys. Chem. C* **2012**, *116*, 26300.

[27] O. Almora, C. Aranda, E. Mas-Marzá, G. Garcia-Belmonte, *Appl. Phys. Lett.* **2016**, *109*, DOI 10.1063/1.4966127.

[28] S. M. Sze, K. K. Ng, *Physics of Semiconductor Devices*, **2007**. 3rd ed. (John Wiley & Sons, Hoboken, New Jersey, 2007), p. 832.

[29] Z. Li, C. Xiao, Y. Yang, S. P. Harvey, D. H. Kim, J. A. Christians, M. Yang, P. Schulz, S. U. Nanayakkara, C.-S. Jiang, J. M. Luther, J. J. Berry, M. C. Beard, M. M. Al-Jassim, K. Zhu, *Energy Environ. Sci.* **2017**, *10*, 1234.

[30] L. Yang, B. Xu, D. Bi, H. Tian, G. Boschloo, L. Sun, A. Hagfeldt, E. M. J. Johansson, *J. Am. Chem. Soc.* **2013**, *135*, 7378.

[31] D. M. Loprete, K. A. Hartman, *Biochemistry* **1993**, *32*, 4077.

[32] Z. Hawash, L. K. Ono, S. R. Raga, M. V. Lee, Y. Qi, *Chem. Mater.* **2015**, *27*, 562.

[33] T. Malinauskas, D. Tomkute-Luksiene, R. Sens, M. Daskeviciene, R. Send, H. Wonneberger, V. Jankauskas, I. Bruder, V. Getautis, *ACS Appl. Mater. Interfaces* **2015**, *7*, 11107.

[34] K. Domanski, J. P. Correa-Baena, N. Mine, M. K. Nazeeruddin, A. Abate, M. Saliba, W. Tress, A. Hagfeldt, M. Grätzel, *ACS Nano* **2016**, *10*, 6306.

Conclusions

Perovskite solar cells are a very promising photovoltaic technology due its unique properties and low cost of materials, showing rapid progress in power conversion efficiency in a surprisingly short period of development. However, still many drawbacks remain behind this progress, which particularly refers to the possibility to further improve efficiency and stability of PSCs. The studies involved in this thesis aim at understanding roles of perovskite, ETL, and HTL in the PSCs and investigating the molecular engineering approach of three main compenents of PSCs towards high efficiency and stability of perovskite solar cells.

Firstly, we demonstrated the mechanism of perovskite crystal growth fabricated by anti-solvent method, as detailed in Chapter 2, with the strategy to control crystal growth with small molecules, methylammonium formate (MAF). We showed that MAF can selectively interact with Pb(II) ions, which can retard PbI_2-methylammonium iodide interaction in the formation of the perovskite. This successfully results in larger grain size favourable to device performance owing to higer V_{OC} with less recombination in the grain boundaries. This study was focused on the planar structured PSC to show more effective charge transport, which resulted in higher power conversion efficiency compared to the state-of-the-art devices.

Next, the study on crystallization of perovskite was detailed in Chapter 3. We demostrated the incorporation of Cs and MA into the perovskite structure at room temperature to affect the crystallization of mixed cation perovskites (MA_xFA_y-PbI_xBr_y). We showed that the presence of both Cs and MA was necessary to obtain the photoactive crystalline perovskite phase with high-quality crystals, and we achieved a PCE of 18% using optimized $FA_{0.8}MA_{0.1}Cs_{0.1}$ cation mixture without annealing or any post treatment at room temperature. Moreover, the efficiencies of 17% were reproduced for planar perovskite solar cell architectures, showing great potential for low-cost, large-scale manufacturing procedures, such as the roll-to-roll process.

In Chapter 4, our work moved to mp-TiO_2 as electon transporing material motivated by the scarcity of the studies on mp-TiO_2, despite the record PCEs persistently involving mesoscopic structures of PSCs. We introduced for the first time 40 nm size TiO_2 particles being endowed with mesopores to augment the contact area with the

perovskite from 60 m^2/g for the conventional scaffold to over 200 m^2/g. In addition, we sucessfully passivated electronically the surface of the mp-TiO$_2$ by treatment with cesium bromide, resulting in PCEs up to 21% with negligible hysteresis.

Finally, in Chapter 5, we studied a novel p-dopant, Zn(TFSI)$_2$, in PSCs. Intrinsic stability issues of spiro-OMeTAD is a critical problem to be solved for commercialization of PSCs. The main factor influencing the stability of spiro-OMeTAD is considered to be related to dopants, such as Li-TFSI and Cobalt complexes (FK209). Unlike the FK209, Li-TFSI is a necessary dopant for oxidizing spiro-OMeTAD. However, we found that the fast degradation of device performance of PSCs relates to Li-TFSI-doped spiro-OMeTAD. On the contrary, the device with Zn(TFSI)$_2$ demonstrated improved performance, showing outstanding stabilized PCE of 22%, based on about an order of magnitude higher recombination resistance than the one with Li-TFSI. Furthermore, the long-term stability of the perovskite solar cell was remarkably enhanced by incorporating Zn(TFSI)$_2$, which provides a basis for promising stability of the high efficiency perovskite devices with spiro-MeOTAD through dopant design.

In summary, the work presented in this thesis demonstrates how refined molecular modifications in perovskite solar cells improved the overall performance of PSCs. The strategy of rational design by introducing molecules having chemical compatibility to materials already used in PSCs helps resolving intrinsic defects of perovskite, ETM and HTM, leading to high performance and stability. I hope that molecular engineering presented in the thesis will motivate a future research to contribute towards high efficient and stable perovskite solar cells

Acknowledgement

First of all, I would like to thank my thesis director and supervisor, Prof. Michael Grätzel for providing me a very precious opportunity to work in the Laboratory of Photonics and Interfaces. Special thanks to Prof. Michael Graetzel as an excellent advisor for giving me the freedom for research and support my work. I really appreciate that. I am truly impressed by him, whose passion for resarch is respectable; he became my role model. I also would like to thank my co-supervisor, Dr. Zakeerunddin, for not only the scienctific but also personal advices. Whenenver I had difficult moments in the lab, he always engcourged me, and I felt better so that I overcomed my emotional slump during my PhD.

I would further like to thank my PhD committee, Prof. A. Hagfeldt, Prof. A. Di Carlo, Prof. F. Nüesch and Prof. J.-E. Moser.

Special thanks to all LPI members, they create a great atmosphere of a group where I could get motivated and finally developed myself a lot. In particular, I would like to thank my dream team memebers, Antonio, Fabrizio, Juanpa, Michael S. and Taisuke! I learned many pratical knowledge of perovskite solar cells from them and I never forget all the moment working with them. At the same time, I would like to thank the collaborators Seckin and Iranian girls, Maboobeh, Elham and Sommayeh, who were the most energenic, always singing in the evening in their office. I appreciate my best friend and office-mate, Yasemin, who began her PhD at the same time as me; because of her I was not lonely and bored in the office for every day. I thank to Koreans in our group, Hui-Seon, Jeong-Hyeuk and Minkyu for talking with me in Korean. It made me feel less home sick. I also would like to thank Heidi, Carmen, Pechy and Paul for supporting me. I really feel greatful to Jovana. I always enjoyed disussing the project with her from a chemist point of view and appreciated her advises on the scientific writting regarding my thesis.

Finally, I would like to thank my previous supervisor, Prof. Kwon, who encuraged me to start my PhD in Switzerland when I was considering it. I must thank my family and friends who always support and encourge even though we are in the different places.

Thank you all!

Curriculum Vitae (2018)

PhD. Ji-Youn Seo
Laboratory of Photonics and Interfaces (LPI)
École polytechnique fédérale de Lausanne
Mobile: +41 76 475 07 07
E-mail: seo.jiyoun@yahoo.com

EDUCATION and RESEARCH EXPERIENCES

2015 – 2018 **PhD of Chemistry & Chemical Engineering (Supervisor: Prof. Michael Gratzel)**
Laboratory of Photonics and Interfaces, EPFL, Switzerland

2011 – 2015 Research Engineer, Materials Research Team, Research & Development Division
Hyundai Motor Company, Korea

2009 – 2011 Master of Material Chemistry (Supervisor: Prof. O-Pil Kwon)
Functional Organic Materials Laboratory, Ajou University, Korea

2005 – 2009 Bachelor of Applied Chemistry, Ajou University, Korea

RESEARCH SUMMARY

➢ **Main Topic: Organic, Inorganic and Hybrid Materials for Electronics and Photonics**

➢ **4 fist author papers in recent 3 years** (*Adv. Mater, Adv. Funct. Mater. and Adv. Energy Mater.*)
with total 21 SCI publications (total 7 first author papers since 2009)

➢ **38 patents of materials and processes for Automotive applications**

Photonics and Electronic Materials

▪ Organic-Inorganic Hybrid Solar cells

▪ Organic pi-conjugated Molecules and Crystals for Photonics

▪ Metal-Organic Hybrid Polymers

Organic and Inorganic Materials for Industry Applications

▪ New Metal-Organic Precursors Synthesis

▪ Thin Film Coatings with PECVD, CVD, ALD System

▪ Inorganic-Organic Composited Insulating Coatings

▪ Bioplastics

PUBLICATION LIST

First Author Publications

1. **Seo, J**., Uchida, R., Kim, H., Saygili, Y., Luo, J., Moore, C., McIntyre, R.., Zakeeruddin, S. M., Grätzel, M., Hagfeldt, Graetzel, M. Boosting the Efficiency of Perovskite Solar Cells with CsBr-Modified Mesoporous TiO_2 Beads as Electron-Selective Contact. *Advanced Functional Materials*. 28, 1705763 (2018).

2. Matsui, T.,[†] **Seo, J. Y**.,[†] Saliba, M., Zakeeruddin, S. M., Gratzel, M. Room-Temperature Formation of Highly Crystalline Multication Perovskites for Efficient, Low-Cost Solar Cells. *Advanced Materials*, *29*(15). (2017). (†equal contribution)

3. **Seo, J.-Y.**, Matsui, T., Luo, J., Correa-Baena, J.-P., Giordano, F., Saliba, M., Abate, A. Ionic Liquid Control Crystal Growth to Enhance Planar Perovskite Solar Cells Efficiency. *Advanced Energy Materials*, 1600767. (2016). (Frontispiece)

4. **Seo, J.-Y**[†], Kim, H.,[†] Akin. S., Stojanovic, M., Hagfeldt. A., Zakeeruddin, S. M., Gratzel, M. Novel p-Dopant Toward Highly Efficient and Stable Perovskite Solar Cells (submitted, 05.2018) (†equal contribution)

5. **Seo, J.-Y.**, Jazbinsek, M., Choi, E.-Y., Lee, S.-H., Yun, H., Kim, J.-T., Kwon, O.-P. Unusual twisting and bending of phenyltriene with methylthiolated biphenyl sulfane group in the crystalline state. *Crystal Growth & Design*, *13*(3), 1014–1022. (2013).

6. **Seo, J.-Y.**, Lee, S.-H., Jazbinsek, M., Yun, H., Kim, J.-T., Lee, Y. S., Kwon, O.-P. New Thiolated Nitrophenylhydrazone Crystals for Nonlinear Optics. *Crystal Growth & Design*, *12*(1), 313–319. (2011).

7. **Seo, J.-Y.**, Choi, S.-B., Jazbinsek, M., Rotermund, F., Günter, P., Kwon, O.-P. Large-size pyrrolidine-based polyene single crystals suitable for terahertz wave generation. *Crystal Growth & Design*, *9*(12), 5003–5005. (2009).
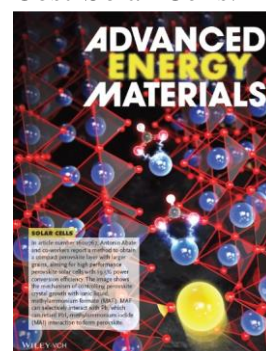
Highlighted Co-author Publications

8. The effect of illumination on the formation of metal halide perovskite films.
Nature, *545*(7653), 208. (2017)
Ummadisingu, A., Steier, L., **Seo, J.-Y**., Matsui, T., Abate, A., Tress, W., Grätzel, M.

9. Incorporation of rubidium cations into perovskite solar cells improves photovoltaic performance.
Science, *354*(6309), 206. (2016).
Saliba, M., Matsui, T., Domanski, K., **Seo, J.-Y.**, Ummadisingu, A., Zakeeruddin, S. M., Gratzel, M

10. Cesium-containing triple cation perovskite solar cells: improved stability, reproducibility and high efficiency
Energy Environ. Sci., *9*, 1989. (2016) *Citation 1229* **(05.2018)**
M. Saliba, T. Matsui, **J.-Y. Seo**, K. Domanski, J.-P. Correa-Baena, M. K. Nazeeruddin, S. M. Zakeeruddin, W. Tress, A. Abate, A. Hagfeldt, M. Grätzel

PUBLICATION LIST

Other Publications

11. E. Halvani Anaraki, A. Kermanpur, M. T. Mayer, L. Steier, T. Ahmed, S.-H. Turren-Cruz, **J. Seo**, J. Luo, S. M. Zakeeruddin, W. R. Tress, T. Edvinsson, M. Grätzel, A. Hagfeldt, J.-P. Correa-Baena, *ACS Energy Lett.* 773. (2018).

12. Ummadisingu, A., **Seo, J.-Y.**, Stojanovic, M., Zakeeruddin, S. M., Grätzel, M., Hagfeldt, A., Saliba, M. Additives, Hole Transporting Materials and Spectroscopic Methods to Characterize the Properties of Perovskite Films. *CHIMIA International Journal for Chemistry*, *71*(11), 754–761. (2017).

13. Kim, H.-S., **Seo, J.-Y.**, Xie, H., Lira-Cantu, M., Zakeeruddin, S. M., Grätzel, M., Hagfeldt, A. Effect of Cs-Incorporated NiO x on the Performance of Perovskite Solar Cells. *Acs Omega*, *2*(12), 9074–9079. (2017).

14. Hadadian, M., Correa-Baena, J., Goharshadi, E. K., Ummadisingu, A., **Seo, J.**, Luo, J., Abate, A. Enhancing Efficiency of Perovskite Solar Cells via N-doped Graphene: Crystal Modification and Surface Passivation. *Advanced Materials*, *28*(39), 8681–8686. (2016).

15. Petrov, A. A., Pellet, N., **Seo, J.-Y.**, Belich, N. A., Kovalev, D. Y., Shevelkov, A. V, Graetzel, M. New insight into the formation of hybrid perovskite nanowires via structure directing adducts. *Chemistry of Materials*, *29*(2), 587–594. (2016).

16. Y. H. Lee, J. Luo, M. K. Son, P. Gao, K. T. Cho, **J. Seo**, S. M. Zakeeruddin, M. Grätzel, M. K. Nazeeruddin, Enhanced Charge Collection with Passivation Layers in Perovskite Solar Cells. Adv. Mater. 28, 3966. (2016).

17. Lin, T.-C., Cole, J. M., Higginbotham, A. P., Edwards, A. J., Piltz, R. O., Perez-Moreno, J., **Seo, J.-Y.**, Kwon, O.-P. Molecular origins of the high-performance nonlinear optical susceptibility in a phenolic polyene chromophore: Electron density distributions, hydrogen bonding, and ab initio calculations. *The Journal of Physical Chemistry C*, *117*(18), 9416–9430. (2013).

18. Kim, J., **Seo, J.-Y.**, Jazbinsek, M., Kwon, S.-J., Choi, E.-Y., Seo, J.-I., Kwon, O.-P. Rotational isomerism of phenylthiolated chromophores with large variation of optical nonlinearity. *The Journal of Physical Chemistry C*, *116*(47), 25034–25043. (2012).

19. Kwon, O.-P., Kwon, S.-J., Jazbinsek, M., **Seo, J.-Y.**, Kim, J.-T., Seo, J.-I., Günter, P. Phenolic polyene crystals with tailored physical properties and very large nonlinear optical response. *Chemistry of Materials*, *23*(2), 239–246. (2010).

20. Kwon, O.-P., Jazbinsek, M., Yun, H., Seo, J.-I., **Seo, J.-Y.**, Kwon, S.-J.,Günter, P. Crystal engineering by eliminating weak hydrogen bonding sites in phenolic polyene nonlinear optical crystals. *CrystEngComm*, *11*(8), 1541–1544. (2009).

21. Choi, E.-Y., **Seo, J.-Y.**, Jazbinsek, M., & Kwon, O.-P. Thickness control of highly efficient organic electro-optic phenolic polyene crystals by metal acetates. *Crystal Growth & Design*, *9*(10), (2009).

PATENT LIST

1. Method of preparing lactide from lactate (US 8759545B2)
2. Cylinder block for engine of vehicle (US9803582B2)
3. Method and apparatus for producing lactic acid (US8673600B2)
4. Noise reducing structure of speed reduction device for electric CVVT (US9599159B2)
5. Cylinder head for engine (US9617949B2)
6. EXHAUST SYSTEM FOR VEHICLE (KR 1018265450000)
7. CYLINDER BLOCK FOR ENGINE (KR 1016845270000)
8. THERMAL INSULATION COATING COMPOSITION AND THERMAL INSULATION COATING LAYER (KR 1016010950000)
9. CYLINDER HEAD FOR ENGINE (KR 1016193910000)
10. Apparatus for manufacturing lactic acid and method for the same (KR 1013614620000)
11. THERMAL INSULATION COATING COMPOSITION AND THERMAL INSULATION COATING LAYER (KR 1017554570000)
12. Manufacturing Method of Lactide from Lactic acid (KR 1013265210000)
13. Manufacturing Method of Lactide Synthesis from Lactic acid (KR 1013265240000)
14. A method for lactide synthesis from lactic acid salt (KR 1014598190000)
15. A method for preparing lactide using a ionic solvent (KR 1014283400000)
16. SEPERATOR FOR FUEL CELL AND METHOD FOR MANUFACTURING THE SAME (KR 1017554600000)
17. COATING METHOD OF SEPERATOR FOR FUEL CELL AND SEPERATOR FOR FUEL CELL (KR 1017554650000)
18. POROUS POLYMER RESIN LAYER AND METHOD FOR MANUFACTURING THE SAME (KR 1017448060000)
19. METHOD FOR MEASURING COEFFICIENT OF FRICTION FOR SPECIMEN (KR 1016285570000)
20. LIQUID DROPLET SURFACE FRICTION FORCE MEASURING SYSTEM AND METHOD USING AFM (KR 1016625230000)
21. COATING METHOD OF SEPERATOR FOR FUEL CELL AND SEPERATOR FOR FUEL CELL (KR 1017244560000)
22. COATING METHOD OF SEPERATOR FOR FUEL CELL AND SEPERATOR FOR FUEL CELL (KR 1017137180000)
23. ENGINE RADIATE NOISE REDUCTION STRUCTURE (KR 1016845040000)
24. MULTI-LAYER COMPOSITES HAVING THERMAL INSULATION PROPETTY (KR 1016845080000)
25. METHOD AND APPARATUS FOR CONTROLLONG WINDSHIELD GLASS WITH FORWARD VISIBILITY IN CASE OF RAIN (KR 1016841580000)

26. COATING MATERIAL FOR SLIDING PART OF VEHICLE AND COATING METHOD THEREOF (KR 1016737120000)
27. COATING METHOD FOR ENGINE MOVING PARTS (KR 1016646150000)
28. DEVICE FOR DETECTING THERMAL BEHAVIOR OF ENGINE INSULATION COATING LAYER (KR 1016461110000)
29. POROUS POLYMER RESIN LAYER AND METHOD FOR MANUFACTURING THE SAME (KR 1016372700000)
30. VAPOR PRESSURE SIMULATION METHOD FOR PRECURSOR (KR 1016377320000)
31. SURFACE TREATMENT METHOD WITH A SUPERIOR MASS PRODUCTIVITY AND LOW FRICTION CHARACTERISTICS (KR 16285540000)
32. EXHAUST VALVE FOR ENGINE (KR 1015667430000)
33. INTAKE VALVE FOR ENGINE (KR 1015753280000)
34. THERMAL INSULATION COATING COMPOSITION AND THERMAL INSULATION COATING LAYER (KR 1015347150000)
35. METHOD FOR COATING TiAgMoN LAYER (KR 1015192520000)
36. CYLINDER HEAD FOR ENGINE (KR 1015583810000)
37. NOISE REDUCING STRUCTURE OF SPEED REDUCTION DEVICE FOR ELECTRIC CVVT (KR 1015583800000)
38. PISTON FOR ENGINE (KR 1015506350000)

EXPERIMENTAL SKILLS

- Spectroscopy: IR, UV, FL, AS, NMR
- Chromatography: GPC, IC, HPLC
- Microscopy: AFM, SEM, TEM, OM, POM
- Scattering: XRD, XPS
- Thermal analyzer: LFA, DSC, TGA

ACADEMIC ACTIVITY

Awards

01/2010 Best Paper Award Department of Molecular Science & Technology, Ajou Univ.

12/2009 Best Cooperation Award, Department of Molecular Science &Technology, Ajou Univ.

Activity

2011   Industry-Academic Society, Center for Women in Science, Engineering & Technology